$BaTiO_3$-based ceramics: fundamentals, properties and applications

Vincenzo Buscaglia, Maria Teresa Buscaglia, Giovanna Canu

ICMATE-CNR, Institute of Condensed Matter Chemistry and Technologies for Energy,
National Research Council, Via De Marini 6, 16149 Genoa, Italy

Keywords Barium titanate, capacitors, ceramics, dielectric properties, doping, ferroelectricity, perovskites, phase transitions, piezoelectricity, scaling effects

Abstract

Barium titanate, $BaTiO_3$, ~~was~~ has been the first commercial ferroelectric and piezoelectric material. After more than 70 years from its discovery, it is still the most widely used functional ceramic in the electronic industry, mainly as a dielectric in multilayer ceramic capacitors. The commercial success of barium titanate was largely determined by the ease its properties can be adapted to the specific application. After discussing the crystal structure, the defect chemistry and the phase transitions of $BaTiO_3$, the strategies to modify the dielectric and piezoelectric properties by means of chemical modification and microstructure control are systematically reviewed. Existing as well as potential applications are presented.

Corresponding author: vincenzo.buscaglia@ge.icmate.cnr.it (V. Buscaglia)

Index

1. Introduction

Barium titanate, $BaTiO_3$, has been the first ferroelectric and piezoelectric ceramic developed for commercial applications and it is still widely used, especially as a high permittivity dielectric in multilayer ceramic capacitors (MLCCs) and as a semiconducting material in thermistors with positive temperature coefficient of resistivity (PTCR). A detailed chronology of the discovery and important scientific contributions on the understanding and use of $BaTiO_3$ was written by Randall, Newnham and Cross [1]. According to Jaffe [2] and Haertling [3], there were three basic steps in the discovery and understanding of ferroelectricity and piezoelectricity in $BaTiO_3$ which have later paved the way to the development of the entirely new class of ferroelectric ceramic materials with perovskite structure.

The first one, the observation of an unusually high dielectric constant in barium titanate, was independently done in USA, former URSS and Japan during World War II [1]. The second step was the realization that the cause of the high permittivity was ferroelectricity [4,5]. Prior to 1940 only two ferroelectric crystals were known, Rochelle salt (potassium sodium tartrate) and potassium dihydrogen phosphate. However, $BaTiO_3$ has better properties, higher chemical stability and wider temperature range of operation. The third and very important step was the discovery of the "poling" process [6,7]. The application of a strong electric field orients the polarization of the ferroelectric domains within the grains along the direction of the external field and this "poled" state remains even after the removal of the field. Thus, even the ceramic, despite its polycrystalline nature, behaves like a single crystal showing useful pyroelectric and piezoelectric properties. In fact, unpoled ceramics are not piezoelectrically active because the contribution of the randomly oriented grains would, on the whole, cancel out each other. This breakthrough was of fundamental importance for the large scale production and application of ferroelectric materials, as ceramics are much cheaper than single crystals and their properties, though inferior to those of single crystal, can be more easily tailored.

The crystal structure of $BaTiO_3$ and the origin of ferroelectricity in this compound from the cooperative ordering of the electrical dipoles arising from the deformation of the prototype perovskite cubic cell was established by Rooksby [8], Megaw [9], and Kay and Vousden [10]. The phenomenological theory of phase transitions and properties of barium titanate was introduced by Devonshire [11]. This thermodynamic theory was later used for describing ferroelectricity in many perovskite-type crystals and related structures. The temperature dependence of polarization, permittivity and optical properties in $BaTiO_3$ single crystals was determined by Mertz [12], who related the observed variations to the deformations of the lattice. Later, the same author investigated the pressure and electric field dependence of the Curie temperature and interpreted the results using Devonshire's theory [13-14]. The domain structure and the domain switching, which largely affect all properties related to ferroelectricity, were studied, among the others, by Matthias and von Hippel [15] and by Merz [16].

The PTCR effect consists of an anomalous steep increase of resistivity of $BaTiO_3$ (up to 5-6 orders of magnitude) at the tetragonal to cubic phase transition temperature [17-18] and has led to several applications as self-regulating heaters and over-current protection systems. This phenomenon is only observed in polycrystalline $BaTiO_3$, with the spontaneous polarization of the ferroelectric domains modifying the band-bending and, therefore, the electronic transport across the grain boundary.

In spite of more than 70 years of continuous investigation, barium titanate still attracts great attention as a model ferroelectric system and key components of materials for applications in capacitors, lead-free piezoelectric devices, ceramics and composites for energy storage [19-22]. According to Web of Science, about 15,000 papers containing "$BaTiO_3$" or "barium titanate" in their title have been published since 1965. The reasons behind this success are manifolds: (i) simple composition and structure; (ii) high stability and ease to adapt the properties to the specific application by doping, formation of solid solutions with other perovskites and tailoring of microstructure; (iii) relatively simple and cheap processing especially in the case of ceramics; (iv) lack of effective competitors in core applications.

2. Crystal structure, nonstoichiometry and defect chemistry of $BaTiO_3$

The BaO-TiO_2 phase diagram shown in **Figure 1(a)** [23] presents at least 9 ternary compounds which have been proven to be useful as electroceramics, with the most important being the perovskite $BaTiO_3$ for its application in MLCCs and PTCR devices. Rase and Roy [24] published in 1955 a phase diagram in which many phase relationships were clarified. This phase diagram was further modified by O'Bryan and Thomson [25], Negas et al. [26], Ritter et al. [27] and, most recently, by Lee et al. [23].

Below 1460 °C, $BaTiO_3$ possesses the perovskite structure. At higher temperature a hexagonal polymorph (6H-type, s.g. *P63/mmc*) with non-perovskite structure appears. The perovskite to 6H transition temperature is very sensitive to the presence of acceptor dopants, as discussed in section 3.2.

The perovskite form of $BaTiO_3$ exhibits different crystallographic variants, depending on temperature [9-10,28], as shown in **Figure 2**. The high-temperature cubic form has the prototype ABO_3 (with Ba^{2+} as A and Ti^{4+} as B) perovskite structure. This is a centrosymmetric structure with Ba^{2+} at the corners, Ti^{4+} at the center, and the oxygen at the face centers. The titanium ion is octahedrically coordinated by six oxygen ions while Ba^{2+} has a dodecahedral coordination. At the Curie temperature, T_C = 120-130 °C, it turns from the high temperature paraelectric cubic form (C, $Pm\bar{3}m$) to the ferroelectric tetragonal structure (T, *P4mm*). On further cooling, two other ferroelectric phases are observed: orthorhombic (O, *Amm2*), below 5-15 °C, and rhombohedral (R, *R3m*), below -80 – (-90) °C. Discontinuities of the small signal dielectric constant are observed at the transition temperatures (**Figure 2**). All polar forms originate from a small deformation of the prototype cubic lattice arising from the off-center displacement of the Ti ion (about 0.1 Å at room temperature) in the TiO_6 octahedron. Each of these variants can be thought as deformations of the cubic unit cell along an edge ([00l], tetragonal), along a face diagonal ([011], orthorhombic), or along a body diagonal ([111], rhombohedral). Likewise, the orientation of the electrical dipole is [001], [011] and [111] for the T, O and R modifications, respectively. The cooperative, long-range ordering of the electrical dipoles gives rise to macroscopic spontaneous polarization (P_S), spontaneous lattice strain and ferroelectricity [29]. At room temperature the ratio c/a of the lattice parameters of the tetragonal cell ($a=b$, $c > a$)) is 1.011, i.e. the deformation and, consequently, the spontaneous strain is of the order of 1%. At -93 °C the rhombohedral angle α is 89.85° [28], *i.e.* there is only a deviation of 0.15° from the cubic lattice. Despite the small deformation, P_S takes significant values, up 20-25 μC/cm^2 at room temperature. The spontaneous polarization can be switched between energetically equivalent orientations (6, 12 and 8 for the T, O and R phase, respectively) by means of an electric field. Polarization switching is a hysteretic process; by plotting the polarization P against the amplitude of the ac electric field E, the ferroelectric hysteresis loop is obtained (**Figure 3**). The polarization at zero field is called remanent polarization (P_r) and the field at zero polarization is the coercive field (E_c). The switching process requires the application of a field larger than E_c. Polarization and strain are strongly coupled in ferroelectrics: a modification of the strain state determines a variation of polarization and vice versa. Because of the strong coupling between polarization and lattice strain and the often incomplete surface charge screening, the properties of ferroelectric materials are also very sensitive to the mechanical and electrical boundary conditions [29].

Ferroelectric crystals spontaneously split into domains when cooled through the Curie temperature. Domains are regions with uniform orientation of polarization separated by domain walls. In tetragonal $BaTiO_3$, there are two kinds of domain walls, which separate regions with mutually antiparallel (180° walls) or perpendicular (90° walls) orientation of polarization. The other ferroelectric phases of barium titanate have a higher number of domain variants, corresponding to 3 and 4 different kinds of domain walls for the R and O phase, respectively. Domain formation occurs to minimize the elastic and electrostatic energies. In a ceramic, elastic energy in individual grains originates from the variation of lattice parameters and unit cell volume as the material crosses the paraelectric/ferroelectric transition on cooling, owing to the mechanical constraints exerted by the surrounding grains. Formation of 90° domain walls relieves the elastic energy. The electrostatic energy is associated with the depolarizing field produced by the surface charges at the termination of the material. Formation of both 90° and 180° walls relieves the electrostatic energy. Domain walls can move under the action of an external electric field or a mechanical stress. The movement of domain walls at weak to moderate fields is one of the most important so-called extrinsic (non-lattice) contributions to the dielectric, elastic and piezoelectric properties of ferroelectric materials and may be comparable to the intrinsic effect of the lattice [19,29]. The movement of the domain walls is also responsible for the reorientation and switching of the polarization and the existence of the ferroelectric hysteresis loop.

Although for the purpose of this chapter we consider the phase transitions in $BaTiO_3$ as purely displacive, their actual nature has been debated. There is some evidence provided by extended X-ray absorption fine structure (EXAFS), nuclear magnetic resonance (NMR) and the pair-distribution function (PDF) investigations that the local structure of $BaTiO_3$ is different from the average one presented above and remains rhombohedral at all temperatures [30–35]. The results demonstrate the coexistence of displacive and order-disorder components in the phase transition mechanism. According to the eight-site model [36], the Ti ions in the paraelectric cubic phase exhibit off-center local displacement along the eight [111] directions but the average polarization is null because of the random distribution among the 8 split sites. Below the Curie temperature partial ordering occurs. Thus O, T and C long-range structures are the result of the averaging [111] displacements of octahedral Ti over 2, 4 and 8 local rhombohedral directions, respectively. Only for the rhombohedral phase the local and long-range structures are equivalent.

Lee and Randall [37-39] spent a great deal of work in determining the homogeneity range of $BaTiO_3$ as a function of temperature and oxygen partial pressure and estimated the entropy and enthalpy of most important defect reactions. As already reported by Rase and Roy [24], $BaTiO_3$ shows a non-negligible nonstoichiometry in the range 1000-1400 °C. Non-stoichiometry is mainly associated to partial Schottky disorder:

$$TiO_2 \rightarrow Ti_{Ti}^{\times} + 2O_O^{\times} + V_{Ba}^{''} + V_o^{\bullet\bullet} \tag{2.1}$$

$$BaO \rightarrow Ba_{Ba}^{\times} + O_O^{\times} + V_{Ti}^{''''} + 2V_o^{\bullet\bullet} \tag{2.2}$$

where $V_{Ba}^{''}$ and $V_{Ti}^{''''}$ denote a barium vacancy and a titanium vacancy, respectively, and $V_o^{\bullet\bullet}$ indicates an oxygen vacancy. Density functional theory calculations have shown that different combinations of barium vacancies, titanium vacancies and $V_{Ti}^{''''}$-$V_o^{\bullet\bullet}$ pairs can be present in $BaTiO_3$ depending on processing and doping [40]. The homogeneity range attains the maximum width at 1320 °C, the eutectic temperature of the BaO-TiO_2 system in air, with a Ba/Ti atomic ratio ranging from 0.967 to 1.01 [23,37]. In other words, the solubility of TiO_2 in $BaTiO_3$ is larger than that of BaO. The nonstoichiometry within the homogeneity range of $BaTiO_3$ impacts on all intrinsic properties, including the Curie temperature, which can change up to 5-6 °C moving throughout the solubility window, the enthalpy of transition [23,37-39] and the dielectric permittivity [41].

At high temperature and low oxygen partial pressure, oxygen vacancies are also created by oxygen loss from the lattice of $BaTiO_3$ according to reaction:

$$O_O \rightarrow V_O^{\bullet\bullet} + \frac{1}{2}O_2 + 2e' \tag{2.3}$$

where e' is an electron in the conduction band. The formation of electrons is associated to the reduction of Ti^{4+} ($3d^0$) to Ti^{3+} ($3d^1$) and the contribution of 3d orbitals to the conduction band. If n is the concentration of conducting electrons, the charge neutrality condition implies $n = 2[V_o^{\bullet\bullet}]$. The homogeneity range of $BaTiO_3$ decreases with decreasing the oxygen pressure [38] as the formation of oxygen vacancies in reaction (2.3) shifts reactions (2.1) and (2.2) to the left (**Figure 1(b)**).

The defect chemistry of undoped barium titanate as a function of oxygen partial pressure was carefully investigated using high-temperature electrical conductivity measurements [42-45] and the results could be explained by a relatively simple model. The equilibrium conductivity

(**Figure 4**) shows regions corresponding to the reduction regime (n-type conductivity) and the oxidation regime (p-type conductivity) below and above a conductivity minimum located at an oxygen partial pressure $p_{O_2}= p^0_{O_2}$, whose value depends on temperature. In the reduction regime the conductivity increases with decreasing p_{O_2}according to reaction (2.3). However, this reaction becomes the major source of defects only at low oxygen partial pressure, where the slope of the conductivity curve in **Figure 4** is -1/6. Over most of the experimental range shown in **Figure 4**, the accidental acceptor impurities and their compensating oxygen vacancies are the dominant defects, and the condition of charge neutrality can be approximated by [A'] = 2[$V_o^{\bullet\bullet}$], where [A'] represents the net concentration of acceptor impurities (see section 3.1 for a more detailed discussion). Acceptor impurities, such as Al and Fe incorporated at the Ti site as well as Na and K incorporated at the Ba site usually predominates over donor impurities. If Ba/Ti ≠ 1 and the concentration of acceptor impurities is low, the dominating defects will be cation vacancies and oxygen vacancies (reaction (2.1) or (2.2)). Under both the above conditions, the slope of the conductivity curves in **Figure 4** is -1/4. In the oxidation regime above $p^0_{O_2}$, oxygen is incorporated in the perovskite lattice by reaction:

$$V_O^{\bullet\bullet} + \frac{1}{2}O_2 \rightarrow O_O + 2h^{\bullet} \qquad (2.4)$$

where $h^{\bullet}$ is an electron hole in the valence band. This determines an increase of the conductivity with increasing oxygen partial pressure with +1/4 slope in **Figure 4**. Oxygen vacancies exist also in the oxidation regime owing to the presence of a net excess of acceptor impurities or nonstoichiometry.

3. Strategies for modifying defect chemistry, phase transitions and properties

Undoped barium titanate ceramics and single crystals have limited interest for applications as their dielectric, electromechanical and optical properties show a significant temperature dependence (see the variation of dielectric constant in Fig. 2 as an example) whereas, in most cases, a better thermal stability is needed. On the other hand, the strong increase of the dielectric and piezoelectric properties approaching the phase transition temperatures [14,19] would be of high interest for the fabrication of devices with better performances. The development of $BaTiO_3$-based materials and their use in commercial applications has been driven by the need to find a compromise between these two contrasting trends.

Chemical modification represents the most common and simple approach for tuning the phase transitions and the properties of barium titanate and other ferroelectric perovskites such as Pb(Zr,Ti)O_3, (K,Na)NbO_3 and $Na_{0.5}Bi_{0.5}TiO_3$. The term doping is usually used to indicate the substitution of a limited amount of parent ions, typically less than a few at.%. Even a very small amount of dopant can considerably modify functional properties like the electrical conductivity and the domain wall mobility. When a substantial amount of foreign ions is incorporated in the lattice is more appropriate to refer to formation of solid solutions. Chemical modification is essential to shift the phase transition temperatures and in particular to lower T_C around room temperature and modify the nature of the phase transition. The formation of solid solutions introduces disorder and local compositional fluctuations with a decrease of the dipole correlation length, coexistence of polymorphs and diffuse phase transitions over a relatively large temperature range leading to broad permittivity peaks. Doping is also essential to impart the material a number of characteristics essential for its processing and reliability under operating conditions. Typical examples include resistance to degradation of dielectric properties during sintering in reducing atmosphere (essential for the fabrication of capacitors with non-noble metal electrodes), high insulation resistance, resistance to ageing and cycling, control of domain wall mobility. In general, the final properties are the result of a complex interplay between alteration of defect chemistry, shift and modification of phase transitions, changes in crystal structure (average and local) and polar order.

Dielectric and piezoelectric properties can also be controlled by modifying the microstructure and, in particular, by optimizing the grain size. It is well known that the permittivity and the piezoelectric activity of $BaTiO_3$ ceramics are maximized for a grain size of ≈1 µm. A further strategy commonly used to improve the dielectric properties for capacitor application is the fabrication of ceramics with core-shell grains, which combines the chemical modification with the control of microstructure and formation of compositional gradients.

3.1 Incorporation of foreign ions

Substitution of a regular ion (Ba^{2+} or Ti^{4+}) with a foreign ion determines the formation of a point defect [45]. If the substituent cation has a higher positive charge than the ion it replaces (e.g. M^{3+} at the Ba site), it is termed a “donor” and will assume an effective positive charge in the oxide lattice ($M_{Ba}^{\cdot}$). This positive charge will be compensated by defects with a negative charge, most commonly cation vacancies ($V_{Ti}^{''''}$, $V_{Ba}^{''}$) or electrons (e') in the conduction band.

$$2M_2O_3 + 4Ba_{Ba} + Ti_{Ti} \rightarrow 4M^{\bullet}_{Ba} + V^{''''}_{Ti} + 3BaO + BaTiO_3 \qquad (3.1)$$

$$M_2O_3 + 2Ba_{Ba} \rightarrow 2M^{\bullet}_{Ba} + \frac{1}{2}O_2 + 2e' + 2BaO \qquad (3.2)$$

The formation of electrons is associated to the reduction of Ti^{4+} ($3d^0$) to Ti^{3+} ($3d^1$) and the contribution of 3d orbitals to the conduction band. A reaction similar to (3.1) can be written for barium vacancy compensation. According to available literature, titanium vacancies are preferred over barium vacancies as charge compensating defects especially if the dopant concentration is high [46-49]. Most common donors are pentavalent ions such as Nb^{5+}, Ta^{5+} and Sb^{5+} substituting at the Ti site and large trivalent lanthanide ions (La^{3+}, Nd^{3+}, Ce^{3+}, etc.) substituting at the Ba site.

If the foreign cation has a lower charge than the regular ion it substitutes, it is called an "acceptor" and will assume an effective negative charge compensated by positively charged defects, either oxygen vacancies ($V_o^{\bullet\bullet}$) or electron holes ($h^{\bullet}$) in the valence band.

$$M_2O_3 + 2Ti_{Ti} + O_o \rightarrow 2M'_{Ti} + V_o^{\bullet\bullet} + 2TiO_2 \qquad (3.3)$$

$$M_2O_3 + \frac{1}{2}O_2 \rightarrow 2M'_{Ti} + 2h^{\bullet} + 2TiO_2 \qquad (3.4)$$

Common acceptors are monovalent ions (Ag^+, Na^+, K^+, etc.) incorporated at the Ba site and all ions with charge lower than 4 (Li^+, Mg^{2+}, Ca^{2+}, Ni^{2+}, Sc^{3+}, Fe^{3+}, Lu^{3+}, Yb^{3+}) and compatible ionic radius incorporated at the Ti site.

For trivalent cations with an ionic radius intermediate between Ba^{2+} and Ti^{4+}, a further incorporation mechanism, termed "self-compensation", corresponding to the simultaneous substitution at both cation sites, exists:

$$M_2O_3 + Ba_{Ba} + Ti_{Ti} \rightarrow M^{\bullet}_{Ba} + M'_{Ti} + BaTiO_3 \qquad (3.5)$$

Finally, when the substituent cation and the regular cation have the same charge, a neutral defect will originate.

$$MO_2 + Ti_{Ti} \rightarrow M^{\times}_{Ti} + TiO_2 \qquad (3.6)$$

The electrostatic interaction between defects of opposite charge can lead to the formation of defect pairs and defect clusters. These clusters, especially those formed by transition metal acceptors (Fe^{3+}, Mn^{3+}, Mn^{2+}) with a neighboring oxygen vacancy, interact with the domain walls and have a strong effect on the ferroelectric and piezoelectric properties [50].

The prevailing charge compensation mechanism (cation vacancies or electrons, oxygen vacancies or holes) is determined by the formation energy of the defects, the oxygen partial pressure and the dopant concentration. For donor doping, electron compensation will prevail in reducing conditions (the Ti^{4+} ions will be progressively reduced to Ti^{3+} with decreasing oxygen activity) while titanium vacancies will dominate in oxidizing atmospheres [51]. When reaction (3.2) prevails, a plateau on the conductivity vs. oxygen pressure is observed as the number of charge carriers is determined by the donor concentration [52-53]. Donor-doped $BaTiO_3$ ceramics sintered in air can be either semiconducting or insulating at room temperature depending on the doping level and ceramic processing conditions (**Figure 5**). With increasing donor concentration, the resistivity decreases from $\approx 10^{-10}$ $\Omega\cdot$cm of neat $BaTiO_3$ (point 1 in **Figure 5**) down to a minimum of 10^2-10^1 $\Omega\cdot$cm (point 2 in **Figure 5**) for a doping level of, typically, 0.2-0.3 at.% [17,49]. For higher doping levels the resistivity rises and the material become again insulating (point 3 in **Figure 5**). This behavior is usually interpreted as a crossover in the charge compensation mechanism, from prevailing electron compensation to cation vacancy compensation. However, this interpretation is still controversial. Morrison et al. [49,54], on the basis of a detailed study of La-doped samples, concluded that charge compensation always occurs by cation vacancies and that semiconductivity in $BaTiO_3$ is determined by oxygen nonstoichiometry and reduction of Ti^{4+} to Ti^{3+}, as described by reaction (2.3). However, this conclusion was criticized by Smyth [55], based on (i) the existence of a p_{O_2}-independent conductivity plateau proportional to the donor concentration in donor-doped samples and (ii) a reversible weight change determined by the release of excess oxygen contained in La_2O_3 (reaction (3.2)) again proportional to the donor concentration. More recent atomistic simulations have shown that oxygen loss by reaction (2.3) is much more favorable in La-doped $BaTiO_3$ than in the undoped material when compensation occurs by cation vacancy due to the formation of unique defect clusters involving the different point defects [56].

In the interpretation of the resistivity anomaly (**Figure 5**) it should also be considered that the ceramics are not in equilibrium at room temperature and that the defect structure corresponds to that existing at an intermediate temperature between sintering temperature and room temperature. During cooling, reoxidation occurs according to the reverse of reactions (3.2) and/or (2.3) but the level and distribution of oxygen uptake on cooling and, consequently, the electrical properties depend on the sintering atmosphere, the cooling rate and the ceramic microstructure. Lowest values of resistivity are observed for coarse grained ceramics rapidly cooled. In contrast, fine grained ceramics slowly cooled tend to exhibit higher values of resistivity. However, coarse ceramics are highly heterogeneous from the point of view of resistivity, with semiconducting grains and more insulating, reoxidized grain boundaries. This heterogeneous electrical structure is at the root of the PTCR effect [18]. The partial reoxidation of grain boundaries determines the development/enhancement of the Schottky barriers which is required for the appearance of this non-ohmic effect. Depending on processing conditions, a fully reoxidized and insulating skin can appear on the ceramic surface [57].

Materials with stoichiometry corresponding to reaction (3.2) sintered at low oxygen partial pressure are single phase and conducting even for large values of the dopant fraction of the order of 10 at.% [51]. In this case, the donors are effectively compensated by the formation of electrons/Ti^{3+} ions.

3.2 Incorporation of transition metal ions and other acceptors

In many cases the transition metal ions exhibit +2 and +3 charge and, due to their relatively small ionic radius, they usually substitute Ti^{4+} and act as acceptors. Doping of $BaTiO_3$ with ions of 3*d* transition metals, especially Fe, Mn and Co, has been widely investigated as they are quite effective as modifiers of the ferroelectric properties leading to constrained and asymmetric P(E) loops [50,58]. The oxygen vacancies created as charge compensating defects can form defect dipoles with the acceptor ions (e.g. $Fe_{Ti}^{'} - V_{o}^{\bullet\bullet}$) which stabilize the domain walls and clamp their motion (“hardening” effect) [59-60]. Poled acceptor-doped $BaTiO_3$ ceramics can be used as highly linear piezoelectric transducers and actuators with low hysteresis and dissipation for high power/frequency applications [61]. Transition metal ions and other acceptors are also quite effective (reaction (3.3)) to suppress oxygen loss and conductivity increase related to reaction (2.3) when sintering $BaTiO_3$ in reducing atmosphere, leading to insulating ceramics suitable for the preparation of MLCCs with non-noble metal (e.g. Ni) internal electrodes [62].

More recently, $BaTiO_3$ ceramics doped with magnetic transition metal ions have attracted interest as potential multiferroic and magnetoelectric materials because of the appearance of weak magnetism [63-66]. However, when the dopant amount exceeds few at.%, formation of the non-ferroelectric hexagonal polymorph (6H-type, s.g. *P63/mmc*) instead of the perovskite phase is observed.

3.2.1 Stabilization of the hexagonal modification

The perovskite/hexagonal structural transition has been investigated in some detail. In undoped $BaTiO_3$ the 6H polymorph is stabilized by sintering or annealing in a reducing atmosphere or quenching from a temperature above 1430-1460 °C [67-69]. The incorporation of transition metal ions ($BaTi_{1-x}B_xO_{3-\delta}$, B = Fe, Mn, Ni, Co, Cr, Cu) stabilizes the 6H-phase below the transition temperature of 1460 °C reported of pure $BaTiO_3$ (**Figure 1**). In the case of Fe, the transition temperature decreases rapidly and attains ≈1300 °C for $x = 0.05$ and 1150±50 °C for $x = 0.10$ [70], as shown in **Figure 6**. However, a mixture of 6H and perovskite phase persist at even lower temperatures. For example, for $x = 0.05$ a single phase perovskite is only obtained at temperatures ≤1100 °C. The relative amount of the two polymorphs is very sensitive to several operating conditions, including the cooling rate, the composition of the sintering atmosphere and the annealing at temperatures below that of sintering [71]. The perovskite to 6H transformation is commonly accompanied by microstructural modifications and, in particular, by the growth of large plate-like hexagonal grains [68,71]. Stabilization of 6H-phase has been attributed to different reasons, including: (i) the formation of oxygen vacancies, (ii) the Jahn-Teller effect related to specific configurations of the *d*-electrons, and (iii) metal-metal bonding of cations through the face sharing octahedra existing in the 6H-phase. Since the stabilization of the hexagonal polymorph has also been observed for acceptors without *d*-electrons (Mg^{2+}, Al^{3+}) or with filled *d*-orbitals (Zn^{2+}, Ga^{3+}, In^{3+}) [72], the most important factor is likely to be the oxygen vacancies. However, other effects can be of some importance and, for example, can play a role in the different solubility of the acceptors. Extensive solid-solutions were reported for Fe- and Mn-doped ceramics, while for many other acceptors the maximum solubility is of the order of 10 at.% [72-73]. Two series of 6H-$BaTi_{1-x-y}Fe^{3+}_xFe^{4+}_y O_{3-x/2}$ solid solutions with iron predominantly in the form Fe^{3+} or Fe^{4+} were reported by quenching from high temperatures in air or slow cooling to 200 °C in oxygen, respectively [74]. In the first case, Fe^{3+} behaves as an acceptor and oxygen vacancy formation occurs up to $x = 0.67$ (corresponding to $\delta = 0.33$ in $BaFe_xTi_{1-x}O_{3-\delta}$). Higher values of x resulted in the conversion of 6H in other phases. Differently, the oxidation of iron to Fe^{4+} avoids the formation of charge compensating defects and complete solubility exists between $BaTiO_3$ ($x = 0$) and $BaFeO_3$ ($x = 1$). The existence of two different incorporation mechanisms is well evident from the opposite trend of the lattice parameters, as shown in **Figure 7**. The deviation from the ideal behavior of $BaTiO_3$-$BaFeO_{2.5}$ and $BaTiO_3$-$BaFeO_3$ solid solutions indicates that iron is in a mixed valence state though one of the states predominates. The BaO-TiO_2-Fe_2O_3 phase diagram and the rich crystal chemistry in this system with 16 quaternary compounds were reviewed by Siegrist and Vanderah [75]. Manganese shows a behavior similar to iron as it can be incorporated at Ti site as Mn^{3+} with oxygen vacancy compensation or as Mn^{4+} or, again, in both forms depending on the annealing atmosphere and cooling rate [76].

3.2.2 Valence state of transition metal ions in the perovskite lattice

The oxidation number of the transition metal inside the $BaTiO_3$ lattice has been investigated also for low dopant concentrations (x up to 0.02) when the perovskite structure is stable. On the basis of magnetic susceptibility measurements on air-sintered ceramics, Ihrig [77] determined that the +3 state prevails for iron, whereas manganese enters the lattice as Mn^{3+} and Mn^{4+}, and nickel is predominantly divalent. Incorporation of Cr^{4+} was suggested for chromium. The valence state of Cr, Mn and Co was found to change reversibly upon annealing at 700 °C at different oxygen partial pressures (pure oxygen at $1.5x10^7$ Pa, air and H_2/H_2O mixture with $p(O_2) = 10^{-17}$ bar) whereas it remained constant for iron (Fe^{3+}) and nickel (Ni^{2+}) [78]. While Cr^{4+}, Mn^{4+} and Co^{3+} prevail in pure oxygen, Cr^{3+}, Mn^{2+} and Co^{2+} predominate at low oxygen partial pressure. Similar conclusions on the valence states were attained by Hagemann and Hennings [62] from the oxygen vacancy concentration data determined gravimetrically as a function of the oxygen partial pressure for samples containing 0.5 mol.% dopant. The concentration of oxygen vacancies was fixed by the acceptor concentration (reaction (3.3)) down to $p(O_2) = 10^{-10}$-10^{-12} Pa. At lower pressure the contribution of intrinsic vacancies from reaction (2.3) becomes increasingly important. Osawa et al. [79] measured the electrical conductivity of $BaTiO_3$ ceramics containing 2 at.% Mn as a function of oxygen partial pressure (10^{-10} – 10^5 Pa) and concluded that at 900-1000 °C, Mn^{3+} prevails at $p(O_2) < 1$ Pa, whereas Mn^{4+} predominates at higher pressure. The Electron Paramagnetic Resonance (EPR) measurements of Langhammer et al. [80-83] generally confirmed the above trends. After sintering in air, cobalt is incorporated as a mixture of Co^{2+} and Co^{3+}, while Co^{2+} prevails after annealing in reducing atmosphere [80]. Likewise, the valence state of chromium changes from a value intermediate between +4 and +3 to +3 with decreasing oxygen partial pressure [81]. The EPR spectrum of Ni^{2+} was not detected in nickel-doped ceramics sintered in air in both the perovskite and hexagonal modifications [82] and it was postulated that the dopant is mainly incorporated as Ni^{4+} in contrast with the results of Ihrig [77]. Copper is incorporated as Cu^{2+} after sintering in air [83]. Recent EPR results indicated that manganese behaves as an amphoteric dopant in $SrTiO_3$ lattice and can occupy both cation sites simultaneously as Mn^{2+}

at the Sr site and Mn^{3+}/Mn^{4+} at the Ti site [84]. This possibility should also be considered for $BaTiO_3$.

Ni^{2+} and Fe^{3+} are quite effective to shift the Curie temperature down, about 30 °C/at.% for Ni^{2+} and 21 °C/at.% for Fe^{3+}, irrespective of oxygen partial pressure [78]. Cr^{3+} and Co^{2+} are also good shifters (25 and 28 °C/at.%, respectively) but only in reducing atmosphere. Tetravalent chromium stabilizes the orthorhombic phase at lower temperature ($T_{O/R}$ = -80 °C for x = 0 and -105 °C for x = 0.02) whereas most of the other ions shift the rhombohedral-orthorhombic transition to higher temperatures.

3.2.3 Formation of dipolar defects

The formation of near neighbor acceptor-oxygen vacancy pairs, $(M_{Ti}^{'} - V_{O}^{\bullet\bullet})$ and $(M_{Ti}^{''} - V_{O}^{\bullet\bullet})$, was also investigated by EPR in the case of Mn- and Fe-doped $BaTiO_3$ and $PbTiO_3$ [59-60]. The dipolar defects align in the direction of spontaneous polarization by oxygen vacancy motion in the MO_6 octahedron and follow the domain switching upon poling [60,85]. The defect dipoles do not reorient during fast field cycling but reorientation rather requires long time, high thermal energy, and high electric fields. Ordering is destroyed above T_C and is not observed in $SrTiO_3$. The association enthalpy was determined as -0.26 eV [86] for $(Fe_{Ti}^{'}\text{-}V_{O}^{\bullet\bullet})$ in $SrTiO_3$, meaning that most of the dipolar pairs are dissociated above 300 °C. Atomistic simulations performed on $SrTiO_3$ indicate association enthalpies in the range -0.25 to -0.5 eV for different transition metal acceptors [87]. Association enthalpies of -0.2 - (-0.3) eV are reported for defect pairs involving $Mn_{Ti}^{''}$, $Mn_{Ti}^{'}$ and $Fe_{Ti}^{'}$ in $BaTiO_3$ [86].

3.3 Incorporation of rare-earth ions

Trivalent rare-earths cations (RE^{3+}) of the lanthanide series show a progressively smaller ionic radius moving from La^{3+} (r^{XII} = 1.36 Å) to Lu^{3+} (r^{VI} = 0.86 Å), intermediate between Ba^{2+} (r^{XII} = 1.61 Å) and Ti^{4+} (r^{VI} = 0.605 Å). Although the +3 state is the most stable, some lanthanides also exhibit other oxidation states: +2 (Yb, Eu, Sm) and +4 (Pr, Ce, Tb). The specific valence exhibited by these ions depends on the sintering atmosphere and on the incorporation site. The mechanism of rare-earth cation substitution in $BaTiO_3$ has been investigated in detail [88-91] as it plays a key role in determining the properties and the reliability of MLCCs fabricated with the base metal electrode technology.

3.3.1 Incorporation site

For trivalent cations, the incorporation site is determined by the ionic radius. Large ions such as La^{3+} (r^{XII}: 1.36 Å), Ce^{3+} (r^{XII}: 1.34 Å) and Pr^{3+} (r^{XII}: 1.29 Å) exclusively substitute at the Ba site, acting as donors, while the smaller Lu^{3+} (r^{VI}: 0.861 Å) and Yb^{3+} (r^{VI}: 0.868 Å) prefer the Ti site, acting as acceptors [88-93]. Although it is reported that Nd^{3+} (r^{VI}: 1.27 Å) preferentially substitutes at the Ba site [88-91,48], Hirose et al. [94] have shown that the mechanism changes from Ba-site substitution to self-compensation above $x = 0.05$ when Ba/Ti = 1. For all other cations, from Sm^{3+} to Tm^{3+}, the substitution site can be controlled by adjusting the Ba/Ti ratio and, for this reason, they are often indicated as “amphoteric” dopants. Consequently, provided that the maximum solubility is not exceeded, the cation will occupy the Ba site when Ba/Ti < 1, the Ti site when Ba/Ti > 1 and both sites when Ba/Ti = 1. In the latter case, charge compensation defects are not needed (self-compensation, reaction (3.5)). The correct value of Ba/Ti required for the formation of the specific single phase solid solution can be determined taking into account the stoichiometry of the incorporation reactions (3.1)-(3.5). The solubility of the RE^{3+} ions at a given site is strongly dependent on ionic radius. For example, the solubility at Ba site with titanium vacancy compensation exceeds 20 at.% in the case of La^{3+} [95] but drops to 5 at.% for Gd^{3+} [96] and is only of the order of 1 at.% for smaller lanthanides such as Y^{3+}, Dy^{3+} and Er^{3+} [97-99]. Opposite, the solubility of small RE ions at the Ti site is much higher, of the order of 15 at.% for Ho^{3+}, Dy^{3+} and Y^{3+} [97-101], and then rapidly decreases with increasing ionic radius (3.75 at.% for Gd^{3+}). However, the incorporation of a substantial amount of acceptor ions according to reaction (3.3) determines the formation of the hexagonal polymorph of $BaTiO_3$, likewise trivalent and divalent transition metal ions substituting at the Ti site. According to Liu and West [101], 6H-$BaTiO_3$ forms as an intermediate kinetically stabilized phase before transforming into the thermodynamically stable perovskite phase after long-time annealing at high temperatures (> 1500 °C). Prolonged annealing was also required to stabilize the perovskite phase in Er-doped ceramics [99]. In contrast, the incorporation of Fe^{3+} and other transition metal ions shifts the polymorphic phase transition at lower temperatures and annealing is ineffective. Maximum solubility of amphoteric dopants is attained when the lanthanide occupies both sites and attains 24 at.% in the case of Ho^{3+} [100].

The size-dependent crystallochemical behavior of RE ions in $BaTiO_3$ is well reproduced by atomistic simulations especially if the formation of defect clusters driven by the electrostatic interaction between the foreign ion and the oppositely charged compensation defect is taken into account [102-103]. Both experimental results [46-48] and simulations indicate that the preferred compensation defects in donor-doped $BaTiO_3$ are titanium vacancies rather than barium vacancies.

A rapid depression of the Curie point is observed even for moderate amounts of RE^{3+}. The replacement of Ba^{2+} by La^{3+}, Pr^{3+} and Ce^{3+} causes a lowering of T_C at a rate of 22-24 °C/at.% [93,95,104]. Incorporation of Nd^{3+} determines an even faster drop of 40 °C/at.% [48]. However, on further reducing the ionic radius of the lanthanide, both the T_C drop rate and the solubility decrease, as observed for Gd^{3+} [96]. The substitution of Ho^{3+} and Er^{3+} at the Ti site results in a lowering of T_C of 17.5 and 22.2 °C/at.% [101,105], respectively.

The incorporation of RE^{3+} ions with intermediate size (the so-called "magic" dopants, in particular Y^{3+}, Dy^{3+} and Ho^{3+}) in $BaTiO_3$ ceramics is essential to prevent the degradation of insulating resistance and strongly improves the lifetime of MLCCs with Ni electrodes fabricated by the base-metal technology [106-108]. The site occupancy of these lanthanide ions was effective for controlling the donor/acceptor dopant ratio and the microstructure. The detailed mechanism is still debated, but the amphoteric nature of the dopants certainly plays an important role.

3.4 Homovalent substitution

$BaTiO_3$ forms extensive solid solutions with a number of perovskites such as $CaTiO_3$, $SrTiO_3$, $PbTiO_3$, $BaSnO_3$, $BaZrO_3$, $BaHfO_3$ and $BaCeO_3$ [2,19] thus allowing the modification of phase transition temperatures, polar order and properties over a broad range of compositions.

3.4.1 $BaTiO_3$-$MTiO_3$ solid solutions (M = Ca, Sr, Pb)

Despite a similar chemical behavior, Ca^{2+} and Sr^{2+} incorporated at the Ba site have a somewhat different effect on the phase transitions (**Figure 8**) and properties of barium titanate which can be ascribed to their different size [109-111]. The $Ba_{1-x}Sr_xTiO_3$ (BST) solid solution shows a continuous and almost linear decrease of T_C and *c/a* ratio with increasing x, until the quantum paraelectric (or incipient ferroelectric) behavior typical of $SrTiO_3$ is achieved ($x > 0.95$) [2,109-110]. In contrast, in $Ba_{1-x}Ca_xTiO_3$ (BCT) both T_C and *c/a* ratio first show a modest increase with a maximum at $x \approx 0.10$ and then decrease though they remain close to the values of $BaTiO_3$ [2,110-111]. The maximum solubility of Ca^{2+} corresponds to $x = 0.33$. Because of its smaller ionic radius ($r^{XII} = 1.34$ Å) in comparison to Ba^{2+} ($r^{XII} = 1.61$ Å), Ca^{2+} moves off-center, as revealed by EXAFS, first-principle calculations and atomistic modelling [110-112]. Furthermore, the Ca^{2+} displacement amplifies the ferroelectric off-centering of Ti cations nearest to the Ca^{2+} site in a cooperative process thus enhancing ferroelectricity despite the unit cell volume decrease. Opposite, the position of Sr cations (r^{XII} = 1.44 Å) in BST is largely central. The temperatures of the O/T and R/O transitions decrease more rapidly in BCT than in BST with increasing x, showing a strong nonlinear behavior and determining the stabilization of the T phase at low temperatures. Despite its conspicuous ionic radius in octahedral coordination (r^{VI} = 1 Å), Ca^{2+} behaves as an amphoteric dopant and substitutes Ti^{4+} up to x = 0.04 in $BaCa_xTi_{1-x}O_{3-x}$, causing the suppression of T_C at a rate of 22 °C/at.% [113-114].

While Ca^{2+} doping at the Ba site results only in a modest increase (8-10 °C) of T_C, the incorporation of Pb^{2+} determines a continuous rise of the Curie temperature up to 490 °C, the T_C of $PbTiO_3$ [2]. Divalent lead ions tend to move off-center the PbO_{12} dodecahedron [115] due to the stereochemically active $6s^2$ electron lone pair and, consequently, they contribute to the overall polarization and enforce the ferroelectricity of $BaTiO_3$.

$MgTiO_3$ crystallizes with the ilmenite-type structure and Mg^{2+} preferentially substitutes at the Ti site because of its small ionic radius (r^{VI} = 0.72 Å) up to a maximum solubility of ≈ 2 at.% [116]. Accordingly, it is largely used as an acceptor in the fabrication of MLCCs and promotes the formation of core-shell grains [117-119].

3.4.2 $BaTiO_3$-$BaMO_3$ solid solutions (M = Sn, Zr, Hf, Ce)

Despite the large variation of ionic radius (Sn^{4+}: 0.69 Å, Zr^{4+}: 0.72 Å, Ce^{4+}: 0.87 Å) of cations substituting Ti^{4+} (0.605 Å), the $BaM_xTi_{1-x}O_3$ (M= Sn, Hf, Zr, Ce) solid solutions exhibit a very similar behavior of the phase transitions [120-127], exemplified by the $BaZr_xTi_{1-x}O_3$ (BZT) phase diagram [123] shown in **Figure 9**. With increasing x, the T/C transition shifts to lower temperature while the O/T and R/T transitions move to higher temperature until the they meet at the phase convergence point (x_p, T_p), giving rise to the so-called “pinched” transition. The value of x_p, 0.09-0.11, is nearly independent of specific M^{4+} cation, though some papers reports $x_p \approx 0.15$ in BZT. In contrast, T_p increases with increasing the ionic radius of M^{4+}, from ≈ 320 K (Sn) to ≈ 390 K (Ce). When $x > x_p$, a direct and diffuse R/C transition is observed. Although the Curie temperature is depressed in comparison to undoped $BaTiO_3$, the rate at which T_C decreases with increasing x depends on the size of the M^{4+} cations as shown in **Figure 10**. A rapid and linear drop is observed for Sn^{4+} substitution while Ce^{4+} substitution determines a strong nonlinear behavior characterized by a decrease of T_C of only a few degrees up to x = 0.05 and a more rapid decay above x = 0.10 [127]. The behavior of Zr^{4+} is intermediate between Sn^{4+} and Ce^{4+}. All the considered tetravalent cations are significantly bigger than Ti^{4+} and, consequently, they have no tendency to move off-center and do not promote ferroelectric ordering. Therefore, in the case of Sn^{4+}, the linear decrease of T_C can be interpreted as a result of the dilution effect caused by the SnO_6 octahedra. However, Ce^{4+} is much bigger than Ti^{4+} and the CeO_6 octahedra are likely to determine a significant deformation and expansion of the surrounding TiO_6 octahedra enhancing the off-center displacement of Ti^{4+} and thus counterbalancing the dilution effect for low values of x [127].

When the amount of M is large enough, x = 0.19-0.22 (≈ 0.25 for BZT), a ferroelectric to relaxor crossover occurs. In the relaxor state the average crystal structure is cubic $Pm\bar{3}m$ though at local scale it is still acentric in agreement with the existence of polar nanoregions, as discussed in section 4.1.

4. Dielectric properties

The relative dielectric constant (real part of the dielectric permittivity), ε', of tetragonal $BaTiO_3$ single crystal is strongly anisotropic, ≈ 250 along the c-axis and ≈ 4500 on the a-b plane **(Fig. 2)** (replace with ref. 12) at room temperature. Discontinuities of ε' and spontaneous polarization (P_s) accompanied by hysteretic behavior are observed at the transition temperatures [2,12]. The discontinuities indicate that the transitions are first-order. In ceramics these dielectric anomalies transform in peaks and the room temperature dielectric constant varies between 1000 and 5000 depending on processing, residual porosity, nonstoichiometry and grain size. The dependence of the dielectric response of $BaTiO_3$ ceramics on the Ba/Ti ratio was investigated by Lee et al. [41]. The dielectric constant attains maximum values for nearly stoichiometric compositions. In Ti-excess ceramics the permittivity drops because of the formation of a titania rich layer at the grain boundaries or $Ba_6Ti_{17}O_{40}$ inclusions. In Ba-excess samples, the decrease of the dielectric constant was ascribed to the formation of Ba_2TiO_4 inclusions and the accumulation of stress around the secondary phases particles due to the different thermal expansion in comparison to $BaTiO_3$ [39,41]. In any case, the above permittivity values are 100-500 times higher than those of alumina ceramics (ε' ≈ 10), common dielectrics largely used for insulating substrates. Barium titanate also shows relatively low values (≈ 1%) of the loss tangent (tan δ = ε''/ε', where ε'' is the imaginary part of permittivity), an indispensable requirement for a dielectric to be used in capacitors [107,128]. Despite these promising properties, the permittivity of neat barium titanate strongly depends on temperature and the material is not suitable for most practical applications, for which a higher thermal stability of the dielectric constant and, hence, capacitance, are desired.

The above limitations were overcome by modifying the composition and the microstructure of the material and nowadays ceramic $BaTiO_3$ is the most widely used dielectric material in the electronic industry [107,128], mainly for the fabrication of MLCCs. Barium titanate ceramics belong to Class II dielectrics with dielectric constant from 1000 to >20000 and losses in the range 0.01 to 0.03 [128]. The Electronic Industry Alliance (EIA) specification of Class II dielectrics is based on a three-character alphanumeric code. In **Table 1**, the first character is the low temperature operating limit, the second the high temperature limit, and the third the maximum capacitance deviation over the specified temperature range. For example, X7R means that the capacitance variation is less than ±15% (from its value at 25 °C) between −55 and 125 °C. Some commonly used MLCCs have specifications Z5U, Y5V and XNR (N = 5-8). The temperature dependence of permittivity can be adapted to fulfil the requirements corresponding to the given specification by two main strategies: (i) engineering the phase transitions and (ii) controlling the microstructure.

4.1 Phase transition engineering

The incorporation of foreign ions in the $BaTiO_3$ lattice not only determines a shift of the phase transition temperatures as discussed in detail in section 3 but also modifies the order of the phase transition, the width of the dielectric peak at the Curie temperature, the polar order and the frequency dispersion of permittivity. The progressive shift and broadening of the permittivity peak in $BaSn_xTi_{1-x}O_3$ as shown in **Figure 11a** is a representative example. In many heterovalent- and homovalent-substituted $BaTiO_3$ ceramics the dielectric behavior gradually evolves with increasing dopant concentration and a crossover to relaxor state is often observed beyond a critical dopant concentration [120]. The relaxor state exists in many lead-free and lead-bearing ferroelectric systems and its typical signature is the appearance of a strong frequency dispersion of the permittivity peak temperature (T_m). The maximum of both real and imaginary part of permittivity shifts at higher temperature with increasing frequency. However, the frequency dispersion is on the low-temperature side of $\varepsilon'(T)$ whereas it is on the high-temperature side of $\varepsilon''(T)$ (see **Figure 11b** as an example). The frequency dependence of T_m obeys the Vogel-Fulcher law [120]. Relaxor behavior is attributed to the existence of polar nanodomains or polar nanoregions (PNRs) inside a highly polarizable matrix [120,129-130]. The orientation of the elemental electrical dipoles, associated to the off-center displacement of the Ti^{4+} ions in the TiO_6 octahedra in the case of $BaTiO_3$-based relaxors, is highly correlated inside each nanodomain but the dipole moments of the PNRs are almost randomly oriented. The PNRs have a size of the order of a few nanometers and are highly responsive to electric fields as indicated by slim, nonlinear P(E) loops. For sufficiently high fields the nanodomains can be oriented with the electric field leading to large polarization but, on removing the field, due to thermal fluctuations most nanodomains re-acquire a random orientation resulting, differently from conventional ferroelectrics, in a very small P_r. The small but nonzero P_r indicates that a weak correlation also exists among nanodomains. It should be stressed that there is no phase transition across T_m in a relaxor, indeed the PNRs exist at much higher temperatures than T_m, up to the so-called Burns temperature, T_d [129]. The permittivity maximum is simply a manifestation of the slowing down of dipolar motion below T_m [130]. The average structure of a perovskite relaxor is usually cubic but at local level the spatial symmetry is broken, as indicated by Raman scattering and PDFs analysis [131]. The existence of PNRs becomes apparent even in the absence of an electric field on properties depending on P^2, for example in the deviation of the temperature dependence of refractive index and thermal expansion below T_d from the behavior predicted for the paraelectric state [129-130]. At sufficiently low temperature (T_f), the dipolar motion freezes and the permittivity dispersion vanishes.

The dielectric properties of two families of $BaTiO_3$ solid solutions, $BaM_xTi_{1-x}O_3$ and $BaTiO_3$-$Bi(M)O_3$, which have attracted attention for application in capacitors will be discussed in some detail.

4.1.1. $BaTiO_3$-$BaMO_3$ solid solutions

In the case of $BaM_xTi_{1-x}O_3$ (M = Sn, Zr, Hf, Ce) solid solutions [124, 127,132-138], the phase transition sequence (see **Figure 9** as an example), the polar order and the dielectric properties (**Figure 11**) change according to the following scenario:

i) In the $BaTiO_3$-rich side of the system, T_C decreases with increasing x whereas the R/O and O/T transition temperatures rise until the three transitions merge at the phase convergence point (x_p, T_p) with $x_p \approx 0.10$, as described in 3.4.2. For small values of x not larger than a few at.%, the T/C transition remains sharp and first order as in neat $BaTiO_3$. For larger x values, the permittivity peak at T_C broadens and at x_p the transition changes to second order.

ii) The dielectric constant attains its maximum value at or close to x_p. The peak permittivity can be very high, of the order of a few tens of thousands. BZT ceramics, further modified by partial substitution of Ca at the Ba site, have maximum relative permittivity of ≈30000 around room temperature and a moderate temperature stability suitable for Z5U and Y5V capacitors [132-133].

iii) For $x > x_p$, only a single R/C transition persists. The transition becomes progressively more diffuse in temperature (DPT, diffuse phase transition) as indicated by the appearance of a broad and rounded permittivity peak accompanied by some frequency dispersion. Despite the smearing of the transition, the temperature corresponding to the permittivity maximum (T_m) remains independent of frequency and can still be identified as the average T_C.

iv) Beyond a certain substitution level x_r ($x_r = 0.20\text{-}0.25$ depending on M), the value of T_m starts to move at higher temperatures with increasing frequency, a typical sign of relaxor behavior. The ferroelectric to relaxor crossover occurs over a finite composition range and is not accompanied by a macroscopic phase transition [120,137]. Recent broad-band dielectric spectroscopy investigations have suggested that $BaZr_xTi_{1-x}O_3$ compositions, especially those with $x \geq \approx 0.50$ behave like a dipolar glass rather than a typical relaxor [139-140]. Furthermore, ferroelectric order could not be induced by the application of an electric field for the composition with $x = 0.50$. The dielectric relaxation is assigned to local hopping of the off-centered Ti^{4+} ions in frozen $BaTiO_3$ clusters, whose size is rather small and cannot grow on cooling [140].

v) Relaxor or dipolar glass behavior persists up to values of x very close to 1 when M = Zr as complete solid solubility exists between $BaTiO_3$ and $BaZrO_3$ [138]. $BaZrO_3$ is a paraelectric solid with a relative dielectric constant of 37-38 at room temperature and cubic $Pm\overline{3}m$ structure up to the melting point [141]. Complete solid solubility with $BaSnO_3$ and $BaHfO_3$ is also likely. In contrast, the maximum solubility of $BaCeO_3$ is limited and corresponds to $x = 0.33\text{-}0.35$ [92,142].

The evolution of polar order and the decrease of dipole correlation length with composition in $BaZr_xTi_{1-x}O_3$ is well supported by Raman spectroscopy studies [121,143-144]. Strong Raman bands not compatible with a cubic structure were revealed for the relaxor composition $x = 0.40$ but cannot be attributed to a specific symmetry and no sign of phase transitions was detected in the range 78-398 K. The persistence of some polar bands in the Raman spectra [144-145] far above the ferroelectric–paraelectric transition as well as measurements of acoustic emission [146] and refractive index [147] support the existence of locally correlated displacements on the Ti sites and of polar clusters in undoped $BaTiO_3$ and BZT compositions $x = 0.10$ - 0.20 [120]. However, the dynamics of these polar clusters if compared to conventional relaxors, is much faster, reaching the THz range, and the dielectric anomaly at T_C is frequency independent in the radiofrequency region [146].

The local structure and polar order of BZT has been carefully investigated using X-ray absorption fine structure (XAFS) measurements as well as X-ray and neutron PDF analysis [144, 148-149]. The PDF provides direct evidence that the Ti and Zr atoms do not occupy the equivalent octahedral sites expected from the average cubic crystallographic structure of the solid solution. Because of the relatively large difference between the ionic radii of Zr^{4+} and Ti^{4+}, the TiO_6 and ZrO_6 octahedra have a tendency to preserve their individuality, i.e. despite a broad bond length distribution, the average value of the Ti-O and Zr-O distances are, for most of the compositional range, similar to those observed in $BaTiO_3$ and $BaZrO_3$, respectively [148-149]. This is evident in the neutron PDF because the neutron scattering factor of Ti is negative whereas those of the other involved elements is positive. This produces a "negative" peak for the Ti-O pair and a positive peak of the Zr-O pair [148], as shown in **Figure 12**. Furthermore, the X-ray PDF studies [144] suggest that the local structure of Ti-rich compositions is always rhombohedral with Ti displacement in the [111] pseudocubic direction, including the relaxor composition $x = 0.40$ which exhibited a cubic $Pm\overline{3}m$ diffraction pattern (from high-resolution synchrotron radiation experiments) at 100-450 K.

XAFS measurements of Levin et al. [149] have revealed that for low concentrations of Ti, isolated Ti atoms in the relatively large octahedral sites of the $BaZrO_3$ lattice acquire centrosymmetric coordination with average Ti-O distances shorter than those in $BaTiO_3$. In contrast for higher concentrations of titanium, Ti atoms having one or more Ti as their B-site nearest neighbors undergo polar off-center displacements. Opposite, Zr cations are essentially in centric position. Significant deviations from a random distribution of Ti and Zr (i.e. segregation phenomena) were not detected except for compositions close to $BaTiO_3$.

The local structure of $BaTi_{0.74}Zr_{0.26}O_3$ was investigated via first-principle calculations using 3×3×3 supercells [150]. While Ba and Zr off-center displacements were small and uncorrelated, Ti off-center displacement was of the same magnitude as in $BaTiO_3$. Notably, the direction of a Ti-atom displacement is variable and entirely determined by the distribution of the Ti and Zr atoms in the adjacent unit cells. The underlying mechanism involves local strain effects that ensue from the difference in size between the Ti^{4+} and Zr^{4+} cations. A Ti atom is no longer displaced in the direction in which its octahedral cage is compressed.

Because of the existence of a phase convergence point, $BaM_xTi_{1-x}O_3$ systems are of potential interest for electrocaloric cooling. Liu et al. [151] have predicted that an enhanced electrocaloric effect or, in other words, a larger temperature variation ΔT, can be attained for compositions close to the convergence point since the dipole entropy increases by increasing the number of coexisting phases which is maximum at the convergence point. Experimental verification was carried out on different systems varying the composition, x. In particular, Qian et al. [152] have measured a ΔT of 4.2-4.5 K for $x = 0.15$-0.20 in $BaZr_xTi_{1-x}O_3$ ceramics using an electric field of ≈150 kV·cm^{-1}. In the homologous systems with Hf and Sn, the temperature variation was maximized at $x = x_p$. A significant ΔT of 0.35 K was obtained in $BaHf_{0.11}Ti_{0.89}O_3$ under an electric field of only 10 kV·cm^{-1} [126] and a similar result was reported for $BaSn_{0.105}Ti_{0.895}O_3$ [153].

4.1.2 $BaTiO_3$-$Bi(M)O_3$ solid solutions

Solid solutions between $BaTiO_3$ and $Bi(M)O_3$ compounds, such as $BiScO_3$, $Bi(Zn_{0.5}Ti_{0.5})O_3$, $Bi(Mg_{0.5}Zr_{0.5})O_3$, $Bi(Mg_{0.5}Ti_{0.5})O_3$ and $Bi(Mg_{2/3}Nb_{1/3})O_3$, show a common behavior and interesting dielectric properties for high-temperature capacitor applications [154]. When the mole fraction of $Bi(M)O_3$ is between 0.05 and 0.15, depending on M, a transition from tetragonal *P4mm* to a pseudocubic structure is observed. Although the average structure appears cubic at X-ray and neutron diffraction, a detailed refinement performed on the $(1-x)BaTiO_3$-$xBi(Zn_{0.5}Ti_{0.5})O_3$ compositions ($x = 0.10$, 0.20) shows that the oxygen ions and B-site cations (Ti, Zn) are displaced from the positions of the cubic perovskite lattice. PDF analysis indicates that the local structure (1-10 Å) is better described by a *P4mm* model with a c/a ratio of 1.014 ($x = 0.20$), close to that of $BaTiO_3$. However, the c/a ratio decreases with increasing the scale length. Beyond 3-4 nm, the structure is very close to the cubic one. The correlation between the atomic displacements is gradually lost with increasing distance and beyond a scale length corresponding to 6-8 unit cells the distortions will be almost averaged out. The introduction of $Bi(Zn_{0.5}Ti_{0.5})O_3$ ($x \geq 0.10$) in the $BaTiO_3$ lattice introduces sufficient chemical and compositional disorder to break the long-range ferroelectric order. In contrast, for compositions $x = 0.06$ and 0.08, both the average and local structure are tetragonal although at short scale lengths (< 2 nm) the c/a ratio is higher than that of the average structure. The PDF analysis gives direct evidence of the existence of polar clusters for all compositions up to at least 225 °C [155], a temperature much higher than the Curie point of $BaTiO_3$.

Solid solutions with composition in the pseudocubic region exhibit relaxor behavior and a very broad permittivity peak with stable permittivity over a wide temperature range [156-160]. The addition of $Bi(M)O_3$ amounts around 30-50 mol.% broadens the stability range up to temperatures > 400 °C as shown in **Figure 13(a)**. Good thermal stability at 50-350 °C and 1 kHz with ε' ≈ 1000 was reported for $0.7BaTiO_3$-$0.3BiScO_3$ although tanδ rapidly rises above 300 °C [157]. A dielectric constant of ≈ 1030±15 % over the temperature range 25 – 420 °C was reported for the composition $0.7Ba_{0.8}Ca_{0.2}TiO_3$-$0.3Bi(Zn_{0.5}Ti_{0.5})O_3$ [159] while for $0.7BaTiO_3$-$0.3Bi(Mg_{0.5}Zr_{0.5})O_3$ ceramics ε' was ≈ 570±15 % between -20 and 430 °C [160] at 1 kHz with low tangent loss (< 2%) in both cases. The temperature stability range can be further widened up to 550 °C in $(1\text{-}x)BaTiO_3$-$xBi(Mg_{2/3}Nb_{1/3})O_3$ ceramics, $x = 0.50$-0.60, [161] while a very flat permittivity plateau of ≈ 1100 was reported for the ternary $xBaTiO_3$–$(1\text{-}x)(0.5Bi(Zn_{1/2}Ti_{1/2})O_3$–$0.5BiScO_3)$ system [162]. Large amounts of $Bi(M)O_3$ often lead to inhomogeneous element distribution and formation of core-shell grains which contribute to improve the temperature stability [157,160]. Extensive formation of core-shell grains was observed in $BaTiO_3$-based ceramics containing only 5 mol.% $BiScO_3$. Complete homogeneity could not be obtained even after 20 h sintering [157].

While for the tetragonal ferroelectric phase ($x \le 0.07$), the Curie temperature of $(1\text{-}x)BaTiO_3$-$xBiScO_3$ ceramics decreases with increasing x, both T_m and T_f of compositions with pseudocubic structure ($x > 0.07$) increase with increasing x, though $BiScO_3$ is a paraelectric solid. A similar behavior was only reported for $BaTiO_3$-$PbTiO_3$ and $BaTiO_3$-$Na_{0.5}Bi_{0.5}TiO_3$ solid solutions but, in these cases, both end members are ferroelectric [2,163]. A further peculiarity of the $BaTiO_3$-$BiScO_3$ system ($x \ge 0.10$) is represented by the re-entrant relaxor behavior. By decreasing the temperature, the remanent polarization first grows from a very low level to values typical of long-range ferroelectric order and then drops again on further cooling [164]. This indicates that the system re-enters in a more disordered state. The maximum of remanent polarization is observed at temperatures close to T_f. According to Guo et al. [165] and differently from most relaxors in which the PNRs emerge from the paraelectric state, polar clusters grow inside the ferroelectric matrix below T_f.

The Curie temperature of $(1\text{-}x)BaTiO_3$-$xBi(Na_{0.5}Ti_{0.5})O_3$ ($x = 0 – 0.30$) solid solutions increased from 136 °C ($x = 0$) to 214 °C ($x = 0.30$) with increasing x. Stabilization of the tetragonal *P4mm* phase and increase of the *c/a* ratio in comparison to pure $BaTiO_3$ is observed over a wide temperature range, from -250 °C to T_C [163]. The addition of 10% $Bi(Na_{0.5}Ti_{0.5})O_3$ can be used to broaden the application field of barium titanate up to 150 °C. Further modification of the dielectric properties by Nb_2O_5 addition leads to ceramics with an average dielectric constant of ≈1600, compatible with the X9R specification. The properties can be further modified by adding other dopants. A representative example is given in **Figure 13(b)** [166]. Ceramics with composition $(1-x)BaTiO_3$–$xLiTaO_3$, $x = 0.25$-0.30 are also X9R compliant with ε' in the range 700-900 [167]. In addition, they can be sintered in reducing atmosphere and are, in principle, compatible with the base metal electrode technology.

In general, cofiring of Bi-containing dielectrics with base metal electrodes is quite challenging because of the reduction of Bi_2O_3 to metallic bismuth at the reduced oxygen partial pressure needed to avoid the electrode oxidation. Even cofiring with noble metal electrodes is not trivial due to the reactivity of Bi-based dielectrics and the sintering temperature has to be carefully chosen to overcome this problem [154].

4.2 Microstructure control: core-shell grains

Microstructure and, in particular, grain size has a strong impact on ferroelectric, dielectric and piezoelectric properties. The role of grain size has been widely investigated and will be discussed in more detail in section 6. From the point of view of obtaining dielectrics with temperature-stable permittivity, a key aspect is represented by the fabrication of ceramics consisting of grains with a core-shell structure.

In general, the temperature stability can be improved by means of ceramics with non-homogeneous composition at the level of the single grains. For example, the partial interdiffusion between a $BaTiO_3$ core and a $SrTiO_3$ or $BaZrO_3$ shell produces grains with a radial composition gradient and, consequently, with a distribution of the Curie temperature resulting in a broad permittivity peak [168-170]. However, the preferred microstructure for temperature-stable dielectrics belonging to XNR (N = 6-8) classes consists of a nearly pure $BaTiO_3$ core surrounded by a shell of more heavily doped material (**Figure 14**), characterized by diffuse phase transition or relaxor behavior with a broad permittivity peak around room temperature [171]. This result can be attained by controlling the Ba/Ti ratio, the amount and distribution of an appropriate dopant oxide, and grain growth [171-174]. In order to obtain reliable capacitors with improved lifetime by means of the base-metal electrode technology (Ni or Cu electrodes), at least two dopants are needed [107,175]. A first dopant is an acceptor (Mn^{2+}, Mg^{2+}, Ca^{2+}, etc.) added in a small amount (1-2 at.%), which substitutes at the Ti site avoiding the degradation of the dielectric properties of $BaTiO_3$ during sintering in a reducing atmosphere. The preferred second dopant is a rare-earth ion with intermediate ionic radius (Y^{3+}, Ho^{3+}, Dy^{3+}), which substitutes at both Ba and Ti site and is mainly confined in the shell region (**Figure 14**). These rare-earths significantly improve the capacitor lifetime, hindering the degradation of the insulation resistance and, for this reason, they are often denoted as "magic" dopants [107,175]. The mechanism has not fully been elucidated in detail yet but it is certainly determined by the amphoteric behavior of these ions and the resulting effective control of the acceptor/donor ratio, as discussed in section 3.3. Prior to the use of rare-earth dopants, $BaTiO_3$-Co_3O_4-Nb_2O_5 ceramics were widely investigated and used as X7R dielectrics [173-174]. A sintering aid, usually a powdered glass or silica, is often added to lower the sintering temperature. In most cases, the formation of the shell does not occur by solid-state diffusion of the dopant but, rather, by a dissolution-precipitation process mediated by the existence, during sintering, of a liquid phase in which the dopant oxides dissolve [171,174,176-179]. Microstructure control plays a crucial role on the performances of the capacitors and needs the optimization of several parameters. Sintering temperature has to be carefully optimized as variations of only 10-20 °C can significantly modify the dielectric properties [174,180] by inducing grain growth and composition homogenization. The relative amount of the dopants has also a crucial influence on the temperature stability. In $BaTiO_3$-Co_3O_4-Nb_2O_5 dielectrics [174,178], the inward diffusion of Co is no longer prevented if Nb/Co < 2, resulting in composition homogenization and collapse of the core-shell structure. In $BaTiO_3$ ceramics co-doped with Mg and Ho, an appropriate amount of Mg is necessary for suppressing the inward diffusion of the rare-earth ions. MgO first reacts with $BaTiO_3$ and forms the shell region in which Mg^{2+} substitutes at the Ti site. At higher temperature, Ho^{3+} also incorporates in the perovskite but its diffusivity is controlled by the Mg/Ho ratio [181]. Likewise, the Mg/Y ratio plays a dominant role in the formation of the core-shell structure in $BaTiO_3$-MgO-Y_2O_3 dielectrics [118]. In general, a higher amount of MgO is required to suppress the grain growth and the diffusion into the core region for the larger lanthanide ions (La^{3+}, Sm^{3+}) compared to the intermediate size ions (Ho^{3+}, Dy^{3+}, Er^{3+}) [117]. The different behavior is related to the different incorporation site of the lanthanide ions: predominant substitution at Ba site for La^{3+} and Sm^{3+}, substitution at both Ba and Ti site for Ho^{3+}, Dy^{3+} and Er^{3+}, as discussed in section 3.3. It is worth noting that in the fabrication of MLCCs, the dielectric material is prepared by directly adding the different dopants to the $BaTiO_3$ powder. The lanthanide ions of intermediate size distribute between the two cation sites depending on the A/B ratio. The volumetric ratio between core and shell is also an important microstructural parameter.

A better control on the formation of the core-shell structure, especially when the grain size is in the submicron scale, can be achieved by coating the $BaTiO_3$ particles with a layer of the dopant oxide using a colloidal chemistry approach [182]. The formation of core-shell grains is also essential to obtain X9R-compliant dielectrics [166,183].

One of the main drawbacks of $BaTiO_3$ ceramics is the relatively low dielectric strength ($E_b \approx$ 90 kV·cm^{-1}) which limits the high-field applications. A significant improvement of the breakdown field can be obtained by realizing $BaTiO_3$-SiO_2/glass composites with a microstructure comprising $BaTiO_3$ grains surrounded by a silica/glass layer at grain boundary [184-187]. Zhang et al. [184] have observed a progressive increase of E_b from 90 to 280 kV·cm^{-1} with increasing silica content from 0 to 8 wt.% and a parallel decrease of the dielectric constant from ≈ 4000 to ≈ 500. The ceramics were fabricated using $BaTiO_3$@SiO_2 core-shell particles prepared by a Stöber-like process with different thickness of the silica shell. The existence of a continuous silica network with a low dielectric constant (≈ 4) determines a strongly nonhomogeneous distribution of the electric field. In particular, the electric field in the silica layer is higher than the applied field, whereas it is lower than the applied field in the ferroelectric cores. The higher dielectric strength of silica (≈ 400 kV·cm^{-1}) and the “screening” effect of the shell results in improved insulating properties of the composite. The breakdown field further increases to ≈ 330 kV·cm^{-1} in $BaTiO_3$/$BaTiO_3$@SiO_2/$BaTiO_3$ multilayered thick films [187].

The encapsulation of $BaTiO_3$ and $Ba_{0.6}Sr_{0.4}TiO_3$ particles of different diameter with an amorphous silica shell by means of a modified Stöber process, using tetraethoxysilane (TEOS) as precursor, was investigated by Elissalde and co-workers [188–191]. In the case of $Ba_{0.6}Sr_{0.4}TiO_3$ particles, the thickness of the shell can be controlled between 2 and 80 nm with high accuracy [189]. Thanks to the silica shell, the sintering temperature can be decreased to ≈ 1000 °C, in comparison to values of the order of 1300-1400 °C required for the uncoated particles, thus avoiding grain growth. Good densification (92%) was also obtained by sintering in a microwave furnace [191]. Densification of $BaTiO_3$@SiO_2 core-shell particles by Spark Plasma Sintering and post-annealing at 800 °C in air produced ceramics with a giant dielectric constant (> 10^5, 10 kHz) and a relatively low loss tangent (≈ 0.05) in the range 25–180 °C [190]. The silica shell is a good dielectric and, moreover, slows down reoxidation of the inner region of the $BaTiO_3$ grains, which remain semiconducting after post-annealing. At low frequency (< 10^5 Hz) and above room temperature, the effective permittivity is controlled by the insulating grain boundary layer, whereas at higher frequency and lower temperature the contribution of grain cores predominates and the permittivity drops to values typical of $BaTiO_3$.

4.3 Dielectrics for energy storage

The main driving force for the continuous development of the MLCC technology is the large scale application of these passive components in consumer electronics. However, in the last few years there has been an increasing demand for ceramic capacitors with higher energy density for power electronic devices and pulse power applications, including hybrid and electrical vehicles. While ceramic capacitors have a high power density (fast charge/discharge performances), the energy density is relatively low and extensive studies have been undertaken to develop new dielectric materials with enhanced breakdown field and improved storage efficiency [20-22].

Room-temperature properties of some bulk ceramics reported in recent years [157, 192-203] are summarized in **Table 2**. Because of the slim polarization loops (small hysteresis) and high breakdown field, $BaTiO_3$-$Bi(M)O_3$ relaxors are potential dielectric materials for energy storage. The recoverable energy density attains values up to 2-3 $J \cdot cm^{-3}$ with efficiency of 80-90 % at fields of $\approx$200 $kV \cdot cm^{-1}$. Thin (15 μm thickness) $BaTiO_3$-$BiScO_3$ dielectrics exhibited superior energy storage capability at the same applied electric field, relative to commercial MLCCs [157]. The charge storage performance of $BaTiO_3$ ceramics is significantly lower (energy density: 0.3-0.4 $J \cdot cm^{-3}$), because of the large hysteresis (efficiency $< 50\%$) and the inferior dielectric strength ($\approx$ 90 $kV \cdot cm^{-1}$) [184-185]. However, the recoverable energy density can substantially be increased up to 1.2 $J \cdot cm^{-3}$ in ceramics obtained by densification of $BaTiO_3$@SiO_2 core-shell particles [184], because of the enhanced dielectric strength, as previously discussed.

$BaTiO_3$-$Bi(M)O_3$ relaxors also exhibit excellent thermal stability of the energy density and efficiency. Ceramics with composition $0.85BaTiO_3$-$0.15Bi(Mg_{0.5}Zr_{0.5})O_3$ show a decrease of energy density of only 12% from room temperature to 150 °C at a field of 220 $kV \cdot cm^{-1}$ and energy efficiency > 80% [192]. A similar stability was reported for $0.85BaTiO_3$–$0.15Bi(Zn_{1/2}Sn_{1/2})O_3$ at 150 $kV \cdot cm^{-1}$, with an efficiency > 95% [194].

$Ba_{1-x}Sr_xTiO_3$ ceramics [200-203] in the paraelectric state at room temperature also show significantly enhanced energy storage density in comparison to $BaTiO_3$ (up to 1.3 $J \cdot cm^{-3}$, **Table 2**) though the performances are inferior to the previously described $BaTiO_3$-based relaxors.

4.4 Tunable dielectrics

Only a few remarks on $BaTiO_3$-based tunable dielectrics will be given here; for a detailed overview on tunable ferroelectrics the review paper of Tagantsev et al. [204] is recommended.

A typical feature of ferroelectric materials is the strong nonlinear dependence of dielectric permittivity on the applied bias electric field. This feature is described by the tunability, *n*, the ratio of the permittivity of the material at zero electric field, $\varepsilon'(0)$, to the permittivity at a given non-zero electric field, $\varepsilon'(E)$. The relative tunability is defined as $[\varepsilon'(0) - \varepsilon'(E)]/\varepsilon'(0)]$ [204]. A variable permittivity with high tunability is attractive for the fabrication of microwave devices such as tunable dielectric resonators, tunable filters and tunable capacitors (varactors). However, the higher losses of ferroelectrics in comparison to conventional microwave dielectrics and the high voltage needed for tuning limit the use of bulk ceramic or single crystal varactors. Materials in the paraelectric state are preferred because the absence of domains reduces the losses and the hysteretic behavior. $BaTiO_3$–based solid solutions such as $Ba_{1-x}Sr_xTiO_3$, $BaTi_{1-x}Zr_xO_3$ and $BaTi_{1-x}Sn_xO_3$ ceramics show a high tunability, especially in the vicinity of phase transitions. At room temperature, the relative tunability at 30 $kV\cdot cm^{-1}$ and 10 kHz is 80% for $BaZr_{0.25}Ti_{0.75}O_3$ and 50% for $Ba_{0.60}Sr_{0.40}TiO_3$ [205]. The variation of permittivity with dielectric field and of relative tunability with temperature is reported in **Figure 15** for different $BaTi_{1-x}Zr_xO_3$ compositions ($x = 0.20$-0.35). The composition $x = 0.20$ and 0.25 shows the maximum relative tunability (85%) at the Curie temperature (297 K and 257 K, respectively) [206]. Compositions $x = 0.30$ and 0.35 have a relaxor behavior. For many homogeneous single phase ferroelectrics, the higher the permittivity the higher the tunability but also the losses and the temperature dependence of permittivity [204]. The correlation between tunability and losses obliges to find materials with the best trade-off between these two parameters. A guide to choose among different materials is provided by the commutation quality factor [204]. Given an appropriate value of the quality factor required for the specific application, materials with high tunability ($n \geq 1.5$) and not too high permittivity (≤ 1000) are generally preferred. Composites between $Ba_{1-x}Sr_xTiO_3$ and a linear dielectric oxide, such as MgO, have been extensively investigated because the dielectric constant can be adjusted and losses lowered by changing the amount of the linear dielectric while retaining a reasonable tunability [204-205, 207-208].

5. Piezoelectric properties

$BaTiO_3$ was the first oxide material to be developed as a piezoceramic [1-3] and was used on large scale for applications in the generation of acoustic and ultrasonic vibrations, vibration detection and actuators. Typical values of the piezoelectric properties of $BaTiO_3$ ceramics are d_{33} = 191 pC/N, d_{31} = -79 pC/N, d_{15} = 270 pC/N, k_{33} = 0.49, k_p = 0.38 [2]. The piezoelectric properties of $BaTiO_3$, likewise dielectric permittivity, are strongly temperature dependent because of the polymorphic transitions. For most commercial purposes it is now superseded by Pb(Zr,TiO)$_3$ (PZT) ceramics, with morphotropic boundary composition. PZT has superior properties, a wider temperature application range and a higher thermal stability. Undoped BaTiO$_3$ cannot be used for high field and high frequency applications such as the generation of ultrasonic power, because of the rapid increase of dielectric losses with increasing field. These losses arise largely from the movement of domain walls. Substitution of transition metal ion acceptors (Co^{3+} is particularly effective) at the Ti site leads to domain wall clamping and consequently to a strong reduction of the losses. As a further effect of domain wall clamping, Co^{3+}-doped BaTiO$_3$ shows greater resistance than PZT to depoling by compressive stresses and, consequently, it is still used in some applications despite the inferior piezoelectric activity [2,209]. The piezoelectric properties of barium titanate ceramics can be further modified by tailoring the microstructure. The influence of grain size will be discussed in section 6.

In recent years, BaTiO$_3$-based piezoceramics have attracted a renewed interest after the publication of the paper of Liu and Ren [210] in 2009, reporting outstanding piezoelectric properties, comparable or even superior to those of PZT at room temperature, in the (1-x)Ba(Ti$_{0.8}$Zr$_{0.2}$)O$_3$-x(Ba$_{0.7}$Ca$_{0.3}$)TiO$_3$ system (BCTZ) for x = 0.50. The material showed $d_{33} \approx$ 600 pC·N^{-1} and a large signal piezoelectric coefficient d$_{33}^*$ (defined as the ratio of the strain and the corresponding electric field) of 1140 pm·V^{-1} at 50 kV·cm^{-1}. An even higher value of d$_{33}^*$ of 1310 pm·V^{-1} at 50 kV·cm^{-1} was reported at x = 0.45 by Ehmke et al. [211]. The high piezoelectric activity was initially attributed to the existence of a morphotropic phase boundary (MPB) between the tetragonal and the rhombohedral phase. However, Keeble et al. [212], in 2013, on the basis of a careful temperature dependent XRD study of this system, demonstrated that there is not a MPB but, rather, a narrow temperature-composition region, which separates the other two crystallographic polar variants, where the orthorhombic phase is stable (see **Figure 16**). A phase diagram very similar to that reported in ref. 212 was constructed by Acosta et al. [213] from dielectric permittivity data. Moving from low to high temperature, the same phase sequence (R-O-T-C) as in undoped BaTiO$_3$ is observed. However, as the presence of Zr lowers the T_C and stabilizes the R phase at higher temperature, while the effect of calcium is to shift the R/O and O/T boundaries at lower temperature, the three phase transitions are observed in a narrow (270-365 K) temperature range at x = 0.50. Furthermore, the different transitions meet at a phase convergence point at x = 0.32-0.35 and 333-337 K. The phase boundaries are not horizontal but quite slanting, and this enhances the tendency to “instability” of the system, a situation quite favorable for producing high piezoelectric properties. In fact, small variations of composition or temperature stabilize one phase respect to the adjacent one, meaning that the free energy landscape is rather flat, thus promoting phase coexistence, increasing the degrees of freedom of the system and making it highly responsive to external stimuli. One possible mechanism responsible for properties enhancement is the "polarization rotation" [214] process. Available data indicate that d_{33} features maximum values around the phase transitions when varying temperature at constant composition or composition at constant temperature [19,213], as shown in **Figure 17**. At room temperature, Zhang et al. [215] reported two maxima of d_{33} corresponding to the R/O transition at x = 0.44 and the O/T transition at x = 0.50. More generally, the highest values of d_{33} are obtained along the O/T transition, while high values of d_{33}^* are observed over a broad region around the O phase with maximum at R/O and O/T transitions. A second maximum of d_{33} is located at $x \approx 0.35$, just above room temperature and close to the R/O transition. These features are partially inherited from the $BaZr_yTi_{1-y}O_3$ system, which shows the same behavior for y = 0.06-0.10, with d_{33} = 770 pC·N^{-1} at 65 °C at the O/T transition [123]. This further confirms that an important effect of Ca substitution is the shift the O/T phase transition to room temperature when x = 0.50. The origin of the large piezoelectric activity in BCTZ ceramics was investigated using the Landau-Devonshire phenomenological theory [216]. Based on the combined computational and experimental results, it was concluded that a reduction in anisotropy energy (i.e. a weaker dependency of energy on the polarization orientation) accompanied by elastic softening (i.e. increase of elastic compliance) is a necessary condition for enhanced piezoelectric properties. Properties can be further maximized where a high spontaneous/remanent polarization can be retained. Despite four different phases coexist at the convergence point and the elastic compliance is comparable to that of the O/T phase boundary, a maximum in d_{33} is not observed at this composition, mainly due to the lower spontaneous/remanent polarization values determined by the small unit cell distortion.

The properties of BCTZ ceramics are highly dependent on processing, relative density, microstructure and poling conditions [217-221]. In the case of powders prepared by solid-state reaction, factors like the precursor powder size and the calcination temperature can have a significant impact on the chemical homogeneity at local level. Differently from undoped $BaTiO_3$, which shows optimal values of properties in ceramics with grain size of ≈1 μm, the electromechanical constants d_{33}^* and d_{33} are maximized for a grain size of the order of 10-30 μm [217-221]. Field cooling poling was found quite effective to improve the piezoelectric properties of BCTZ ceramics. This was attributed to the development of an internal bias field caused by the alignment of defect charge carriers, rather than higher degree of domain texture

[222]. A drawback of the BCTZ system is the relatively low T_C (70-75 °C for $x = 0.40$ and 90-95°C for $x = 0.60$) which reduces the operating temperature range of the material. Furthermore, d_{33} decays rapidly with increasing temperature. The Curie point can be increased but at the expenses of the piezoelectric properties; for example $T_C = 114$°C and $d_{33} = 450$ pC·N^{-1} in $(1-x)Ba(Zr_{0.15}Ti_{0.85})O_3–x(Ba_{0.8}Ca_{0.2})TiO_3$ for $x = 0.53$ [223]. Texturing is a common strategy to further enhancing the piezoelectric activity of ceramics by orienting the grains along a common and favorable crystallographic direction, using template grain growth. For [001] grain-oriented $(Ba_{0.94}Ca_{0.06})(Ti_{0.95}Zr_{0.05})O_3$ ceramics, a very high d_{33} of 755 pC·N^{-1} and an extremely large d_{33}^*coefficient of 2027 pm·V^{-1}, along with a low strain hysteresis, were reported by Liu et al. [224].

The family of $(Ba,Ca)(Ti,Sn)O_3$ (BCTS) ceramics has also been investigated in detail and shows excellent piezoelectric properties, whereas the $(Ba,Ca)(Ti,Hf)O_3$ (BCTH) system was less extensively explored. The phase diagrams and the general features of BCTZ, BCTS and BCTH systems are similar [19,212,225-229]. Low signal $d_{33} > 500$ pC·N^{-1} and $d_{33}^* > 1000$ pm·V^{-1} were reported for a wide range of BCTS compositions in proximity of the O/T transition and, more generally, at the polymorphic phase transitions [226-230]. In particular, $d_{33} = 670$ pC·N^{-1} for $x = 0.07$-0.09 and $d_{33}^* = 1414$ pm·V^{-1} for $x = 0.11$ were reported in $Ba_{0.95}Ca_{0.05}T_{1-x}Sn_xO_3$ ceramics [227]. A remarkable piezoelectric coefficient, $d_{33} = 697$ pC·N^{-1}, was also measured in $BaSn_xTi_{1-x}O_3$ ceramics with composition corresponding to the phase convergence point, $x = 0.11$, with T_C of 40 °C [231]. However, this material has limited interest, because of the inherent thermal instability and the incorporation of Ca is essential to stabilize the tetragonal phase at higher temperature. Very recently a detailed mapping of d_{33} (**Figure 18**) has revealed values higher than 600 pC·N^{-1} for a large range of compositions ($x = 0.06 – 0.23$) in $(1-x)Ba(Ti_{0.89}Sn_{0.11})O_3–x(Ba_{0.70}Ca_{0.30})TiO_3$ ceramics at room temperature, with a maximum of 700 pC·N^{-1} for $x = 0.18$ [232]. Despite the high piezoelectric activity, the T_C of the compositions with the best properties is only 60-70 °C and, consequently, a rapid drop of d_{33} is observed with increasing temperature. BCTH ceramics generally show a reduced piezoelectric activity in comparison to BCTZ and BCTS [225,233], with higher values of d_{33} at the R/O and O/T phase boundary, up to ≈500 pC·N^{-1} in $Ba_{0.85}Ca_{0.15}Hf_{0.1}Ti_{0.9}O_3$ with a Curie temperature of ≈85°C. q

An improvement of the piezoelectric properties of $BaTiO_3$ can be obtained by adding a small amount of LiF, which also lowers the sintering temperature to 1100 °C, i.e. at least 200-300 °C below the temperature generally employed. Li compounds such as Li_2O, Li_2CO_3 and LiF are well-known sintering aids, which promote densification by formation of a liquid phase and growth of grains with core-shell microstructure [234]. Yang et al. [235] showed that the addition of 4 mol.% LiF leads to d_{33} = 270 pC·N^{-1} and k_p = 0.45, though T_C is lowered to 73 °C. Kimura et al. [236] sintered Li-doped ceramics with improved d_{33} = 260 pC·N^{-1}, k_p = 0.44 and T_C = 130 °C using hydrothermally-synthesized powders. In both cases, the presence of Li stabilizes the orthorhombic phase at room temperature and this can contribute to the enhancement of the piezoelectric activity. Even higher d_{33} values > 300 pC·N^{-1} were measured on undoped $BaTiO_3$ ceramics with grain size of ≈ 50 μm sintered at 1160-1230 °C from hydrothermal powders. The poled ceramics exhibited orthorhombic or mixed tetragonal-orthorhombic structure. Optimal properties, d_{33} = 355 pC·N^{-1} and k_p = 0.40, were obtained after sintering at 1190 °C [237]. Coarse-grained (grain size >10 μm) ceramics densified by spark plasma sintering featured d_{33} values up to 416 pC·N^{-1} [238]. In both cases, the enhancement of piezoelectric activity was ascribed to the presence of nanodomains with thickness of few tens of nanometers. However, the origin of these nanodomains is still unclear. As discussed in the next section, maximum piezoelectric activity is usually observed in ceramics with grains size around 1 μm.

6. Size and scaling effects

The properties of ferroelectric materials, including $BaTiO_3$, in form of films, particles and ceramics show a significant variation with decreasing the physical dimension (thickness for films, diameter for particles and grain size for ceramics) [239-240]. Representative examples are provided by the dielectric response and the piezoelectric activity.

Kinoshita and Yamaji [241] first reported a progressive increase of the dielectric permittivity of $BaTiO_3$ ceramics with decreasing the grain size from 53 to 1.1 μm. A systematic lowering of saturation polarization, piezoelectric coefficients and electromechanical coupling constants with diminishing grain size (4 – 0.2 μm) was described in PZT ceramics by Randall et al. [242]. The room temperature dielectric constant of barium titanate ceramics as a function of grain size, as obtained by plotting the data reported by several authors [243-252], is shown in **Figure 19**. A pronounced maximum with ε_r = 5000-6000 is observed at a grain size of ≈ 1 μm. These values are 3-4 times higher than the dielectric permittivity (≈1500) measured in ceramics with grain size > 10 μm. The permittivity is significantly suppressed to values even lower than 1000 in ceramics with nanosized grains.

The piezoelectric coefficient d_{33} exhibits a trend similar to dielectric permittivity, with a maximum > 500 $pC{\cdot}N^{-1}$ again at ≈ 1 μm [253-257] to be compared with the piezoelectric coefficient of coarse grained ceramics, 180-190 $pC{\cdot}N^{-1}$ (**Figure 20**). However, some data sets indicate the existence of a broad maximum at a grain size of 4-5 μm.

Size and scaling effects in ferroelectric materials have received significant attention for over five decades. Besides the fundamental question of determining the critical size at which ferroelectric order vanishes, many studies have been driven by the continuous miniaturization process of virtually all active and passive electronic components, with a size reduction of the functional material inside the devices. Ferroelectric perovskites are used in different devices, including MLCCs, non-volatile memories (FERAMs) and multilayer piezoelectric transducers and actuators. A typical example of device downsizing is represented by MLCCs, widely used in consumer electronics, smartphones, hybrid and electrical vehicles. A typical multilayer capacitor is essentially a parallel connection of many stacked ceramic plate capacitors [107,128]. The interdigitated conducting layers form the counter-electrodes for each dielectric layer. The capacitance of a MLCC is given by

$$C = \varepsilon_0 \varepsilon' n \frac{S}{t}$$

where S is the overlap electrode area, t the thickness of the single dielectric layer, n the number of layers and ε_0 the permittivity of vacuum. A reduction of the case size keeping the capacitance constant can then be obtained by decreasing the geometric parameters t and S or the lateral size of the capacitor if n is increased.

In the last 20 years the typical thickness of the dielectric layers has decreased from 10 to 0.5 μm. Most of the capacitors are fabricated using the nickel inner electrodes technology, that co-fires the $BaTiO_3$ based dielectrics with Ni-electrode layers in a reducing atmosphere [107,128]. Taking into account that, for reasons of long-term reliability, it is preferable to have several grains (5-7) spanning the thickness of each dielectric layer, the grain size of top edge MLCCs is of the order of 100 nm or even less. The dielectric constant of $BaTiO_3$ is significantly suppressed (< 2000) when the grain size approaches the nanoscale region and this trend continues with further reducing the grain size (**Figure 19**), with a significant effect on the capacitor performance. In fact, the same depression reported for undoped ceramics is also exhibited by $BaTiO_3$-based dielectrics used in XNR (N = 6-9) capacitors. For example, the dielectric constant of X7R compliant ceramics decreases from ≈ 2800 to ≈ 2000 while decreasing the grain size from 460 to 120 nm [258].

The scaling of properties is mainly of extrinsic origin and determined by the contribution of different types of interfaces such as grain boundaries, domain walls and other extended defects, whose concentration or volume fraction changes as the system size scales [239-240]. A detailed discussion of the mechanisms responsible for size and scaling effects in ferroelectrics is beyond the aim of this contribution and only some general results are summarized below. Recent reviews can be found in ref. 240 and 259.

The domain configuration, the domain wall density and the domain wall mobility change with the grain size and this determines a dimension-dependent contribution to permittivity and piezoelectric properties. As anticipated in section 2, the domain wall movement represents the major extrinsic contribution to the dielectric and piezoelectric properties at low and moderate fields [29].

The domain configuration becomes simpler with decreasing grain size (**Figure 21**). Coarse grained ceramics (> ≈10 μm) show complex three-dimensional arrangements of 90° and 180° domain walls and their dielectric permittivity is practically constant. Below about 10 μm, the grains predominantly exhibit stripe domain patterns with domains separated by 90° walls. The domain width decreases from 0.3-0.4 μm to less than 100 nm in submicron ceramics. Domain walls are no longer observed when the grain size is smaller than 200-300 nm, and the grains mainly comprise single domains [244,247,249,260-261].

According to the model of Arlt et al. [243], the permittivity of $BaTiO_3$ ceramics is given as the sum of two terms: the lattice contribution (assumed independent of grain size) and the domain wall contribution. When the grain size g is the range 1-10 μm, the width of the 90° domains is proportional to g^m with $m = ½$ and, consequently, the dielectric permittivity increases with decreasing grain size with a $g^{-1/2}$ dependence, in agreement with the experimental data. The proportionality between the domain width and the square root of a characteristic length of the material (thickness for slabs, diameter for wires, lateral side for nanocubes) is a general property of ferroic crystals [262-263] which was initially proposed by C. Kittel for ferromagnetic materials. When $g < 1$ μm , m rises to values > 1.

In the model, the wall mobility was assumed to be independent of grain size. Later, Arlt and Pertsev [264] predicted that the domain wall mobility is also a function of the grain size. A recent investigation using in-situ synchrotron X-ray diffraction experiments on ceramics with different grain size (0.3 - 3.5 μm) has provided further insight into the dependence of mobility on grain size [265]. It was shown that the motion of 90° domain walls is greatest under both strong (above coercive) and weak (below coercive) electric fields for an intermediate grain size of ≈ 2 μm. Furthermore, the domain wall motion was strongly suppressed in the ceramic with grain size of 0.3 μm. The reduction of wall mobility in ferroelectric ceramics with submicron and nanometric grains is also indicated by the progressive tilting of the P(E) hysteresis loops with a reduction of both remanent and spontaneous polarization [244,249,266]. Domain reorientation and switching become increasingly more difficult as the grain size is reduced towards the single domain grain regime.

There is general consensus that the grain boundaries in $BaTiO_3$ and other perovskites have a non-ferroelectric character and a much lower permittivity ($\varepsilon' \approx 10^2$) than the grain cores ($\varepsilon' \approx 10^3$) forming a "dead-layer" region which exert an increasing dilution effect on the dielectric properties of ceramics with decreasing grain size, especially at submicron and nanometric scale [244,247,249,267-269]. The low permittivity grain boundaries determine a redistribution of the electric field inside the ceramic. Finite element modelling has shown that the effective electric field is higher than the applied field in the grain boundaries perpendicular to the direction of the applied field and lower in the grain cores. This inhomogeneity increases with decreasing grain size. A main effect of electric field redistribution is the progressive decrease of the nonlinear contribution to effective permittivity and of tunability [269] as the grain size goes down. The effect of grain boundaries has also been investigated by phase-field simulation based on Ginzburg-Landau kinetic equation with the grain size varying form 170 do 10 nm [270]. At low field the monotonic decrease of dielectric permittivity with decreasing grain size is confirmed. At high field, the dielectric and piezoelectric responses are dominated by the dynamics of domain structure above the grain size of 50 nm and by the properties of the dead layer below this value. As a result, the large field permittivity and d_{33} first increase and then decrease with a maximum at ≈50nm. The distribution of polarization in the remnant state after field removal undergoes a profound alteration with decreasing grain size, from a monodomain state at 110 nm to a vortex organization at 15 nm. The change of polarization distribution is determined by the significant depolarization field associated to the "dead-layer". A similar transition in the polarization was also predicted by Fu and Bellaiche [271] in $BaTiO_3$ nanoparticles using a first-principles-based approach. Further experimental studies are needed to confirm these trends.

The enhancement of the dielectric strength with decreasing grains size experimentally observed [268] has been elucidated by phase field modelling and ascribed to the higher breakdown energy of the grain boundaries with respect to grain cores [272]. The impact of grain boundaries is also dependent on the Ba/Ti ratio. Ti-rich stoichiometries beyond the solubility limit cause the segregation of a crystalline or amorphous titania-rich layer which further amplifies the dilution effect. A significant binary oxide excess leads to the formation of secondary phase inclusions such as Ba_2TiO_4 (Ba-excess), $BaTi_2O_5$ and $Ba_6Ti_{17}O_{40}$ (Ti-excess) [39,41].

Although the domain wall mobility probably plays a main role in determining the existence of the permittivity maximum in **Figure 19**, the dilution effect of grain boundaries gives an increasing and significant contribution to permittivity depression when the grain size is $< \approx 0.5$ μm [244,247]. Furthermore, the inhomogeneous distribution of the electric field in fine grained ceramics results in a decrease of the effective field in the grain core [269] with a negative impact on domain reorientation and switching [266].

A broad dispersion of experimental data is apparent from **Figures 19** and **20**. The dispersion can be attributed to the use of powders synthesized with various methods and different precursors as well as to differences in subsequent processing, including sintering technique, sintering thermal parameters and possible post-sintering annealing treatment. The synthesis step introduces impurities of variable nature and amount as well as variability of the Ba/Ti ratio which, in turn, affects the lattice defects concentration and impacts all the properties. For example, coarse-grained ceramics sintered in the same conditions exhibited a room temperature dielectric constant in the range 950-1800, increasing the Ba/Ti molar ratio from 0.97 to 1.03 with maximum permittivity at 1.01 [41]. The impact of stoichiometry can partly explain the broad dispersion of the piezoelectric activity data, which is even larger than that of the permittivity response. Dai et al. [273] systematically investigated the dependence of d_{33} on grain size for different values of the Ba/Ti ratio from 0.998 to 1.002. The maximum of d_{33} was found at a grain size of ≈ 1 μm when Ba/Ti ≥ 1 and at ≈ 4 μm when Ba/Ti < 1, and this might justify the existence of two sets of data with a different trend in **Figure 20**. Maximum piezoelectric activity (> 500 pC/N) is attained at Ba/Ti = 1.

When the particle/grain size is reduced below ≈ 100 nm, the high fraction of surface/interface atoms produces a disturbance of the polar order, reducing the thermodynamic stability of the polar phase in comparison to the paraelectric modification, with a progressive decrease of T_C and spontaneous polarization until ferroelectricity will vanish below a critical size [240,274].

This phenomenon is usually referred to as "intrinsic" size effect and, along with the reduced domain wall mobility and the dilution effect of grain boundaries, will contribute to the downscaling of properties. The critical size for ferroelectricity is of the order of ≈ 10 nm for isolated particles and grains in ceramics containing a low concentration of impurities and defects [248, 275-277].

From the above discussion it is clear that multiple mechanisms combine to produce the maximization of the dielectric constant and piezoelectric properties exhibited by $BaTiO_3$ ceramics for an intermediate grain size and, more generally, the observed variations of properties with grain size. The size and scaling effects are further convoluted with spurious contributions related to stoichiometry, impurities and defects leading to a large dispersion of experimental data and the behaviour of specific samples can be hardly understood without a comprehensive chemical and microstructural analysis.

The decline of permittivity and all other functional properties with decreasing grain size, albeit unavoidable, can be alleviated by the use of high purity precursors, a tight control of the Ba/Ti ratio and a careful processing. The coherence length and ferroelectric order will be enhanced in materials with high crystalline order, low defect concentration, absence of local strain gradients and internal stresses. A low level of impurities and a stoichiometry within the homogeneity range of the compound will decrease the effective thickness of the grain boundary layer and its dilution effect.

References

1. Randall, C.A., Newnham, R.E. and Cross, L.E. (2004). History of the First Ferroelectric Oxide, $BaTiO_3$, Materials Research Institute, The Pennsylvania State University, University Park, PA 16802 USA.
2. Jaffe B., Cook, W.R. and Jaffe, H. (1971). *Piezoelectric Ceramics*, Academic Press, London.
3. Haertling, G.H. (1999). Ferroelectric ceramics: history and technology, *Journal of the American Ceramic Society* **82**, 797-818.
4. Wul, B. M. and Goldman, I. M. (1945). Dielectric Constants of Titanates of Metals of the Second Group, *Comptes Rendus de l'Académie des Sciences de l'URSS*, **46**, 139–142.
5. von Hippel, A., Breckenridge, R. G., Chesley, F. G. and Tisza, L. (1946). High Dielectric Constant Ceramics, *Ind. Eng. Chem.,* **38,** 1097–1109.
6. Gray, R. B. (1949). U.S. Pat. No. US2486560A. (Transducer and Method of Making the Same).
7. Roberts, S. (1947). Dielectric and Piezoelectric Properties of Barium Titanate, *Phys. Rev.,* **71**, 890-895.

8. Rooksby, H. P. (1945). Compounds of the Structural Type of Calcium Titanate, *Nature* **155,** 484-484.
9. Megaw, H. D. (1945). Crystal Structure of Barium Titanate, *Nature*, **155**, 484-485.
10. Kay, H. F. and Vousden, P. (1949). Symmetry changes in barium titanate at low temperatures and their relation to its ferroelectric properties, *Philos. Mag*. **40,** 1019-1040.
11. Devonshire, A.F. (1949). Theory of barium titanate, *Philos. Mag*. **40,** 1040-1063.
12. Mertz, W. J. (1949). The Electric and Optical Behavior of $BaTiO_3$ Single-Domain Crystals, *Physical Review* **76,** 1221-1225.
13. Mertz, W. J. (1950). The Effect of Hydrostatic Pressure on the Curie Point of Barium Titanate Single Crystals, *Physical Review* **77,** 52-54.
14. Mertz, W. J. (1953). Double Hysteresis Loops of $BaTiO_3$ at the Curie Point, *Physical Review* **91,** 513-517.
15. Matthias, B. and von Hippel, A. (1948). Domain Structure and Dielectric Response of Barium Titanate Single Crystals, Phys. Rev. **73**, 1378-1384.
16. Merz, W.J. (1954). Domain Formation and Domain Wall Motions in Ferroelectric $BaTiO_3$ Single Crystals, Phys. Rev. **95**, 690-698.
17. Jonker, G.H. (1964). Some aspects of semiconducting barium titanate, *Solid-State Electron.* **7**, 895-903.
18. Heywang, W. (1971). Semiconducting barium titanate. *J. Mater. Sci.* **6**, 1214
19. Acosta, M., Novak, N., Rojas, V. et al. (2017). $BaTiO_3$-based piezoelectrics: Fundamentals, current status, and perspectives, *Appl. Phys. Rev.* **4,** 041305.
20. Yao, Z. H., Song, Z., Hao, H. et al., (2017). Homogeneous/Inhomogeneous-Structured Dielectrics and their Energy-Storage Performances, *Advanced Materials* **29**, 1601727.
21. Palneedi, H., Peddigari, M., Hwang, G. T., Jeong, D. Y. and Ryu, J. G. (2018). High-Performance Dielectric Ceramic Films for Energy Storage Capacitors: Progress and Outlook, *Advanced Functional Materials* **28**, 1803665.
22. Prateek, P., Thakur, V. K. and Gupta, R. K. (2016). Recent Progress on Ferroelectric Polymer-Based Nanocomposites for High Energy Density Capacitors: Synthesis, Dielectric Properties, and Future Aspects, *Chem. Rev.,* **116**, 4260−4317.
23. Lee, S., Liu, Z.-K. and Randall, C. A. (2007). Modified Phase Diagram for the Barium Oxide-Titanium Dioxide System for the Ferroelectric Barium Titanate, *Journal of the American Ceramic Society* **90**, 2589–94.
24. Rase, D. E. and Roy, R. (1955). Phase Equilibrium in the System BaO–TiO_2, *Journal of the American Ceramic Society* **38**, 102–13.
25. O'Bryan, M. Jr. and Thomson, J. Jr. (1974). Phase Equilibria in the TiO_2-Rich Region of the System BaO–TiO_2, *Journal of the American Ceramic Society* **57**, 522–6.
26. Negas, T., Roth, R. S., Parker, H. S. and Minor, D. (1974). Subsolidus Phase Relations in the $BaTiO_3$–TiO_2 System, J. *Solid State Chem.* **9**, 297–307.
27. Ritter, J. J., Roth, R. S. and Blendell, J. E. (1986). Alkoxide Precursor Synthesis and Characterization of Phases in the Barium–Titanium Oxide System, *Journal of the American Ceramic Society* **69**, 155–62.
28. Kwei, G. H., Lawson, A. C., Billinge, J. L. and Cheong, S.-W. (1993). Structure of the Ferroelectric Phase of Barium Titanate. *J. Phys. Chem.* **97**, 2368–2377.
29. Damjanovic, D. (1998). Ferroelectric, dielectric and piezoelectric properties of ferroelectric thin films and ceramics. *Reports Prog. Phys.* **61**, 1267-1324.

30. Comes, R., Lambert, M. and Guinier, A. (1968). The chain structure of $BaTiO_3$ and KNbO3. *Solid State Commun*. **6**, 715–719.
31. Kwei, G. H., Billinge, S. J. L., Cheong, S. W. and Saxton, J. G. (1995). Pair-distribution functions of ferroelectric perovskites: Direct observation of structural ground states. *Ferroelectrics* **164**, 57–73.
32. Ravel, B., Stern, E. A., Vedrinskii, R. I. and Kraizman, V. (1998). Local structure and the phase transitions of $BaTiO_3$. *Ferroelectrics* **206**, 407–430.
33. Zalar, B., Laguta, V. V. and Blinc, R. (2003). NMR Evidence for the Coexistence of Order-Disorder and Displacive Components in Barium Titanate. *Phys. Rev. Lett.* **90**, 037601.
34. Levin, I., Krayzman, V. and Woicik, J. C. (2014). Local structure in perovskite (Ba, Sr)TiO_3: Reverse Monte Carlo refinements from multiple measurement techniques. *Physical Review B* **89,** 024106.
35. Senn, M. S., Keen, D. A., Lucas, T. C. A., Hriljac, J. A. and Goodwin, A. L. (2016). Emergence of Long-Range Order in $BaTiO_3$ from Local Symmetry-Breaking Distortions. *Phys. Rev. Lett.* **116**, 207602.
36. Pirc, R. and Blinc, R. (2004). Off-center Ti model of barium titanate. *Physical Review B* **70**, 134107.
37. Lee, S., Liu, Z.-K. and Randall, C. A. (2008). Comprehensive Linkage of Defect and Phase Equilibria through Ferroelectric Transition Behavior in $BaTiO_3$-Based Dielectrics: Part 1. Defect Energies under Ambient Air Conditions, *Journal of the American Ceramic Society* **91**, 1748–1752
38. Lee, S. and Randall, C. A. (2008). Comprehensive Linkage of Defect and Phase Equilibria Through Ferroelectric Transition Behavior in $BaTiO_3$-Based Dielectrics: Part 2. Defect Modeling Under Low Oxygen Partial Pressure Conditions, *Journal of the American Ceramic Society* **91**, 1753–1761.
39. Lee, S., Liu, Z.-K., Kim, M. H. and Randall, C. A. (2007). Influence of Nonstoichiometry on Ferroelectric Phase Transition in $BaTiO_3$, *Journal of Applied Physics* **101**, 054119/1–8.
40. Baker, J. N. Bowes P. C., Harris, J. S. and Irving, D. L. (2018). Mechanisms governing metal vacancy formation in $BaTiO_3$ and $SrTiO_3$, *Journal of Applied Physics* **124**, 114101.
41. Lee, J. K, Hong, K. S. and Jang, J. W. (2001). Roles of Ba/Ti Ratios in the Dielectric Properties of $BaTiO_3$ Ceramics, *Journal of the American Ceramic Society* **84** 2001–2006.
42. Long, S. A. and Blumenthal, R. N. (1971). Ti-rich nonostoichiometric $BaTiO_3$: I, High-Temperature Electrical Conductivity Measurements, *Journal of the American Ceramic Society* **54**, 515-519.
43. Long, S. A. and Blumenthal, R. N. (1971). Ti-rich nonostoichiometric $BaTiO_3$: II, Analysis of Defect Structure, *Journal of the American Ceramic Society* **54**, 577-583.
44. Chan, N. H., Sharma, R. K., Smyth, D. M. (1981). Nonstoichiometry in undoped $BaTiO_3$, *Journal of the American Ceramic Society* **64**, 556-562.
45. Smyth, D. M. (1985). Defects and order in perovskite-related compounds, *Ann. Rev. Mater. Sci.,* 15, 329-357.
46. Jonker, G. H., Havinga, E. E. (1982). The influence of foreign ions on the crystal lattice of barium titanate, *Mat. Res. Bull.* **17,** 345-350.
47. Chan, H. M., Harmer, M. P., Smyth, D. M. (1986). Compensating defects in highly donor-doped $BaTiO_3$, *Journal of the American Ceramic Society* **69,** 507-510.
48. Shaikh, A. S. and Vest, R. W. (1986). Defect structure and dielectric properties of Nd_2O_3-modified $BaTiO_3$. *Journal of the American Ceramic Society* **69**, 689-694.

49. Morrison, F. D., Coats, A. M., Sinclair, D. C. and West, A. R. (2001). Charge Compensation Mechanisms in La-Doped $BaTiO_3$, *J. Electroceram.,* **6**, 219-232.
50. Jin, L., Li, F. and Zhang, S.J. (2014). Decoding the Fingerprint of Ferroelectric Loops: Comprehension of the Material Properties and Structures, *Journal of the American Ceramic Society* **97,** 1-27.
51. Makovec, D. and Drofenik, M. (2000). Microstructural Changes during the Reduction/Reoxidation Process in Donor-Doped $BaTiO_3$ Ceramics, *Journal of the American Ceramic Society* **83**, 2593–99.
52. Daniels J. and Härdtl, K.H. (1976). *Philips Res. Repts.* **31**, 489.
53. Chan, N. H. and Smyth, D. M. (1984). Defect chemistry of donor-doped $BaTiO_3$, *Journal of the American Ceramic Society* **67** 285-288.
54. Morrison, F. D., Sinclair, D. C. and West, A. R. (2001). Alternative Explanation for the Origin of the Resistivity Anomaly in La-Doped $BaTiO_3$, *Journal of the American Ceramic Society* **84**, 474-476.
55. Smyth, D.M. (2002). The Defect Chemistry of Donor-Doped $BaTiO_3$: A Rebuttal, *Journal of Electroceramics* **9**, 179–186.
56. Freeman, C. L., Dawson, J. A., Chen, H.-R. et al. (2013). Energetics of Donor-Doping, Metal Vacancies, and Oxygen-Loss in A-Site Rare-Earth-Doped $BaTiO_3$, *Advanced Functional Materials* **23**, 3925–3928.
57. Morrison, F. D., Sinclair, D. C. and West, A. R. (2001). Characterization of Lanthanum-Doped Barium Titanate Ceramics Using Impedance Spectroscopy, *Journal of the American Ceramic Society* **84**, 531–38.
58. Hall, D. A., Ben-Omran, M. M. and Stevenson, P. J. (1998). Field and temperature dependence of dielectric properties in BaTiO3-based piezoceramics, *J. Phys.: Condens. Matter* **10,** 461–476.
59. Zhang, L. X., Erdem, E., Ren, X. B. and Eichel, R. A. (2008). Reorientation of $(\mathrm{Mn_{Ti}}''\text{-}\mathrm{V_O}^{\bullet\bullet})$ defect dipoles in acceptor-modified $BaTiO_3$ single crystals: An electron paramagnetic resonance study, *Applied Physics Letters* **93**, 202901.
60. Erhart, P., Eichel, R.-A., Träskelin, P. and Albe, K. (2007). Association of oxygen vacancies with impurity metal ions in lead titanate, *Physical Review B* **76,** 174116.
61. Zhang, S., Lim, J. B., Lee, H. J. and Shrout T. R. (2009). Characterization of Hard Piezoelectric Lead-Free Ceramics, *IEEE Transactions on Ultrasonics, Ferroelectrics, and Frequency Control* **56**, 1523-1527.
62. Hagemann, H. J. and Hennings, D. (1981). Reversible weight change of acceptor-doped $BaTiO_3$, Journal of the American Ceramic Society **64,** 590-594.
63. Raj S., Mahadevan P., Mandal S., et al., (2008). High temperature ferromagnetism in single crystalline dilute Fe-doped $BaTiO_3$, *Physical Review B* **77** 104416.
64. Xu, B., Yin, K. B. and Lin, J. (2009). Room-temperature ferromagnetism and ferroelectricity in Fe-doped $BaTiO_3$, *Physical Review B* **79,** 134109.
65. Lin, Y.-H., Yuan, J. and Zhang, S. (2009). Multiferroic behavior observed in highly orientated Mn-doped $BaTiO_3$ thin films, *Applied Physics Letters* **95**, 033105.
66. Son, J. Y., Lee, J.-H., Song, S., Shin, Y.-H. and Jang H. M. (2013). Four-States Multiferroic Memory Embodied Using Mn-Doped $BaTiO_3$ Nanorods, *ACS Nano* **7,** 5522-5529.
67. Glaister, R. M. and Kay, H. F. (1960). An Investigation of the Cubic-Hexagonal Transition in Barium Titanate, *Proc. Phys. Soc.* **76,** 763.

68. Kolar, D., Kunaver, U. and Rečnik, A. (1998). Exaggerated Anisotropic Grain Growth in Hexagonal Barium Titanate Ceramics, *Physica Status Solidi (A)* **166**, 219-230.
69. Sinclair, D.C., Skakle, J. M. S., Morrison, F. D., Smith, R. I. and Beales, T. P. (1999). Structure and electrical properties of oxygen-deficient hexagonal $BaTiO_3$, *J. Mater. Chem.,* **9**, 1327–1331.
70. Masó, N., Beltrán, H., Cordoncillo, E., Escribano, P. and West, A. R. (2006). Electrical properties of Fe-doped $BaTiO_3$, J. *Mater. Chem.,* **16**, 1626–1633.
71. Langhammer, H. T., Müller, T., Felgner, K.-H. and Abicht, H.-P. (2000). Crystal Structure and Related Properties of Manganese-Doped Barium Titanate Ceramics, *Journal of the American Ceramic Society* **83**, 605–11.
72. Keith, G. M., Rampling, M. J., Sarma, K., Mc. Alford, N. and Sinclair, D.C. (2004). Synthesis and characterisation of doped 6H-$BaTiO_3$ ceramics, *Journal of the European Ceramic Society* **24,** 1721–1724.
73. Das, S. K., Mishra, R. N. and Roul, B. K. (2014). Magnetic and ferroelectric properties of Ni doped $BaTiO_3$, *Solid State Communications* **191**, 19–24.
74. Grey, I. E., Li, C., Cranswick, L. M. D., Roth, R. S. and Vanderah, T. A. (1998). Structure Analysis of the 6H–Ba(Ti, Fe^{3+}, Fe^{4+})$O_{3-\delta}$ Solid Solution, *J. Solid State Chem.* **135**, 312-321.
75. Siegrist, T. and Vanderah, T. A. (2003). Combining Magnets and Dielectrics: Crystal Chemistry in the BaO-Fe_2O_3-TiO_2 System, *European Journal of Inorganic Chemistry* 2003, 1483-1501
76. Miranda, L., Feteira, A., Sinclair, D. C., at al. (2009). Composition-Structure-Property Relationships of 6H- and 12R-Type Hexagonal Ba(Mn,Ti)$O_{3-\delta}$ Perovskites, *Chem. Mater.* **21**, 1731–1742.
77. Ihrig, H. (1978). The phase stability of $BaTiO_3$ as a function of doped 3d elements: an experimental study, *J. Phys. C: Solid State Phys.* **11**, 819-827.
78. Hagemann, H. J. and Ihrig, H. (1979). Valence change and phase stability of 3d-doped $BaTiO_3$ annealed in oxygen and hydrogen, *Physical Review B* **20,** 3871-3878.
79. Ozawa, S., Furuzawa, A. and Fujikawa, N. (1993). Effect of manganese valence state on the electrical conductivity of barium titanate, *Journal of the American Ceramic Society* **76,** 1191-1194.
80. Langhammer, T., Böttcher, R., Müller, T., Walther, T. and Ebbinghaus, S. G. (2015). Defect properties of cobalt-doped hexagonal barium titanate ceramics, *J. Phys.: Condens. Matter* **27,** 295901.
81. Langhammer, H. T., Müller, T., Böttcher, R. and Abicht, H.-P. (2008). Structural and optical properties of chromium-doped hexagonal barium titanate ceramics, *J. Phys.: Condens. Matter* **20,** 085206.
82. Böttcher, R., Langhammer, H. T. and Müller, T. (2011). Paramagnetic resonance study of nickel ions in hexagonal barium titanate, *J. Phys.: Condens. Matter* **23,** 115903.
83. Langhammer, H. T. Müller, T., Böttcher, R. and Abicht, H.-P. (2003). Crystal structure and related properties of copper-doped barium titanate ceramics, *Solid State Sciences* **5,** 965–971.
84. Maier, R. A., Johnston-Peck, A. C. and Donohue, M. P. (2016). (Magic Dopant) Amphoteric Behavior of a Redox-Active Transition Metal Ion in a Perovskite Lattice: New Insights on the Lattice Site Occupation of Manganese in $SrTiO_3$, *Advanced Functional Materials* **26**, 8325–8333.

85. Warren, W. L., Pike, G. E., Vanheusden, K., Dimos, D. and Tuttle, B. A. (1996) Defect-dipole alignment and tetragonal strain in ferroelectrics, J. App. Phys. **79**, 9250-9257.
86. Merkle, R. and Maier, J. (2003). Defect Association in Acceptor-Doped $SrTiO_3$: Case Study for $Fe_{Ti}'V_O^{\cdot\cdot}$ and $Mn_{Ti}''V_O^{\cdot\cdot}$, *Phys. Chem. Chem. Phys.* **5**, 2297−2303.
87. Schie, M., Waser, R. and De Souza, R. A. (2014). A Simulation Study of Oxygen-Vacancy Behavior in Strontium Titanate: Beyond Nearest-Neighbor Interactions, *J. Phys. Chem. C* **118**, 15185−15192.
88. Xue, L. A., Chen, Y. and Brook, R. J. (1988). The influence of ionic radii on the incorporation of trivalent dopants into $BaTiO_3$, *Materials Science and Engineering: B* **1**, 193-201.
89. Buscaglia, M. T., Buscaglia, V., Viviani, M., Nanni, P. and Hanuskova, M. (2000). Influence of foreign ions on the crystal structure of $BaTiO_3$, *Journal of the European Ceramic Society* **20**, 1997-2007.
90. Tsur, Y., Dumbar, T. D. and Randall, C. A. (2001). Crystal and defect chemistry of rare earth cations in $BaTiO_3$, *Journal of Electroceramics* **7,** 25-34.
91. Dunbar, T. D., Warren, W. L., Tuttle, B. A., Randall, C. A. and Tsur, Y. (2004). Electron paramagnetic resonance investigations of lanthanide-doped barium titanate: Dopant site occupancy, *The Journal of Physical Chemistry B* **108,** 908-917.
92. Makovec, D., Samardžija, Z. and Kolar, D. (1996). Solid Solubility of Cerium in $BaTiO_3$, *Journal of Solid State Chemistry* **123,** 30-38.
93. Lu, D.-Y., Sun, X.-Y., Liu, B., Zhang, J.-L., Ogata, T. (2014). Structural and dielectric properties, electron paramagnetic resonance, and defect chemistry of Pr-doped $BaTiO_3$ ceramics, *Journal of Alloys and Compounds* **615,** 25–34.
94. Hirose, N., Skakle, J. M. S. and West, A.R. (1999). Doping mechanism and permittivity correlations in Nd-doped $BaTiO_3$, *Journal of Electroceramics* **3,** 233-238.
95. Morrison, F. D., Sinclair, D. C. and West, A. R. (1999). Electrical and structural characteristics of lanthanum-doped barium titanate ceramics, *Journal of Applied Physics* **86**, 6355.
96. Ben, L. B. and Sinclair, D. C. (2011). Anomalous Curie temperature behavior of A-site Gd-doped $BaTiO_3$ ceramics: The influence of strain, Applied Physics Letters **98**, 092907.
97. Zhi, J., Chen, A., Zhi, Y., Vilarinho, P. M. and Baptista, J. L. (1999). Incorporation of yttrium in barium titanate ceramics, *Journal of the American Ceramic Society* **82**, 1345-1348.
98. Lee, W. H., Groen, W.A., Schreinemacher, H. and Hennings, D. (2000). Dysprosium doped dielectric materials for sintering in reducing atmospheres, *Journal of Electroceramics* **5,** 31-36.
99. Buscaglia, M. T. Viviani M., Buscaglia V., Bottino, C. (2002). Incorporation of Er^{3+} into $BaTiO_3$, *Journal of the American Ceramic Society* **85**, 1569–75
100. Makovec, D. Samardzija, Z. and Drofenik, M. (2004). Solid solubility of holmium, yttrium, and dysprosium in $BaTiO_3$, *Journal of the American Ceramic Society* **87,** 1324-1329.
101. Liu, Y. and West, A. R. (2009). Ho-doped $BaTiO_3$: Polymorphism, phase equilibria and dielectric properties of $BaTi_{1-x}Ho_xO_{3-x/2}$: $0 \le x \le 0.17$, *Journal of the European Ceramic Society* **29,** 3249–3257.
102. Buscaglia, M. T., Buscaglia, V., Viviani, M. and Nanni, P. (2001). Atomistic simulation of dopant incorporation in barium titanate, *Journal of the American Ceramic Society* **84**, 376–384.

103. Freeman, C. L., Dawson, J. A., Chen, H.-R. et al., (2011). A new potential model for barium titanate and its implications for rare-earth doping, *J. Mater. Chem.* **21**, 4861.
104. Hwang, J. H., Han, Y. H., (2001). Electrical Prop3erties of Cerium-Doped $BaTiO_3$, *Journal of the American Ceramic Society* **84,** 1750.
105. Hwang, J. H. and Han, Y. H. (2001). Dielectric Properties of Erbium Doped Barium Titanate, *Japanese Journal of Applied Physics* **40**, 676–679.
106. Sakabe, Y., Hamahi, Y., Sano, H. and Wada, N. (2002). Effects of Rare-Earth Oxides on the Reliability of X7R Dielectrics, *Japanese Journal of Applied Physics* **41,** 5668–5673.
107. Kishi, H. Mizuno, Y. and Chazono, H. (2003). Base-Metal Electrode-Multilayer Ceramic Capacitors: Past, Present and Future Perspectives, *Japanese Journal of Applied Physics* **42**, 1–15.
108. Mizuno, Y., Kishi. H., Ohnuma. K., Ishikawa. T., Ohsato, H. (2007). Effect of site occupancies of rare earth ions on electrical properties in Ni-MLCC based on $BaTiO_3$, *Journal of the European Ceramic Society* **27**, 4017–4020.
109. Vendik, O. G. and Zubko, S. P. (2000). Ferroelectric phase transition and maximum dielectric permittivity of displacement type ferroelectrics $Ba_xSr_{1-x}TiO_3$, *Journal of Applied Physics* **88**, 5343.
110. Levin, I., Krayzman, V. and Woicik, J. C. (2013). Local-structure origins of the sustained Curie temperature in $(Ba,Ca)TiO_3$ ferroelectrics, *Applied Physics Letters* **102**, 162906.
111. Fu, D., Itoh, M., Koshihara, S. Y., Kosugi, T. and Tsuneyuki, S. (2008). Anomalous phase diagram of ferroelectric $(Ba,Ca)TiO_3$ single crystals with giant electromechanical response. *Physical Review Letters* **100**, 227601.
112. Dawson, J. A., Sinclair, D. C., Harding, J. H. and Freeman, C. L. (2014). A-site strain and displacement in $Ba_{1-x}Ca_xTiO_3$ and $Ba_{1-x}Sr_xTiO_3$ and the consequences for the Curie temperature, *Chemistry of Materials* **26**, 6104–6112.
113. Han, Y. H., Appleby, J. B. and Smyth, D. M. (1987). Calcium as an acceptor impurity in $BaTiO_3$, Journal of the American Ceramic Society **70**, 96-100.
114. Zhang L., Thakur, O. P. and Feteira A. (2007). Comment on the use of calcium as a dopant in X8R $BaTiO_3$-based ceramics, *Applied Physics Letters* **90**, 142914.
115. Sághi-Szabó, G., Cohen, R. E. and Krakauer, H. (1999). First-principles study of piezoelectricity in tetragonal $PbTiO_3$ and $PbZr_{1/2}Ti_{1/2}O_3$, *Physical Review B* **59**, 12771-12776.
116. Su, B. and Button, T. W. (2004). Microstructure and dielectric properties of Mg-doped barium strontium titanate ceramics, Journal of Applied Physics **95**, 1382-1385.
117. Kishi, H., Kohzu, N., Sugino, J. et al. (1999). The Effect of Rare-earth (La, Sm, Dy, Ho and Er) and Mg on the Microstructure in $BaTiO_3$, *Journal of the European Ceramic Society* **19**, 1043-1046.
118. Kim, C.-H., Park, K.-J., Yoon, Y.-J. et al. (2008). Role of yttrium and magnesium in the formation of core-shell structure of $BaTiO_3$ grains in MLCC, *Journal of the European Ceramic Society* **28**, 1213–1219.
119. Yoon, S.-H., Randall, C. A. and Hur, K.-H. (2009). Effect of Acceptor (Mg) Concentration on the Resistance Degradation Behavior in Acceptor (Mg)-Doped $BaTiO_3$ Bulk Ceramics: I. Impedance Analysis, *Journal of the American Ceramic Society* **92**, 1758–1765.
120. Shvartsman, V.V. and Lupascu, D.C. (2012). Lead-Free relaxor ferroelectrics, Journal of the American Ceramic Society **95**, 1.

121. Dobal, P. S., Dixit, A., Katiyar, R. S. et al. (2001). Micro-Raman scattering and dielectric investigations of phase transition behavior in the $BaTiO_3$-$BaZrO_3$ system, *Journal of Applied Physics* **89**, 8085.
122. Simon, A., Ravez, J. and Maglione, M. (2004). The crossover from a ferroelectric to a relaxor state in lead-free solid solutions, *Journal of Physics Condensed Matter* **16**, 963.
123. Dong, L., Stone, D. S. and Lakes, R. S. (2012). Enhanced dielectric and piezoelectric properties of $xBaZrO_3$-$(1-x)BaTiO_3$ ceramics, *Journal of Applied Physics* **111**, 084107.
124. Lei, C., Bokov, A. A. and Ye, Z.-G. (2007). Ferroelectric to relaxor crossover and dielectric phase diagram in the $BaTiO_3$-$BaSnO_3$ system, *Journal of Applied Physics* **101**, 084105.
125. Anwar, S., Sagdeo, P. R. and Lalla, N. P. (2007). Study of the relaxor behavior in $BaTi_{1-x}Hf_xO_3$ ($0.20 \leq x \leq 0.30$) ceramics, *Solid State Sci.* **9**, 1054.
126. Li, J., Zhang, D., Qin, S. et al. (2016). Large room temperature electrocaloric effect in lead-free $BaHf_xTi_{1-x}O_3$ ceramics under low electric field, *Acta Materialia* **115**, 58.
127. Canu, G., Confalonieri, G., Deluca, M. et al. (2018). Structure-property correlations and origin of relaxor behaviour in $BaCe_xTi_{1-x}O_3$, *Acta Materialia* **152**, 258-268.
128. Pan, M. J. and Randall, C. A. (2010). A Brief Introduction to Ceramic Capacitors, *IEEE Electr. Insul. Mag.* **26**, 44-50.
129. Burns, G. and Dacol, F. H. (1983). Crystalline ferroelectrics with glassy polarization behaviour, *Physical Review B* **28**, 2527-2530.
130. Samara, G. A. (2003). The relaxational properties of compositionally disordered ABO_3 perovskites, *Journal of Physics: Condensed Matter* **15**, R367-R411.
131. Hou, D., Zhao, C., Paterson, A. R., Li, S. and Jones, J. L. (2018). Local structures of perovskite dielectrics and ferroelectrics via pair distribution function analysis, *Journal of the European Ceramic Society* **38**, 971-987.
132. Hennings D., Schnell, A. and Simon, G. (1982). Diffuse ferroelectric phase transitions in $Ba(Ti_{1-y}Zr_y)O_3$ ceramics, *Journal of the American Ceramic Society* **65**, 539.
133. Hansen P., Hennings, D. and Schreinemacher, H. (1998). High-K dielectric ceramics from donor/acceptor-codoped $(Ba_{1-x}Ca_x)Ti_{1-y}Zr_y)O_3$ (BCTZ), *Journal of the American Ceramic Society* **81**, 1369–73.
134. Shvartsman, V. V., Zhai, J. and Kleemann, W. (2009). The Dielectric Relaxation in Solid Solutions $BaTi_{1-x}Zr_xO_3$, *Ferroelectrics* **379,** 77–85.
135. Shvartsman, V. V., Dec, J., Xu, Z. K. et al. (2008). Crossover from ferroelectric to relaxor behavior in $BaTi_{1-x}Sn_xO_3$ solid solutions, *Phase Transitions* **81**, 1013–1021.
136. Gao, J. H., Liu, Y., Wang, Y. et al, (2017). Designing High Dielectric Permittivity Material in Barium Titanate, *J. Phys. Chem. C,* **121**, 13106−13113.
137. Kleemann, W., Miga, S., Dec, J. and Zhai, J. (2013). Crossover from ferroelectric to relaxor and cluster glass in $BaTi_{1-x}Zr_xO_3$ ($x=0.25$–0.35) studied by non-linear permittivity, *Applied Physics Letters* **102**, 232907
138. Maiti, T., Guo, R. and Bhalla, A. S. (2008). Structure-property phase diagram of $BaZr_xTi_{1-x}O_3$ system. *Journal of the American Ceramic Society* **91**, 1769–1780.
139. Filipič, C., Kutnjak, Z., Pirc, R., Canu, G. and Petzelt, J. (2016). $BaZr_{0.5}Ti_{0.5}O3$: Lead-free relaxor ferroelectric or dipolar glass, *Physical Review B* **93**, 224105.
140. Petzelt, J., Nuzhnyy, D., Savinov, M., et al (2014). Broadband Dielectric Spectroscopy of $Ba(Zr,Ti)O_3$: Dynamics of Relaxors and Diffuse Ferroelectrics, *Ferroelectrics* **469,** 14-25.

141. Akbarzadeh, A. R., Kornev, I., Malibert, C., Bellaiche, L. and Kiat, J. M. (2005). Combined theoretical and experimental study of the low-temperature properties of $BaZrO_3$, *Physical Review B* **72**, 205104.
142. Lu, D. Y., Han, D.-D. and Sun, X.-Y. (2012). Mutual solid solubility and phase equilibrium in the system $BaTiO_3$-$BaCeO_3$, *Japanese Journal of Applied Physics* **51**, 071501.
143. Miao, S., Pokorny, J. and Pasha, U.M. (2009). Polar order and diffuse scatter in $Ba(Ti_{1-x}Zr_x)O_3$ ceramics, *Journal of Applied Physics* **106**, 114111.
144. Buscaglia, V., Tripathi, S., Petkov, V. et al. (2014). Average and local atomic-scale structure in $BaZr_xTi_{1-x}O_3$ ($x = 0.10, 0.20, 0.40$) ceramics by high-energy x-ray diffraction and Raman spectroscopy, *J. Phys.: Condens. Matter* **26**, 065901.
145. Buscaglia, V., Buscaglia, M.T., Viviani, M. et al. (2006). Grain size and grain boundary-related effects on the properties of nanocrystalline barium titanate ceramics, *Journal of the European Ceramic Society* **26** 2889–2898.
146. Dul'kin, A. E., Petzelt, J., Kamba, S., Mojaev, E. and Roth, M. (2010). Relaxor-like behavior of crystals from acoustic emission study, *Applied Physics Letters* **97**, 032903.
147. Burns, G. and Dacol, F. H. (1982). Polarization of the cubic phase of $BaTiO_3$, *Solid State Communications* **42**, 9.
148. Laulhe, C., Hippert, F., Bellissent, R. and Cuello G. J. (2009). Local structure in $BaTi_{1-x}Zr_xO_3$ relaxors from neutron pair distribution function analysis, *Physical Review B* **79**, 064104.
149. Levin, I., Cockayne, E., Krayzman, V., Woicik, J. C., Lee, S. and Randall, C. A. (2011). Local structure of $Ba(Ti,Zr)O_3$ perovskite-like solid solutions and its relation to the bandgap behavior, *Physical Review B* **83**, 094122.
150. Laulhé, C., Pasturel, A., Hippert, F. and Kreisel, J. (2010). Random local strain effects in homovalent-substituted relaxor ferroelectrics: A first-principles study of $BaTi_{0.74}Zr_{0.26}O_3$, *Physical Review B* **82**, 132102.
151. Liu, Z. K., Li, X., and Zhang, Q. M. (2012). Maximizing the number of coexisting phases near invariant critical points for giant electrocaloric and electromechanical responses in ferroelectrics, *Applied Physics Letters* **101**, 082904.
152. Qian, X. S., Ye, H. J., Zhang, Y. T. et al. (2014). Giant electrocaloric response over a broad temperature range in modified $BaTiO_3$ ceramics, *Advanced Functional Materials* **24**, 1300.
153. Luo Z., Zhang D., Liu Y., et al. (2014). Enhanced electrocaloric effect in lead-free $BaTi_{1-x}Sn_xO_3$ ceramics near room temperature, *Applied Physics Letters* **105**, 102904.
154. Beuerlein, M. A., Kumar, N., Usher, T.-M. et al. (2016). Current Understanding of Structure-Processing-Property Relationships in $BaTiO_3$-$Bi(M)O_3$ Dielectrics, *Journal of the American Ceramic Society* 99, 2849-2870.
155. Hou, D., Usher, T.-M., Zhou, H. et al. (2017). Temperature-induced local and average structural changes in $BaTiO_3$-$xBi(Zn_{1/2}Ti_{1/2})O_3$ solid solutions: The origin of high temperature dielectric permittivity, *J. App. Phys.* **122**, 064103.
156. Zeb, A. and Milne, S. J. (2015). High temperature dielectric ceramics: a review of temperature-stable high-permittivity perovskites, *J Mater Sci: Mater Electron* **26**, 9243–9255.
157. Ogihara, H., Randall, C. A. and Trolier-McKinstry, S. (2009). High-Energy Density Capacitors Utilizing $0.7BaTiO_3$–$0.3BiScO_3$ Ceramics, *Journal of the American Ceramic Society* **92**, 1719–24.

158. Xiong, B., Hao, H., Zhang, S., Liu, H. and Cao, M. (2011). Structure, dielectric properties and temperature stability of $BaTiO_3$–$Bi(Mg_{1/2}Ti_{1/2})O_3$ perovskite solid solutions, *Journal of the American Ceramic Society* **94**, 3412–3417.
159. Zeb, A. and Milne, S. J. (2014). Low variation in relative permittivity over the temperature range 25–450°C for ceramics in the system $(1-x)[Ba_{0.8}Ca_{0.2}TiO_3]$–$x[Bi(Zn_{0.5}Ti_{0.5})O_3]$, *Journal of the European Ceramic Society* **34**, 1727–1732.
160. Zeb, A. and Milne, S. J. (2014). Temperature-stable dielectric properties from 20 °C to 430 °C in the system $BaTiO_3$-$Bi(Mg_{0.5}Zr_{0.5})O_3$*, Journal of the European Ceramic Society* **34** 3159–3166.
161. Muhammad, R., Iqbal, Y. and Reaney, I. M. (2016). $BaTiO_3$–$Bi(Mg_{2/3}Nb_{1/3})O_3$ Ceramics for High-Temperature Capacitor Applications, *Journal of the American Ceramic Society* **99**, 2089–2095.
162. Raengthon, N., Sebastian, T., Cumming, D., Reaney, I. M. and Cann, D. P. (2012). $BaTiO_3$–$Bi(Zn_{1/2}Ti_{1/2})O_3$–$BiScO_3$ Ceramics for High-Temperature Capacitor Applications, *Journal of the American Ceramic Society* **95,** 3554–61.
163. Datta, K., Thomas, P. A. and Roleder, K. (2010). Anomalous phase transitions of lead-free piezoelectric $xNa_{0.5}Bi_{0.5}TiO_3$-$(1-x)$BaTiO3 solid solutions with enhanced phase transition temperatures, *Physical Review B* **82**, 224105.
164. Bharadwaja, S. S. N., Kim, J. R., Ogihara, H. et al. (2011). Critical slowing down mechanism and reentrant dipole glass phenomena in $(1-x)BaTiO_3$-$xBiScO_3$ $(0.1 \leq x \leq 0.4)$: The high energy density dielectrics, *Physical Review B* **83**, 024106.
165. Guo, H. Y., Lei, C. and Ye, Z.-G. (2008). Re-entrant type relaxor behavior in $(1-x)BaTiO_3$–$xBiScO_3$ solid solution, *Applied Physics Letters* **92**, 172901.
166. Chen, L. L., Hui, K. Z., Wang, H. X. et al. (2019). Effects of Ho_2O_3 doping and sintering temperature on the core-shell structure of X9R Nb-modified $BaTiO_3$-$(Bi_{0.5}Na_{0.5})TiO_3$ ceramics, *Journal of the European Ceramic Society* **39**, 3710–3715.
167. Wang, S.-F., Li, J.-H., Hsu, Y.-F. et al. (2013). Dielectric properties and microstructures of non-reducible high-temperature stable X9R ceramics, *Journal of the European Ceramic Society* **33**, 1793–1799.
168. Buscaglia, M. T., Viviani, M., Zhao, Z., Buscaglia, V. and Nanni, P. (2006). Synthesis of $BaTiO_3$ core-shell particles and fabrication of dielectric ceramics with local graded structure, *Chem. Mater.* **18**, 4002-4010.
169. Wu, L., Wang, X., Gong, H. et al. (2015). Core-satellite $BaTiO_3$@$SrTiO_3$ assemblies for a local compositionally graded relaxor ferroelectric capacitor with enhanced energy storage density and high energy efficiency, *J. Mater. Chem. C* **3**, 750.
170. Airimioaei, M., Buscaglia, M. T., Tredici, I., et al. (2017). $SrTiO_3$-$BaTiO_3$ nanocomposites with temperature independent permittivity and linear tunability fabricated using field-assisted sintering from chemically synthesized powders, *J. Mater. Chem. C* **5**, 9028-9036.
171. Jeon, S.-C., Lee, C.-S. and Kang, S.-L. (2012). The Mechanism of Core/Shell Structure Formation During Sintering of $BaTiO_3$-Based Ceramics, *Journal of the American Ceramic Society* **95**, 2435–2438.
172. Armstrong, T. R., Morgens, L. E., Maurice, A. K. and Buchanan, R. C. (1989). Effects of Zirconia on Microstructure and Dielectric Properties of Barium Titanate Ceramics, *Journal of the American Ceramic Society* **72**, 605-611.

173. Hennings, D. F. K. and Schreinemacher, B. S. (1994). Temperature-Stable Dielectric Materials in the System $BaTiO_3$-Nb_2O_5-Co_3O_4, *Journal of the European Ceramic Society* **14**, 463471.
174. Chazono, H. and Kishi, H. (1999). Sintering Characteristics in $BaTiO_3$–Nb_2O_5–Co_3O_4 Ternary System: I, Electrical Properties and Microstructure, *Journal of the American Ceramic Society* **82**, 2689–97.
175. Sato, S., Nakano, Y., Sato, A. and Nomura, T. (1999). Mechanism of Improvement of Resistance Degradation in Y-doped $BaTiO_3$ Based MLCCs with Ni Electrodes under Highly Accelerated Life Testing, *Journal of the European Ceramic Society* **19**, 1061-1065.
176. Hennings, D. and Rosenstein, G. (1984). Temperature-Stable Dielectrics Based on Chemically Inhomogeneous $BaTiO_3$, *Journal of the American Ceramic Society* **67**, 249.
177. Armstrong, T. R. and Buchanan, R. C. (1990). Influence of Core-Shell Grains on the Internal Stress State and Permittivity Response of Zirconia-Modified Barium Titanate, *Journal of the American Ceramic Society* **73**, 1268–73.
178. Chazono, H. and Kishi, H. (2000). Sintering Characteristics in the $BaTiO_3$–Nb_2O_5–Co_3O_4 Ternary System: II, Stability of So-called "Core–Shell" Structure, *Journal of the American Ceramic Society* **83**, 101–106.
179. Kim, J.-S. and Kang, S.-J. L. (1999). Formation of Core–Shell Structure in the $BaTiO_3$–$SrTiO_3$ System, *Journal of the American Ceramic Society* **82**, 1085–88.
180. Mizuno, Y., Okino, Y., Kohzu, N., Chazono, H. and Kishi, H. (1998). Influence of the microstructure evolution on electrical properties of multilayer capacitor with Ni electrode, *Japanese Journal of Applied Physics* **37**, 5227.
181. Kishi, H., Okino, Y., Honda, M., et al. (1997). The effect of MgO and rare-earth oxide on formation behavior of core-shell structure in $BaTiO_3$, *Japanese Journal of Applied Physics* **36**, 5954-5997.
182. Zhang, Y., Wang, X., Tian, Z., Hur, K.-H. and Li, L. (2011). Preparation of BME MLCC Powders by Aqueous Chemical Coating Method, *Journal of the American Ceramic Society* **94**, 3286–3290.
183. Yao, G. F., Wang, X. H., Wu, Y. Y. and Li, L. T. (2012), Nb-Doped $0.9BaTiO_3$–$0.1(Bi_{0.5}Na_{0.5})TiO_3$ Ceramics with Stable Dielectric Properties at High Temperature, *Journal of the American Ceramic Society*, **95**, 614–618.
184. Zhang, Y., Cao, M., Yao, Z. et al. (2015). Effects of silica coating on the microstructures and energy storage properties of $BaTiO_3$ ceramics, *Mat. Res. Bull.* **67**, 70–76.
185. Wang, X., Zhang, Y., Son, X. et al., (2012). Glass additive in barium titanate ceramics and its influence on electrical breakdown strength in relation with energy storage properties, *Journal of the European Ceramic Society* **32**, 559-567.
186. Liu, B., Wang, X., Zhang, R. and Li, L. (2017). Grain size effect and microstructure influence on the energy storage properties of fine-grained $BaTiO_3$-based ceramics, *Journal of the American Ceramic Society* **100**, 3599–3607.
187. Yuan, Q., Cui J., Wang Y., Ma R. and H. Wang (2017). Significant enhancement in breakdown strength and energy density of the $BaTiO_3$/$BaTiO_3$@SiO_2 layered ceramics with strong interface blocking effect, *Journal of the European Ceramic Society* **37**, 4645–4652.
188. Hornebecq, V., Huber, C., Maglione, M., et al. (2004). Dielectric properties of pure $(BaSr)TiO_3$ and composites with different grain sizes ranging from the nanometer to the micrometer, *Advanced Functional Materials* **14**, 899–904.

189. Mornet, S., Elissalde, C., Hornebecq, V. et al. (2005). Controlled growth of silica shell on $Ba_{0.6}Sr_{0.4}TiO_3$ nanoparticles used as precursors of ferroelectric composites, *Chemistry of Materials*, **17**, 4530–4536.
190. Chung, U. C., Elissalde, C., Mornet, S. et al. (2009). Controlling internal barrier in low loss $BaTiO_3$ supercapacitors. *Applied Physics Letters*, **94**, art. no. 072903.
191. Chung, U. C., Elissalde, C, Mompiou, F. et al. (2010). Interface investigation in nanostructured $BaTiO_3$/silica composite ceramics, *Journal of the American Ceramic Society* **93**, 865–874.
192. Yuan, Q., Li, G., Yao, F.-Z. et al. (2018). Simultaneously achieved temperature-insensitive high energy density and efficiency in domain engineered $BaTiO_3$-$Bi(Mg_{0.5}Zr_{0.5})O_3$ lead-free relaxor ferroelectrics, *Nano Energy* **52**, 203–210.
193. Yuan, Q., Yao, F.-Z., Wang, Y., Ma, R. and Wang, H. (2017). Relaxor ferroelectric $0.9BaTiO_3$–$0.1Bi(Zn_{0.5}Zr_{0.5})O_3$ ceramic capacitors with high energy density and temperature stable energy storage properties, *J. Mater. Chem. C* **5**, 9552-9558.
194. Zhou, M., Liang, R., Zhou, Z. and Dong, X. (2018). Novel $BaTiO_3$-based lead-free ceramic capacitors featuring high energy storage density, high power density, and excellent stability, J. *Mater. Chem. C* **6**, 8528-8537.
195. Yang, H., Yan, F. and Lin, Y. (2017). Lead-free $BaTiO_3$-$Bi_{0.5}Na_{0.5}TiO_3$-$Na_{0.73}Bi_{0.09}NbO_3$ relaxor ferroelectric ceramics for high energy storage, *Journal of the European Ceramic Society* **37**, 3303-3311.
196. Li, W.-B., Zhou, D. and Pang, L.-X. (2017). Enhanced energy storage density by inducing defect dipoles in lead free relaxor ferroelectric $BaTiO_3$-based ceramics, *Applied Physics Letters* **110**, 132902.
197. Wang, T., Jin, L., Li, C., Hu, Q. and Wei, X. (2015). Relaxor Ferroelectric $BaTiO_3$–$Bi(Mg_{2/3}Nb_{1/3})O_3$ Ceramics for Energy Storage Application, *Journal of the American Ceramic Society* **98**, 559–566.
198. Wu, L., Wang, X. and Li, L. (2016). Lead-free $BaTiO_3$–$Bi(Zn_{2/3}Nb_{1/3})O_3$ weakly coupled relaxor ferroelectric materials for energy storage, *RSC Advances* **6**, 14273-14282.
199. Shen, Z. B., Wang, X.H., Luo, B.C. and Li, L. T. (2015). $BaTiO_3$–$BiYbO_3$ perovskite materials for energy storage applications, *J. Mater. Chem. A* **3**, 18146-18153.
200. Song, Z., Liu, H., Zhang, S. et al. (2014). Effect of grain size on the energy storage properties of $(Ba_{0.4}Sr_{0.6})TiO_3$ paraelectric ceramics, *Journal of the European Ceramic Society* **34**, 1209–1217.
201. Song, Z., Zhang, S., Liu, H. et al., (2015). Improved Energy Storage Properties Accompanied by Enhanced Interface Polarization in Annealed Microwave-Sintered BST, *Journal of the American Ceramic Society* **98**, 3212–3222.
202. Huang, Y. H., Wu Y. J., Qiu W. J., Li J. and X. M. Chen (2015). Enhanced energy storage density of $Ba_{0.4}Sr_{0.6}TiO_3$–MgO composite prepared by spark plasma sintering, *Journal of the European Ceramic Society* **35**, 1469–1476.
203. Yang, H., Yan, F., Lin, Y. and Wang T. (2018). Enhanced energy storage properties of $Ba_{0.4}Sr_{0.6}TiO_3$ lead-free ceramics with Bi_2O_3-B_2O_3-SiO_2 glass addition, *Journal of the European Ceramic Society* **38** 1367–1373.
204. Tagantsev, A. K., Sherman, V. O., Astafiev, K. F., Venkatesh, J. and Setter, N. (2003). Ferroelectric Materials for Microwave Tunable Applications, *Journal of Electroceramics* **11**, 5.

205. Zhang, Q. W., Zhai, J. W. and Kong, L. B. (2012). Relaxor Ferroelectric Materials for Microwave Tunable Applications, J. Adv. Dielectr., **1**, 1230002.
206. Tang, X. G., Chew, K.-H. and Chan, H. L. W. (2004). Diffuse phase transition and dielectric tunability of $Ba(Zr_yTi_{1-y})O_3$ relaxor ferroelectric ceramics, *Acta Materialia* **52**, 5177–5183.
207. Chang, W. and Sengupta, L. (2002). MgO-mixed $Ba_{0.6}Sr_{0.4}TiO_3$ bulk ceramics and thin films for tunable microwave applications, *Journal of Applied Physics* **92**, 3941.
208. Chung, U. C., Elissalde, C., Maglione, M., et al. (2008). Low-losses, highly tunable $Ba_{0.6}Sr_{0.4}TiO_3$/MgO composite, *Applied Physics Letters* **92**, 042902.
209. Moulson, A. J. and Herbert, J. M. (1990). Electroceramics, Chapman & Hall, London.
210. Liu, W. and Ren, X. (2009) Large piezoelectric effect in Pb-free ceramics. *Phys. Rev. Lett.* **103**, 257602.
211. Ehmke, M. C., Ehrlich, S. N., Blendell, J. E. and Bowman, K. J. (2012). Phase coexistence and ferroelastic texture in high strain $(1-x)Ba(Zr_{0.2}Ti_{0.8})O_3–x(Ba_{0.7}Ca_{0.3})TiO_3$ piezoceramics, *Journal of Applied Physics* **111**, 124110.
212. Keeble, D. S., Benabdallah, F., Thomas, P. A., Maglione, M. and Kreisel, J. (2013). Revised structural phase diagram of $(Ba_{0.7}Ca_{0.3}TiO_3)$-$(BaZr_{0.2}Ti_{0.8}O_3)$, *Applied Physics Letters* **102**, 092903.
213. Acosta, M., Novak, N., Jo, W. and Rödel, J. (2014). Relationship between electromechanical properties and phase diagram in the $Ba(Zr_{0.2}Ti_{0.8})O_3–x(Ba_{0.7}Ca_{0.3})TiO_3$ lead-free piezoceramic, *Acta Materialia* **80**, 48.
214. Damjanovic, D. (2013). Contributions to the Piezoelectric Effect in Ferroelectric Single Crystals and Ceramics, *Applied Physics Letters* **102**, 092903.
215. Zhang, L., Zhang, M., Wang, L. et al. (2014). Phase transitions and the piezoelectricity around morphotropic phase boundary in $Ba(Zr_{0.2}Ti_{0.8})O_3$-$x(Ba_{0.7}Ca_{0.3})TiO_3$ lead-free solid solution, *Applied Physics Letters* **105**, 162908.
216. Acosta, M., Khakpash, N., Someya, T. et al. (2015). Origin of the large piezoelectric activity in $(1-x)Ba(Zr_{0.2}Ti_{0.8})O_3$-$x(Ba_{0.7}Ca_{0.3})TiO_3$ ceramics, *Physical Review B* **91**, 104108.
217. Wang, P., Li, Y. X. and Lu, Y. Q. (2011). Enhanced piezoelectric properties of $(Ba_{0.85}Ca_{0.15})(Ti_{0.9}Zr_{0.1})O_3$ lead-free ceramics by optimizing calcination and sintering temperature, *Journal of the European Ceramic Society* **31**, 2005–2012.
218. Bai, Y., Matouseka, A., Tofela P. et al., (2015). $(Ba,Ca)(Zr,Ti)O_3$ lead-free piezoelectric ceramics—The critical role of processing on properties, *Journal of the European Ceramic Society* **35**, 3445–3456.
219. Wu, J., Xiao, D., Wu, W. et al., (2012). Composition and poling condition-induced electrical behavior of $(Ba_{0.85}Ca_{0.15})(Ti_{1-x}Zr_x)O_3$ lead-free piezoelectric ceramics, *Journal of the European Ceramic Society* **32**, 891–898.
220. Praveen, J. P., Karthik, T., James, A.R., et al. (2015). Effect of poling process on piezoelectric properties of sol–gel derived BZT–BCT ceramics, *Journal of the European Ceramic Society* **35**, 1785–1798.
221. Hao, J. G., Bai, W. F., Li, W. and Zhai, J. W. (2012). Correlation Between the Microstructure and Electrical Properties in High-Performance $(Ba_{0.85}Ca_{0.15})(Zr_{0.1}Ti_{0.9})O_3$ Lead-Free Piezoelectric Ceramics, *Journal of the American Ceramic Society* **95**, 1998–2006.
222. Li, B., Ehmke, M. C., Blendell, J. E. and Bowman, K. J. (2013). Optimizing electrical poling for tetragonal, lead-free BZT–BCT piezoceramic alloys, *Journal of the European Ceramic Society* **33**, 3037–3044.

223. Bao, H. X., Zhou, C., Xue, D. Z., Gao, J. G. and Ren, X. B. (2010). A modified lead-free piezoelectric BZT–xBCT system with higher T_C, *Journal of Physics D: Applied Physics* **43**, 465401.
224. Liu, Y., Chang, Y., Li, F., et al. (2017). Exceptionally high piezoelectric coefficient and low strain hysteresis in grain-oriented (Ba,Ca)(Ti,Zr)O_3 through integrating crystallographic texture and domain engineering. *ACS Applied Materials & Interfaces* **9**, 29863-71.
225. Wang, D., Jiang, Z., Yang, B. et al., (2014). Phase Diagram and Enhanced Piezoelectric Response of Lead-Free $BaTiO_3$–$CaTiO_3$–$BaHfO_3$ System, *Journal of the American Ceramic Society* **97,** 3244–3251.
226. Zhu, L. F., Zhang, B. P., Zhao, X. K. et al. (2013). Enhanced Piezoelectric Properties of $(Ba_{1-x}Ca_x)(Ti_{0.92}Sn_{0.08})O_3$ Lead-Free Ceramics, *Journal of the American Ceramic Society* **96**, 241–245.
227. Zhu, L. F., Zhang, B. P., Zhao, X. K. et al. (2013). Phase transition and high piezoelectricity in (Ba, Ca)$(Ti_{1-x}Sn_x)O_3$ lead-free ceramics, *Applied Physics Letters* **103**, 72905.
228. Zhu, L. F., Zhang, B. P., Zhao, L. and Li, J. F. (2014). High piezoelectricity of $BaTiO_3$-$CaTiO_3$-$BaSnO_3$ lead-free ceramics, *J Mater Chem C* **2**, 4764.
229. Zhu, L. F., Zhang, B. P., Zhao L., Li S., et al. (2016). Large piezoelectric effect of (Ba,Ca)TiO_3–xBa(Sn,Ti)O_3 lead free ceramics, *Journal of the European Ceramic Society* **36**, 1017–1024.
230. Janbua W., Bongkarn T., Kolodiazhny T. and Vittayakorn, N. (2017). High piezoelectric response and polymorphic phase region in the lead-free piezoelectric $BaTiO_3$–$CaTiO_3$–$BaSnO_3$ ternary system, *RSC Advances*, **7**, 30166.
231. Yao, Y.G., Zhou, C., Lv, D. et al. (2012). Large piezoelectricity and dielectric permittivity in $BaTiO_3$-x$BaSnO_3$ system: The role of phase coexisting, *Europhysics Letters* **98**, 27008.
232. Zhao, C., Wu, H., Li, F. et al., (2018). Practical High Piezoelectricity in Barium Titanate Ceramics Utilizing Multiphase Convergence with Broad Structural Flexibility, *Journal of the American Chemical Society* **140**, 15252−15260.
233. Zhao, C.L., Wu, W.J., Wang, H. and Wu J. G. (2016). Site engineering and polarization characteristics in $(Ba_{1-y}Ca_y)(Ti_{1-x}Hf_x)O_3$ lead-free ceramics, *Journal of Applied Physics* **119**, 024108.
234. Randall, C. A., Wang, S. F., Laubscher, D., Dougherty, J. P. and Huebner, W. (1993). Structure property relationships in core-shell $BaTiO_3$-LiF ceramics, *Journal of Materials Research* **8**, 871-879
235. Yang, W. G., Zhang, B. P., Ma N. and Zhao, L. (2012). High piezoelectric properties of $BaTiO_3$–xLiF ceramics sintered at low temperatures, *Journal of the European Ceramic Society* **32**, 899–904.
236. Kimura, T., Dong, Q., Yin, S. et al. (2013). Synthesis and piezoelectric properties of Li-doped $BaTiO_3$ by a solvothermal approach, *Journal of the European Ceramic Society* **33**, 1009–1015
237. Ma, N., Zhang, B.-P., Yang, W.-G. and Guo, D. (2012). Phase structure and nano-domain in high performance of $BaTiO_3$ piezoelectric ceramics, *Journal of the European Ceramic Society* **32**, 1059–1066.
238. Shen, Z.-Y. and Li, J.-F. (2010). Enhancement of piezoelectric constant d_{33} in $BaTiO_3$ ceramics due to nano-domain structure, *Journal of Ceramic Society of Japan* **118**, 940-943.
239. Shaw, T. M., Trolier-McKinstry, S. and McIntyre, P. C. (2000). The properties of ferroelectric films at small dimensions, *Annual Review of Materials Science* **30**, 263-298.

240. Ihlefeld, J. F., Harris, D. T., Keech, R. et al. (2016). Scaling Effects in Perovskite Ferroelectrics: Fundamental Limits and Process-Structure-Property Relations, *Journal of the American Ceramic Society* **99**, 2537–2557.
241. Kinoshita, K. and Yamaji, A. (1976). Grain-Size Effects on Dielectric Properties in Barium-Titanate Ceramics, *Journal of Applied Physics* **47**, 371-3.
242. Randall, C. A., Kim, N., Kucera, J.-P., Cao, W. W. and Shrout, T. R. (1998). Intrinsic and Extrinsic Size Effects in Fine-Grained Morphotropic-Phase-Boundary Lead Zirconate Titanate Ceramics, *Journal of the American Ceramic Society* **81**, 677–88.
243. Arlt, G., Hennings, D. and de With, G. (1985). Dielectric-Properties of Fine-Grained Barium-Titanate Ceramics, *Journal of Applied Physics* **58**, 1619–25.
244. Frey, M. H., Xu, Z., Han, P. and Payne, D. A. (1998). The Role of Interfaces on an Apparent Grain Size Effect on the Dielectric Properties for Ferroelectric Barium Titanate Ceramics, *Ferroelectrics* **206**, 337–53.
245. Takeuchi, T., Capiglia, C., Balakrishnan, N., Takeda, Y. and Kageyama, H. (2002). Preparation of fine-grained $BaTiO_3$ ceramics by spark plasma sintering, *Journal of Materials Research* **17**, 575.
246. Polotai, A. V., Ragulya, A. V. and Randall, C. A. (2003). Preparation and size effect in pure nanocrystalline barium titanate ceramics, *Ferroelectrics* **288**, 93.
247. Zhao, Z., Buscaglia, V., Viviani, M., et al. (2004). Grain-Size Effects on the Ferroelectric Behavior of Dense Nanocrystalline $BaTiO_3$ Ceramics, *Physical Review B* **70**, 024107.
248. Wang, X. H., Deng, X. Y., Wen, H. and Li, L. T. (2006). Phase transition and high dielectric constant of bulk dense nanograin barium titanate ceramics, *Applied Physics Letters* **89** 162902.
249. Buscaglia, M. T., Viviani, M., Buscaglia, V., et al. (2006). High Dielectric Constant and Frozen Macroscopic Polarization in Dense Nanocrystalline $BaTiO_3$ Ceramics, *Physical Review B* **73**, 064114.
250. Deng, X. Y., Wang, X. H., Wen, H. et al. (2006). Ferroelectric properties of nanocrystalline barium titanate ceramics, *Applied Physics Letters* **88**, 252905.
251. Zhu, J. L., Jin, C. Q., Cao, W. W. and Wang, X. H. (2008). Phase transition and dielectric properties of $BaTiO_3$ nanograin ceramic under high pressure, *Applied Physics Letters* **92**, 242901.
252. Huan, Y., Wang, X. H., Fang, J. and Li, L. T. (2013). Grain Size Effects on Piezoelectric Properties and Domain Structure of $BaTiO_3$ Ceramics Prepared by Two-Step Sintering, *Journal of the American Ceramic Society* **96**, 3369–3371.
253. Shao, S. F., Zhang, J. L., Zhang, Z., et al. (2008). High piezoelectric properties and domain configuration in $BaTiO_3$ ceramics obtained through solid-state reaction route, *Journal of Physics D: Applied Physics* **41**, 125408.
254. Zheng, P., Zhang, J. L., Tan, Y. Q. and Wang, C. L. (2012). Grain-size effects on dielectric and piezoelectric properties of poled $BaTiO_3$ ceramics, *Acta Materialia* **60**, 5022–5030.
255. Huan, Y., Wang, X. H., Fang, J. and Li, L. T. (2014). Grain size effect on piezoelectric and ferroelectric properties of $BaTiO_3$ ceramics, *Journal of the European Ceramic Society* **34**, 1445–1448.
256. Tan, Y. Q., Zhang, J., Wu, Y. et al. (2015). Unfolding grain size effects in barium titanate ferroelectric ceramics, *Scientific Reports* **5,** 9953.
257. Hoshina, T., Hatta, S., Takeda, H. and Tsurumi, T. (2018). Grain size effect on piezoelectric properties of $BaTiO_3$ ceramics, *Japanese Journal of Applied Physics* **57**, 0902BB.

258. Gong, H. L., Wang, X. H., Zhang, S. P., Wen, H. and Li, L. T. (2014). Grain size effect on electrical and reliability characteristics of modified fine-grained $BaTiO_3$ ceramics for MLCCs, *Journal of the European Ceramic Society* **34**, 1733–1739.
259. Buscaglia, V. and Randall, C. A. (2020). Size and scaling effects in barium titanate. An overview, *Journal of the European Ceramic Society,* in press (2020). doi:https://doi.org/10.1016/j.jeurceramsoc.2020.01.02
260. Arlt, G. (1990). Twinning in ferroelectric and ferroelastic ceramics: stress relief, *Journal of Materials Science* **25**, 2655-2666.
261. Frey, M. H. and Payne, D. A. (1996). Grain-Size Effect on Structure and Phase Transformations for Barium Titanate, *Physical Review B* **54**, 3158–68.
262. Schilling, A., Adams, T. B., Bowman, R. M., Gregg, J. M., Catalan, G. and Scott, J. F. (2006). Scaling of domain periodicity with thickness measured in $BaTiO_3$ single crystal lamellae and comparison with other ferroics, *Physical Review B* **74**, 024115.
263. Schilling, A., Byrne, D., Catalan, G., Webber, K. G., Genenko, Y. A., Wu, G. S., Scott, J. F. and Gregg, J. M. (2009). Domains in Ferroelectric Nanodots, *Nano Letters* **9**, 3359-3364.
264. Arlt, G. and Pertsev, N. A. (1991). Force constant and effective mass of 90° domain walls in ferroelectric ceramics, *Journal of Applied Physics* **70**, 2283.
265. Ghosh, D., Sakata, A., Carter, J. et al. (2014). Domain Wall Displacement is the Origin of Superior Permittivity and Piezoelectricity in $BaTiO_3$ at Intermediate Grain Sizes, *Advanced Functional Materials* **24,** 885–896.
266. Curecheriu, L., Balmus, S.-B., Buscaglia, M. T. et al. (2012). Grain Size-Dependent Properties of Dense Nanocrystalline Barium Titanate Ceramics, *Journal of the American Ceramic Society* **95,** 3912–3921.
267. Emelyanov, A. Y., Pertsev, N. A., Hoffmann-Eifert, S., Böttger, U. and Waser, R. (2002). Grain-Boundary Effect on the Curie-Weiss Law of Ferroelectric Ceramics and Polycrystalline Thin Films: Calculation by the Method of Effective Medium, *Journal of Electroceramics* **9**, 5-16.
268. Curecheriu, L., Buscaglia, M. T., Buscaglia, V., Zhao, Z. and Mitoseriu, L. (2010). Grain size effect on the nonlinear dielectric properties of barium titanate ceramics, *Applied Physics Letters* **97**, 242909.
269. Padurariu, L., Curecheriu, L., Buscaglia, V. and Mitoseriu, L. (2012). Field-dependent permittivity in nanostructured $BaTiO_3$ ceramics: Modeling and experimental verification, *Physical Review B* **85**, 224111.
270. Su, Y., Kang, H., Wang, Y., Li, J. and Weng, G. J. (2017). Intrinsic versus extrinsic effects of the grain boundary on the properties of ferroelectric nanoceramics, *Physical Review B* **95**, 054121.
271. Fu, H.X. and Bellaiche, L. (2003). Ferroelectricity in Barium Titanate Quantum Dots and Wires, *Physical Review Letters* **91**, 257601.
272. Cai, Z. M., Wang, X. H., Hong, W., Luo, B. C., Zhao, Q. C. and Li, L. T. (2018). Grain size–dependent dielectric properties in nanograin ferroelectrics, *Journal of the American Ceramic Society* **101**, 5487–5496.
273. Dai B., Zheng P., Bai W. et al. (2018). Direct and converse piezoelectric grain-size effects in $BaTiO_3$ ceramics with different Ba/Ti ratios, *Journal of the European Ceramic Society* **38**, 4212–4219.
274. Zhong, W. L., Wang, Y. G., Zhang, P. L. and Qu, B. D. (1994). Phenomenological study of the size effect on phase transitions in ferroelectric particles, *Physical Review B* **50,** 698-703.

275. Ishikawa, K., Yoshikawa, K. and Okada, N. (1988). Size effect on the ferroelectric phase transitions of $PbTiO_3$ ultrafine particles, *Physical Review B* **37,** 5852-5855
276. McCauley, D., Newnham, R. E. and Randall, C. A. (1998). Intrinsic Size Effects in a Barium Titanate Glass-Ceramic, *Journal of the American Ceramic Society* **81,** 979–987.
277. Polking, M. J., Han, M. G., Yourdkhani, A. et al. (2012). Ferroelectric Order in Individual Nanometre-Scale Crystals, *Nature Materials* **11**, 700–9.

Figure captions

Figure 1. (a) Pseudo-binary phase diagram of the BaO–TiO_2 system under ambient air conditions. Reprinted from ref. 23 with permission of Wiley. Copyright American Ceramic Society (2007). (b) Variation of solubility regime as a function of oxygen partial pressure on the Ba- and Ti-rich sides of $BaTiO_3$ at 1200°C (left) and 1320°C (right). Reprinted from ref. 38 with permission of Wiley. Copyright American Ceramic Society (2008).

Figure 2. (a) Temperature dependence of crystal structure and relative dielectric constant along the a-axis direction in $BaTiO_3$ single crystal. Dielectric constant data from ref. 12. The Ti off centre displacement is exaggerated to be better observable.

Figure 3. Polarization (P) – electric field (E) ferroelectric polarization loop.

Figure 4. Equilibrium electrical conductivity of polycrystalline $BaTiO_3$ at 600-1000 °C with 50 °C interval. Data from ref. 45.

Figure 5. Schematic representation of the room-temperature dc resistivity as a function of the trivalent dopant concentration M^{3+} for ceramics heated in air. Adapted from ref. 54.

Figure 6. Phase diagram for the solid solution $BaTi_{1-x}Fe_xO_{3-\delta}$. T_C (IS) denotes Curie temperature obtained from impedance spectroscopy measurements. T_C (DSC) denotes Curie temperature obtained from differential scanning calorimetry. Reproduced from ref. 70 by permission of The Royal Society of Chemistry. Copyright (2006) The Royal Society of Chemistry.

Figure 7. Lattice parameters of 6H-$BaTi_{1-x-y}Fe^{3+}{}_xFe^{4+}{}_y\,O_{3-x/2}$ solid solution for air-quenched (filled circles) and slow-cooled in oxygen (open circles) samples after sintering in air. The lines correspond to Vegard law cell composition relationships for $BaTiO_3$-$BaFeO_{2.5}$ (upper lines) and $BaTiO_3$-$BaFeO_3$ (lower lines). Reprinted from ref. 74 with permission from Elsevier. Copyright (1998) Academic Press.

Figure 8. Compositional dependence of (a) unit-cell volume and (b) *c/a* ratio (filled symbols) and T_C (open symbols) in the $Ba_{1-x}Sr_xTiO_3$ (BST, blue) and $Ba_{1-x}Ca_xTiO_3$ (BCT, red) solid solutions. Reprinted from ref. 110, with the permission of AIP Publishing. (c) Phase diagram of the $Ba_{1-x}Ca_xTiO_3$ system. Reprinted figure with permission from ref.111. Copyright (2008) by the American Physical Society.

Figure 9. Phase diagram of $x$$BaZrO_3$-(1-$x$)$BaTiO_3$ ceramics with $0 \leq x \leq 0.20$. Reprinted from ref. 123, with the permission of AIP Publishing.

Figure 10. Variation of the Curie temperature in the $BaM_xTi_{1-x}O_3$ (M = Sn, Zr, Ce) solid solutions with respect to undoped $BaTiO_3$. Reprinted from ref. 127 with permission from Elsevier. Copyright (2018) Acta Materialia Inc.

Figure 11. (a) Temperature dependence of the relative dielectric constant (ε') of $BaTi_{1-x}Sn_xO_3$ (x = 0, 0.06, 0.12, 0.18, 0.24, 0.30) ceramics at 100 kHz. Composition $x = 0.12$ is close to the phase convergence point. (b) Temperature dependence of the real (ε') and imaginary parts (ε'') of the dielectric permittivity of ceramic with composition $x = 0.30$. Reprinted from ref. 124, with the permission of AIP Publishing.

Figure 12. Experimental pair distribution function of (a) $BaZrO_3$, (b) $BaTiO_3$, and (c) $BaTi_{0.68}Zr_{0.32}O_3$ at 300 K (crosses), compared with the PDF calculated from their crystallographic structures (lines). Inset in figure (b): zoom on the contribution of the Ti-O pairs within the TiO_6 octahedra in $BaTiO_3$. Reprinted figure with permission from ref. 148. Copyright (2009) by the American Physical Society.

Figure 13. Dielectric properties of $BaTiO_3$-$Bi(M)O_3$ ceramics. (a) $0.50BaTiO_3$–$0.25BiZn_{1/2}Ti_{1/2}O_3$–$0.25BiScO_3$. Reprinted from ref. 156 with permission INSERT PERMISSION DETAILS. (b) $0.9BaTiO_3$-$0.10Bi_{0.5}Na_{0.5}TiO_3$ with 1.5 mol. % Nb_2O_5 and different Ho content (frequency: 1 kHz). Reprinted from ref. 166 with permission from Elsevier. Copyright (2019) Elsevier Ltd.

Figure 14. (a) SEM and (b) TEM micrographs showing typical core-shell structures in a sample sintered at 1350 °C in wet H_2 for 2 h; (c) HRTEM image at the interface between a core and a shell; (d) STEM/EDS line profile showing the distribution of Y and Mg. Reprinted from ref. 171 with permission of Wiley. Copyright (2012) American Ceramic Society.

Figure 15. (a) Dielectric permittivity vs. electric field and (b) relative tunability vs. temperature for different $BaTi_{1-x}Zr_xO_3$ ceramics (x = 0.20-0.35). Reprinted from ref. 206 with permission from Elsevier. Copyright (2004) Acta Materialia Inc.

Figure 16. $xBa_{0.7}Ca_{0.3}TiO_3$-$(1-x)BaZr_{0.2}Ti_{0.8}O_3$ phase diagram. Reprinted from ref. 212 with the permission of AIP Publishing.

Figure 17. Contour plot of (a) small signal d_{33} and (b) large signal d_{33}^* as a function of temperature and composition in the $(1-x)Ba(Zr_{0.2}Ti_{0.8})O_3$-$x(Ba_{0.7}Ca_{0.3})TiO_3$ system. Reprinted from ref. 213 with permission from Elsevier. Copyright Acta Materialia Inc. (2014).

Figure 18. Map of piezoelectric coefficient d_{33} as a function of temperature and composition in the system $(1-x)Ba(Ti_{0.89}Sn_{0.11})O_3-x(Ba_{0.70}Ca_{0.30})TiO_3$. Reprinted with permission from ref. 232. Copyright (2018) American Chemical Society.

Figure 19. Room temperature dielectric constant of $BaTiO_3$ ceramics as a function of grain size. Data collected from different authors. HPS: hot pressing sintering, MAP: multi-anvil press, CSM: combined sintering method, SPS: spark plasma sintering, 2SS: two-step sintering.

Figure 20. Room temperature piezoelectric coefficient d_{33} as a function of grain size. Data collected from different authors.

Figure 21. SEM images of domain patterns observed in the various poled BaTiO3 ceramics with different average grain size. (a) 0.74 µm. (b) 1.63 µm. (c) 3.95 µm. (d) 8.37 µm. A progressive evolution from simple stripe patterns to more complex domain arrangements is observed with increasing grain size. Reprinted from ref. 254 with permission from Elsevier. Copyright Acta Materialia Inc. (2012).

Tables

Table 1 EIA specification codes for Class II dielectrics.

First Marking		Second Marking		Third Marking	
Symbol	**Low temperature limit (°C)**	**Symbol**	**High temperature limit (°C)**	**Symbol**	**Maximum capacitance deviation (%)**
Z	+10	4	+65	A	1.0
Y	-30	5	+85	B	1.5
X	-55	6	+105	C	2.2
		7	+125	D	3.3
		8	+150	E	4.7
		9	+200	F	5.5
				P	10.0
				R	15
				S	22
				T	+22/-33
				U	+22/-56
				V	+22/-82

Table 2. Energy storage properties of $BaTiO_3$-based bulk ceramics at room temperature. W_{rec}: recoverable (discharged) energy density. η: efficiency (ratio of discharged to charged energy density). E: electric field amplitude.

Composition	W_{rec} ($J \cdot cm^{-3}$)	η (%)	E ($kV \cdot cm^{-1}$)	Ref.
$BaTiO_3$-$Bi(M)O_3$ solid solutions				
$0.85BaTiO_3$-$0.15Bi(Mg_{0.5}Zr_{0.5})O_3$	2.9	86.8	300	192
$0.9BaTiO_3$-$0.1Bi(Zn_{0.5}Zr_{0.5})O_3$	2.46	86	264	193
0.7 $BaTiO_3$–0.3 $BiScO_3$	2.3 (6.1*)		225 (730*)	157
$0.85BaTiO_3$–$0.15Bi(Zn_{1/2}Sn_{1/2})O_3$	2.21	91.7	230	194
$0.88(0.65BaTiO_3$-$0.35Bi_{0.5}Na_{0.5}TiO_3)$-$0.08Na_{0.73}Bi_{0.09}NbO_3$	1.70	82	172	195
$0.9BaTiO_3$-$0.1Bi(Mg_{2/3}Nb_{1/3})O_3$	1.70	90	210	196
$0.9BaTiO_3$–$0.1Bi(Mg_{2/3}Nb_{1/3})O_3$	1.13	93	145	197
$0.85BaTiO_3$–$0.15Bi(Zn_{2/3}Nb_{1/3})O_3$	0.79	93.5	131	198
$0.91BaTiO_3$–$0.09BiYbO_3$	0.71	82.6	93	199
$Ba_{1-x}Sr_xTiO_3$ solid solution				
$(Ba_{0.4}Sr_{0.6})TiO_3$	1.28	-	243	200
$(Ba_{0.4}Sr_{0.6})TiO_3$	1.15	82	190	201
$Ba_{0.4}Sr_{0.6}TiO_3$–5wt%MgO	1.5	88.5	300	202
$Ba_{0.4}Sr_{0.6}TiO_3$-9wt%(Bi_2O_3-B_2O_3-SiO_2 glass)	1.98	90.6	279	203
$BaTiO_3$				
$BaTiO_3$	0.38	40.3	90	184
$BaTiO_3$	0.32	-	88	185

(*) Thin layer with 15 µm thickness

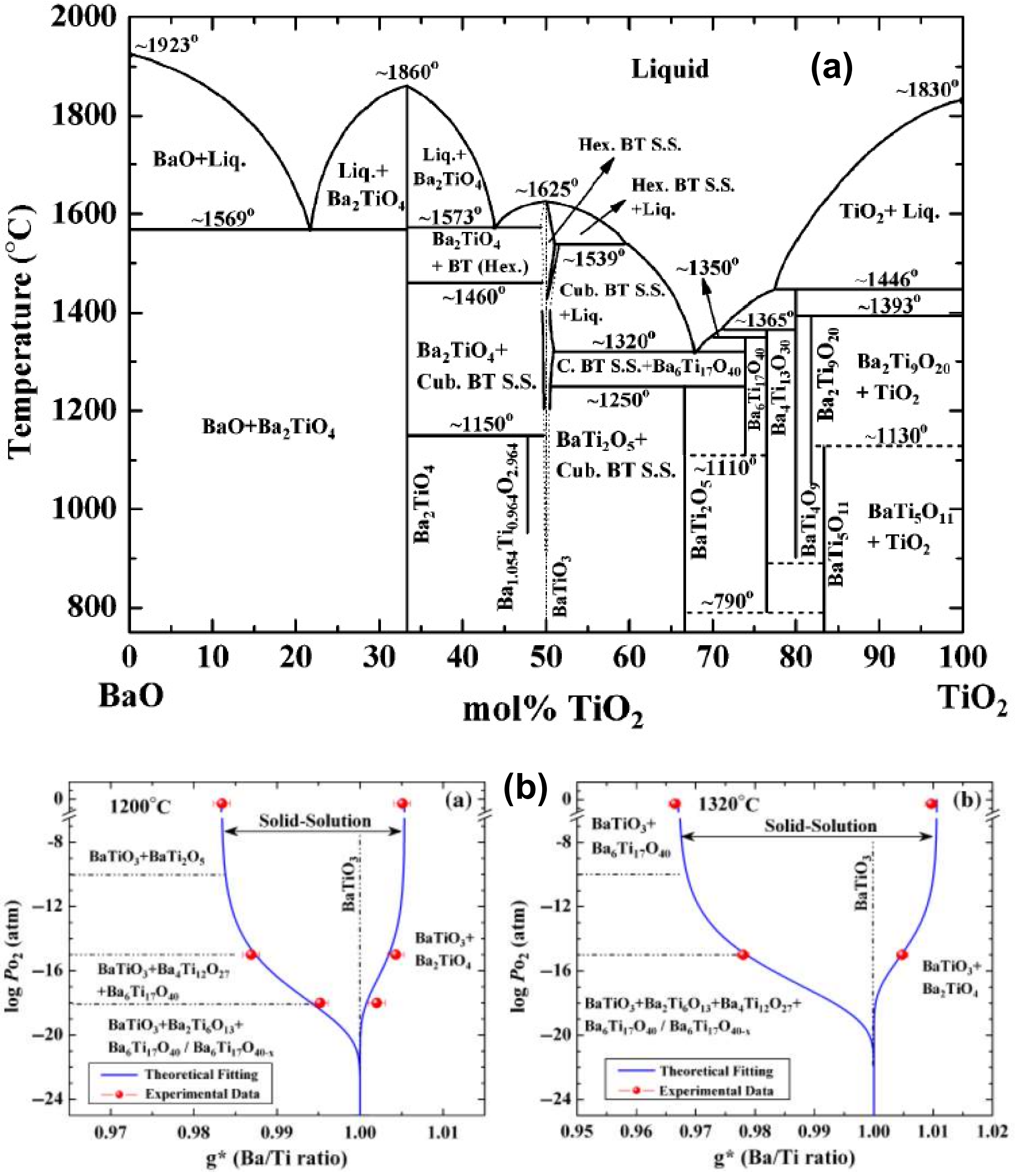

Figure 1. (a) Pseudo-binary phase diagram of the BaO–TiO_2 system under ambient air conditions. Reprinted from ref. 23 with permission of Wiley. Copyright American Ceramic Society (2007). (b) Variation of solubility regime as a function of oxygen partial pressure on the Ba- and Ti-rich sides of $BaTiO_3$ at 1200°C (left) and 1320°C (right). Reprinted from ref. 38 with permission of Wiley. Copyright American Ceramic Society (2008).

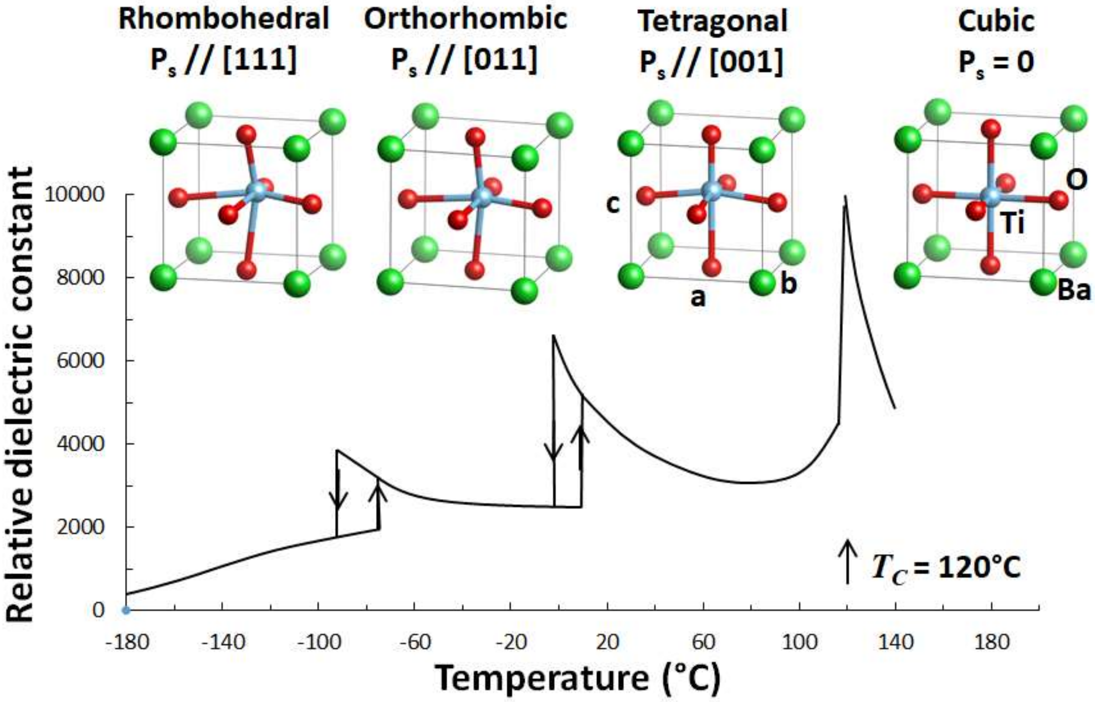

Figure 2. (a) Temperature dependence of crystal structure and relative dielectric constant along the a-axis direction in $BaTiO_3$ single crystal. Dielectric constant data from ref. 12. The Ti off centre displacement is exaggerated to be better observable.

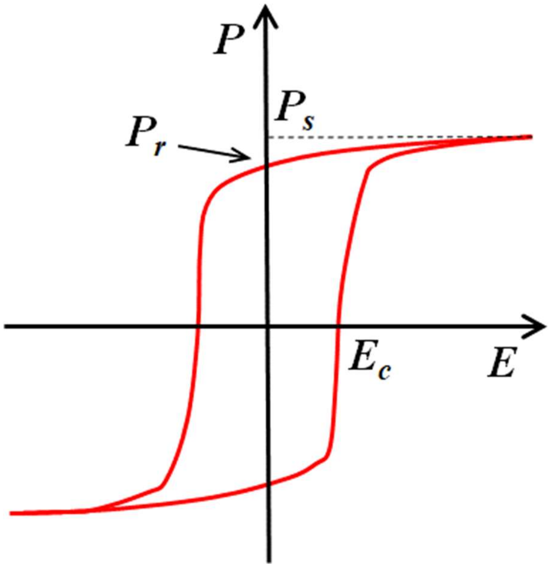

Figure 3. Polarization (P) – electric field (E) ferroelectric polarization loop.

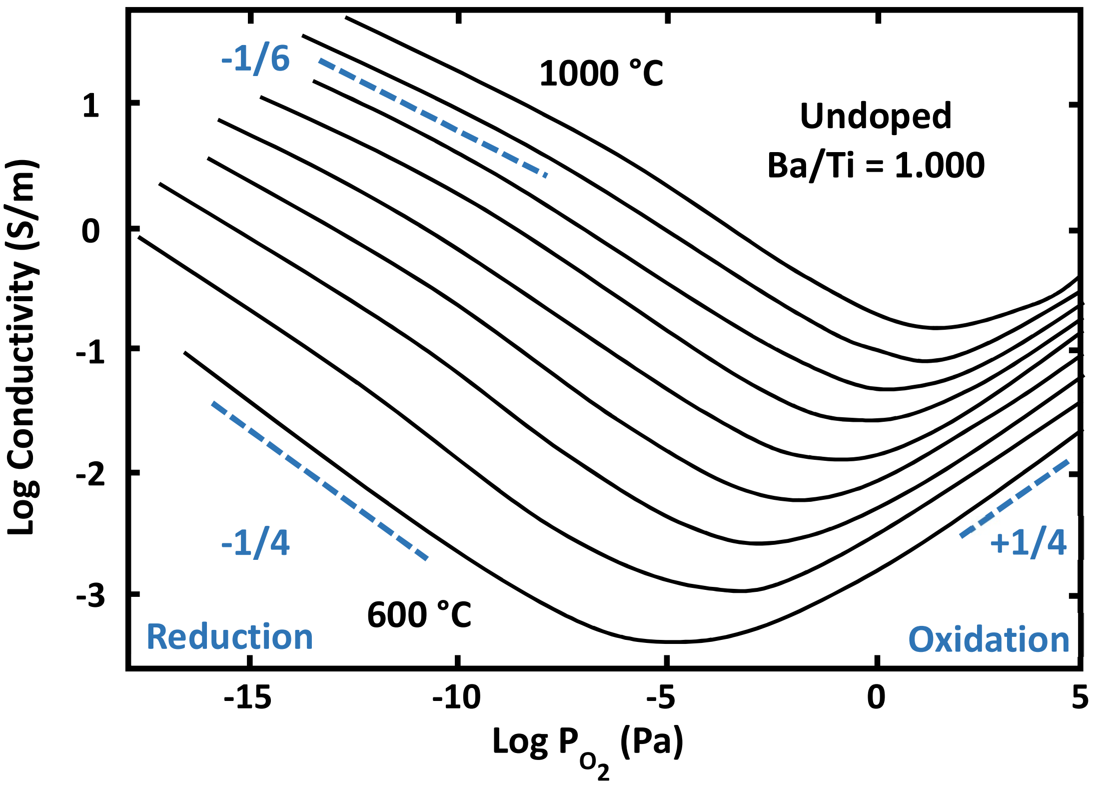

Figure 4. Equilibrium electrical conductivity of polycrystalline $BaTiO_3$ at 600-1000 °C with 50 °C interval. Data from ref. 45.

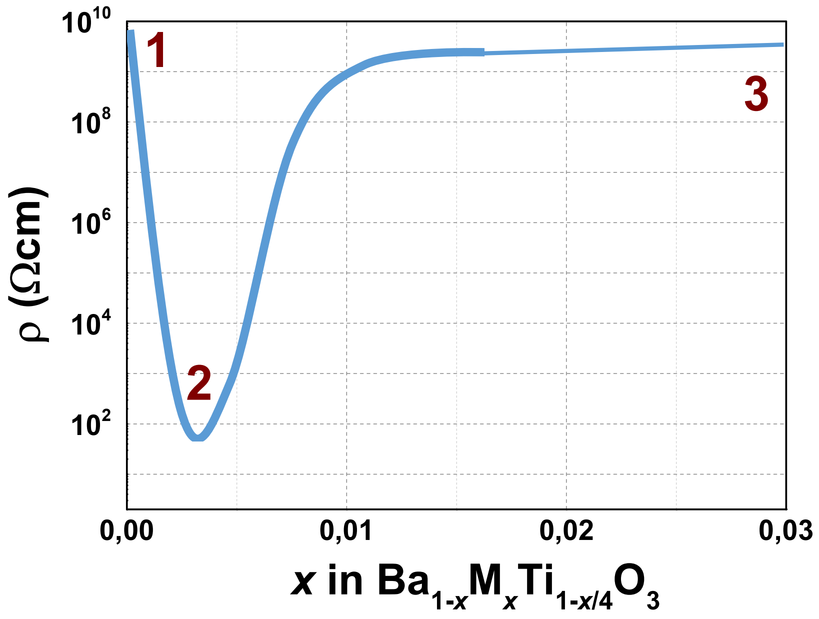

Figure 5. Schematic representation of the room-temperature dc resistivity as a function of the trivalent dopant concentration M^{3+} for ceramics heated in air. Adapted from ref. 54.

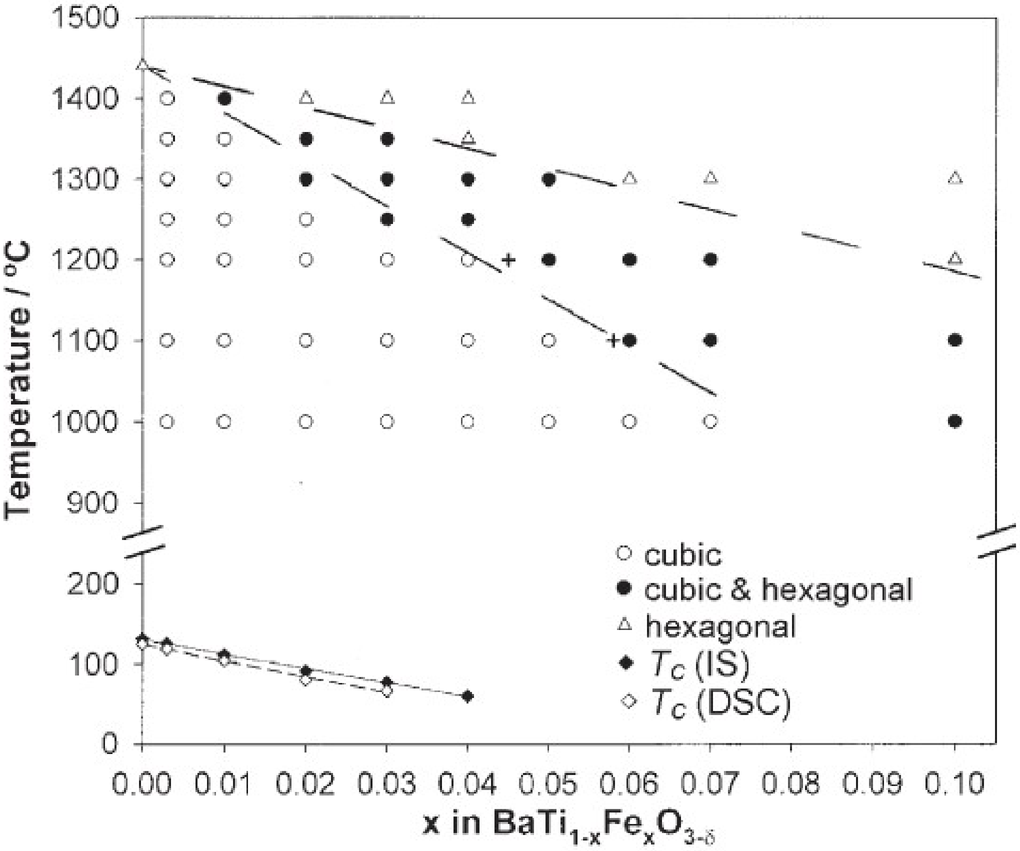

Figure 6. Phase diagram for the solid solution $BaTi_{1-x}Fe_xO_{3-\delta}$. T_C (IS) denotes Curie temperature obtained from impedance spectroscopy measurements. T_C (DSC) denotes Curie temperature obtained from differential scanning calorimetry. Reproduced from ref. 70 by permission of The Royal Society of Chemistry. Copyright (2006) The Royal Society of Chemistry.

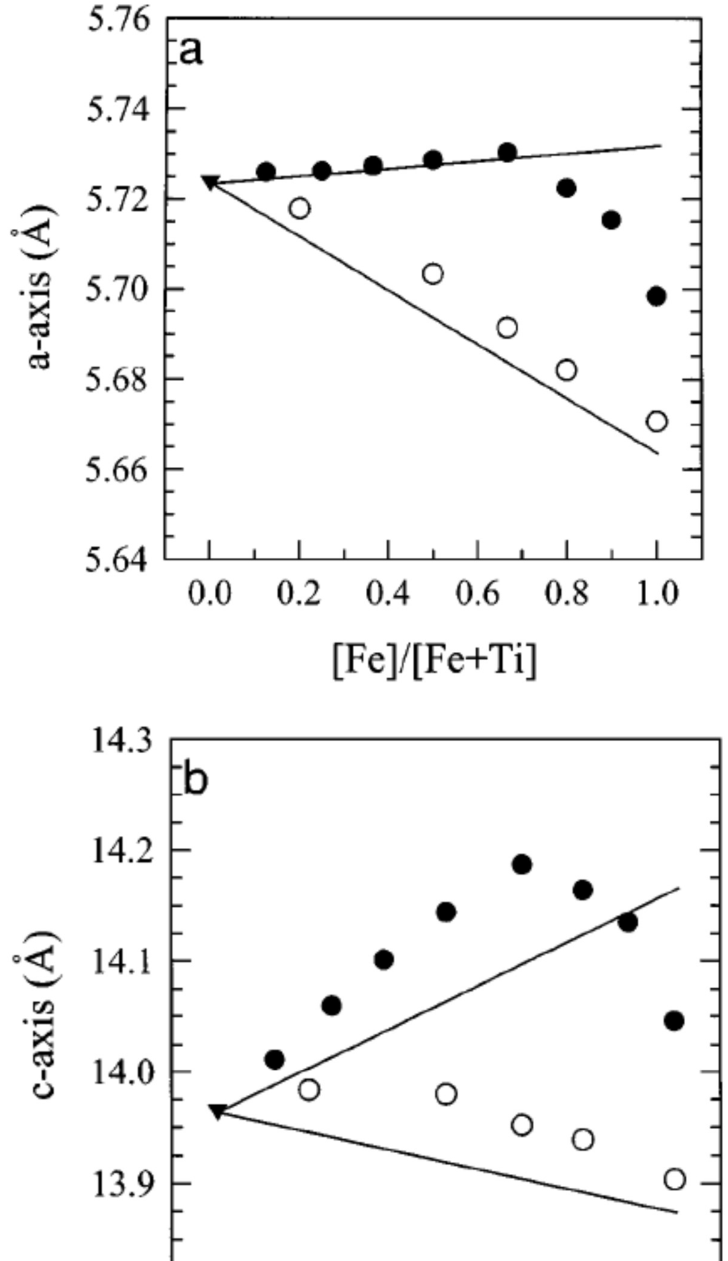

Figure 7. Lattice parameters of 6H-BaTi$_{1-x-y}$Fe$^{3+}_{x}$Fe$^{4+}_{y}$ O$_{3-x/2}$ solid solution for air-quenched (filled circles) and slow-cooled in oxygen (open circles) samples after sintering in air. The lines correspond to Vegard law cell composition relationships for BaTiO$_3$-BaFeO$_{2.5}$ (upper lines) and BaTiO$_3$-BaFeO$_3$ (lower lines). Reprinted from ref. 74 with permission from Elsevier. Copyright (1998) Academic Press.

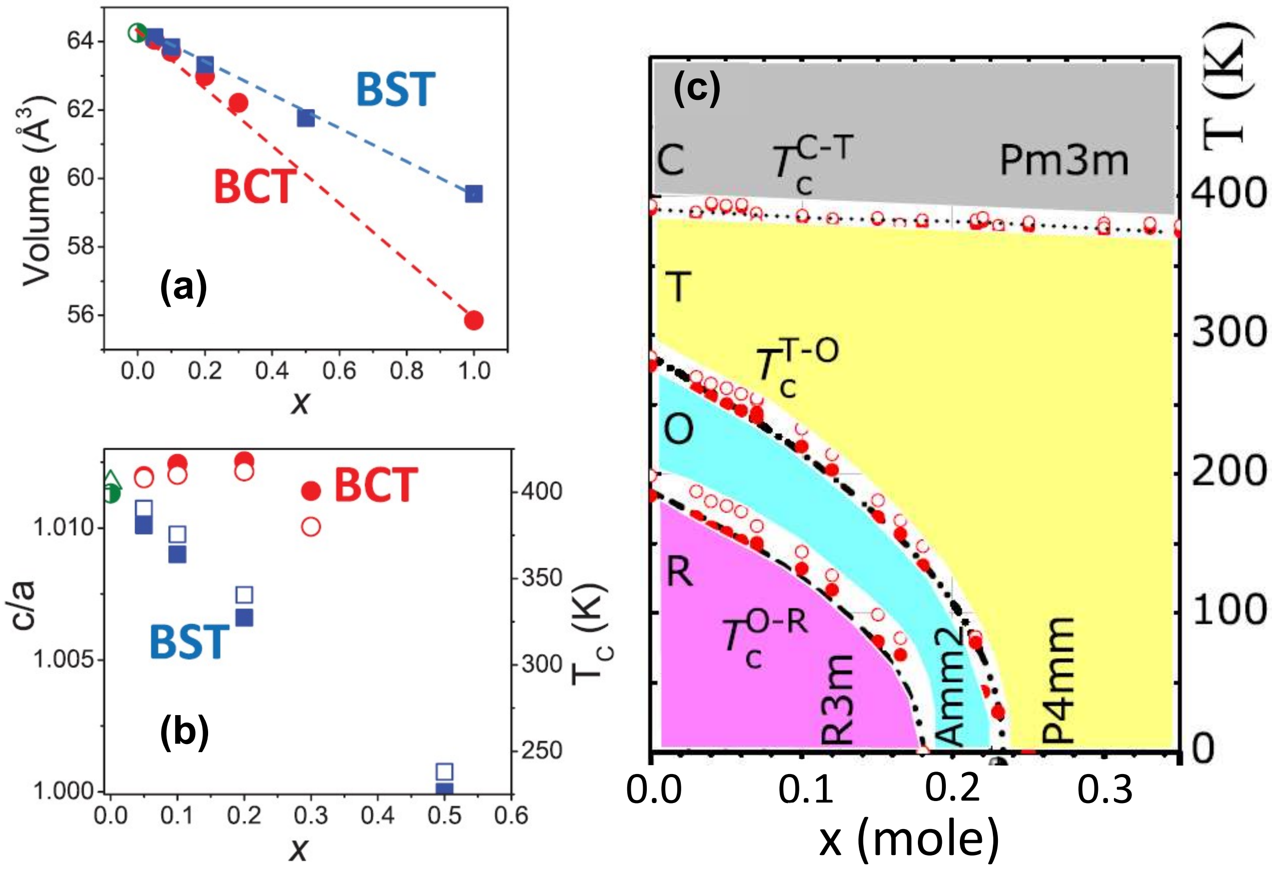

Figure 8. Compositional dependence of (a) unit-cell volume and (b) *c/a* ratio (filled symbols) and T_C (open symbols) in the $Ba_{1-x}Sr_xTiO_3$ (BST, blue) and $Ba_{1-x}Ca_xTiO_3$ (BCT, red) solid solutions. Reprinted from ref. 110, with the permission of AIP Publishing. (c) Phase diagram of the $Ba_{1-x}Ca_xTiO_3$ system. Reprinted figure with permission from ref.111. Copyright (2008) by the American Physical Society.

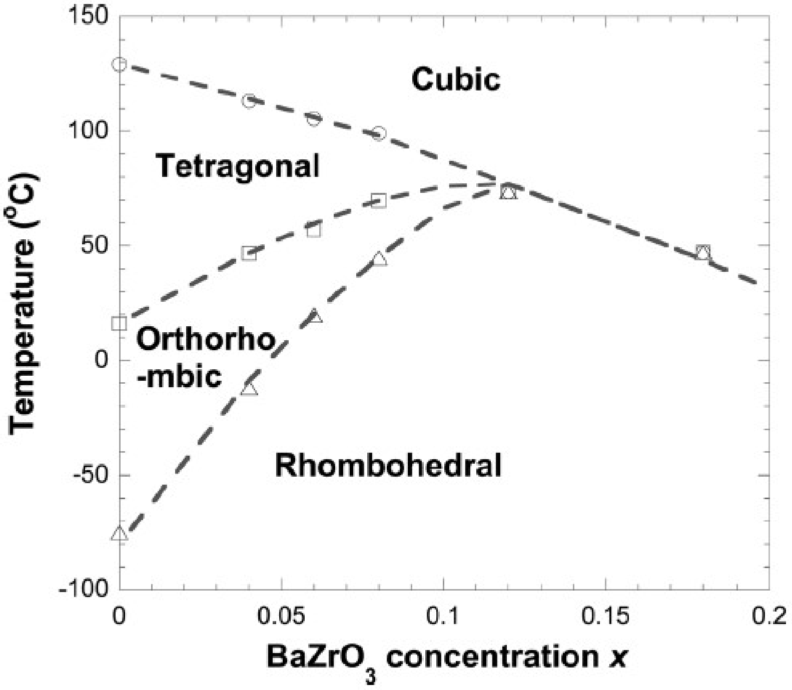

Figure 9. Phase diagram of xBaZrO$_3$-(1-x)BaTiO$_3$ ceramics with $0 \leq x \leq 0.20$. Reprinted from ref. 123, with the permission of AIP Publishing.

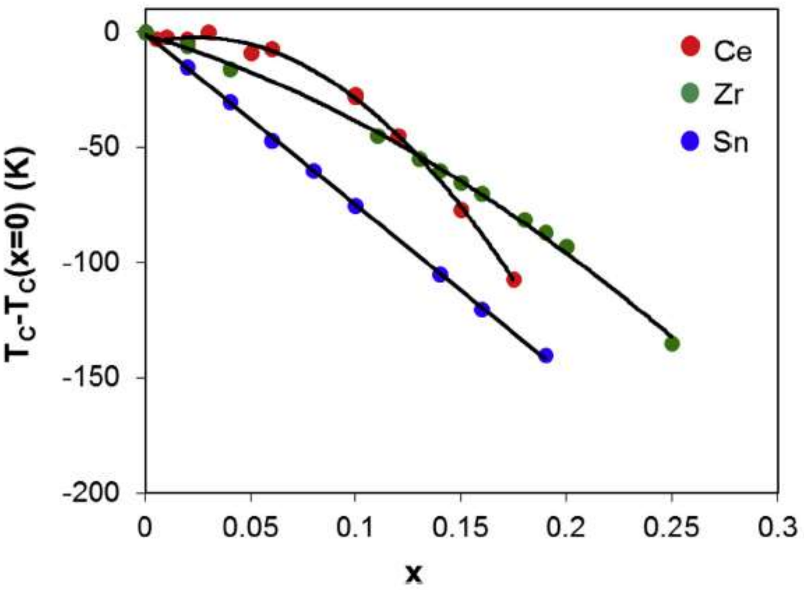

Figure 10. Variation of the Curie temperature in the $BaM_xTi_{1-x}O_3$ (M = Sn, Zr, Ce) solid solutions with respect to undoped $BaTiO_3$. Reprinted from ref. 127 with permission from Elsevier. Copyright (2018) Acta Materialia Inc.

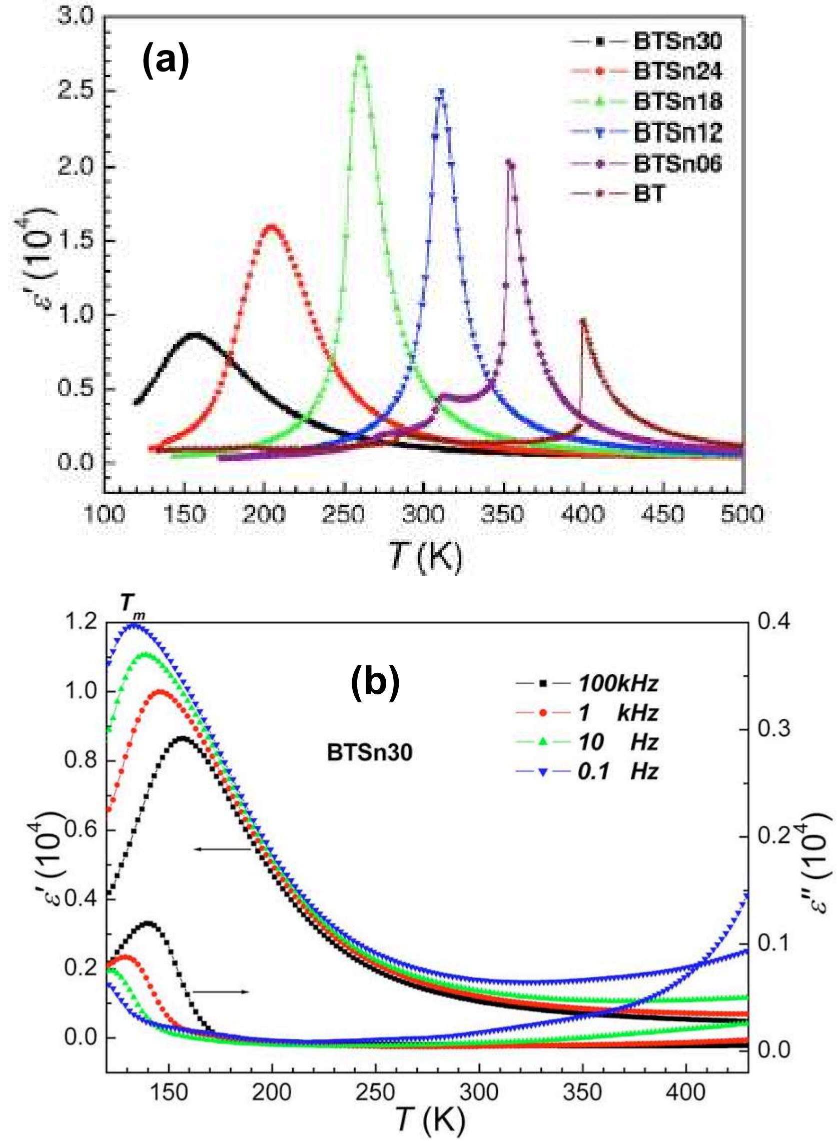

Figure 11. (a) Temperature dependence of the relative dielectric constant (ε’) of $BaTi_{1-x}Sn_xO_3$ ($x = 0, 0.06, 0.12, 0.18, 0.24, 0.30$) ceramics at 100 kHz. Composition $x = 0.12$ is close to the phase convergence point. (b) Temperature dependence of the real (ε’) and imaginary parts (ε’’) of the dielectric permittivity of ceramic with composition $x = 0.30$. Reprinted from ref. 124, with the permission of AIP Publishing.

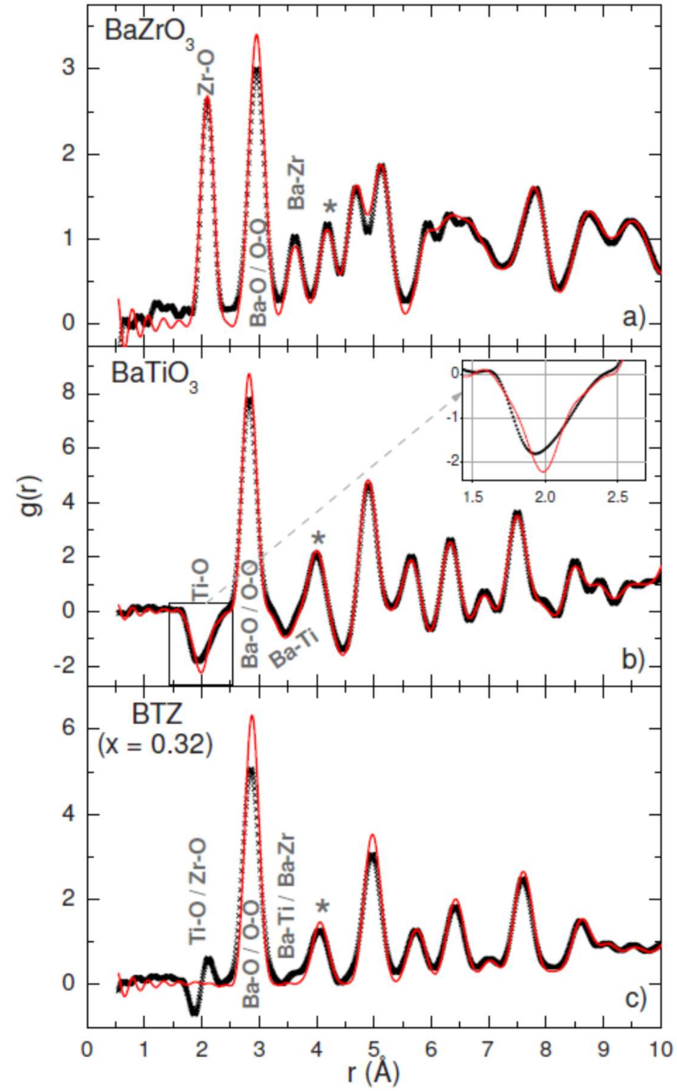

Figure 12. Experimental pair distribution function of (a) $BaZrO_3$, (b) $BaTiO_3$, and (c) $BaTi_{0.68}Zr_{0.32}O_3$ at 300 K (crosses), compared with the PDF calculated from their crystallographic structures (lines). Inset in figure (b): zoom on the contribution of the Ti-O pairs within the TiO_6 octahedra in $BaTiO_3$. Reprinted figure with permission from ref. 148. Copyright (2009) by the American Physical Society.

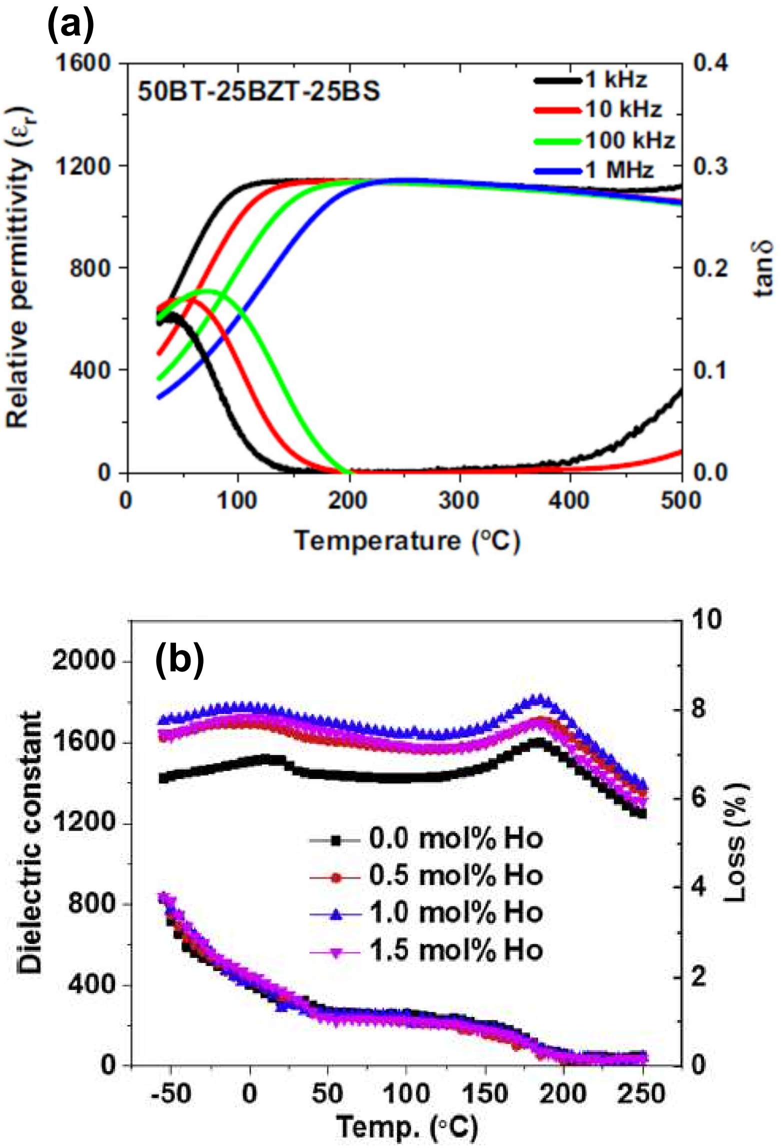

Figure 13. Dielectric properties of $BaTiO_3$-$Bi(M)O_3$ ceramics. (a) $0.50BaTiO_3$–$0.25BiZn_{1/2}Ti_{1/2}O_3$–$0.25BiScO_3$. Reprinted from ref. 156 with permission ADD DETAILS FOR PERMISSION. (b) $0.9BaTiO_3$-$0.10Bi_{0.5}Na_{0.5}TiO_3$ with 1.5 mol. % Nb_2O_5 and different Ho content (frequency: 1 kHz). Reprinted from ref. 166 with permission from Elsevier. Copyright (2019) Elsevier Ltd.

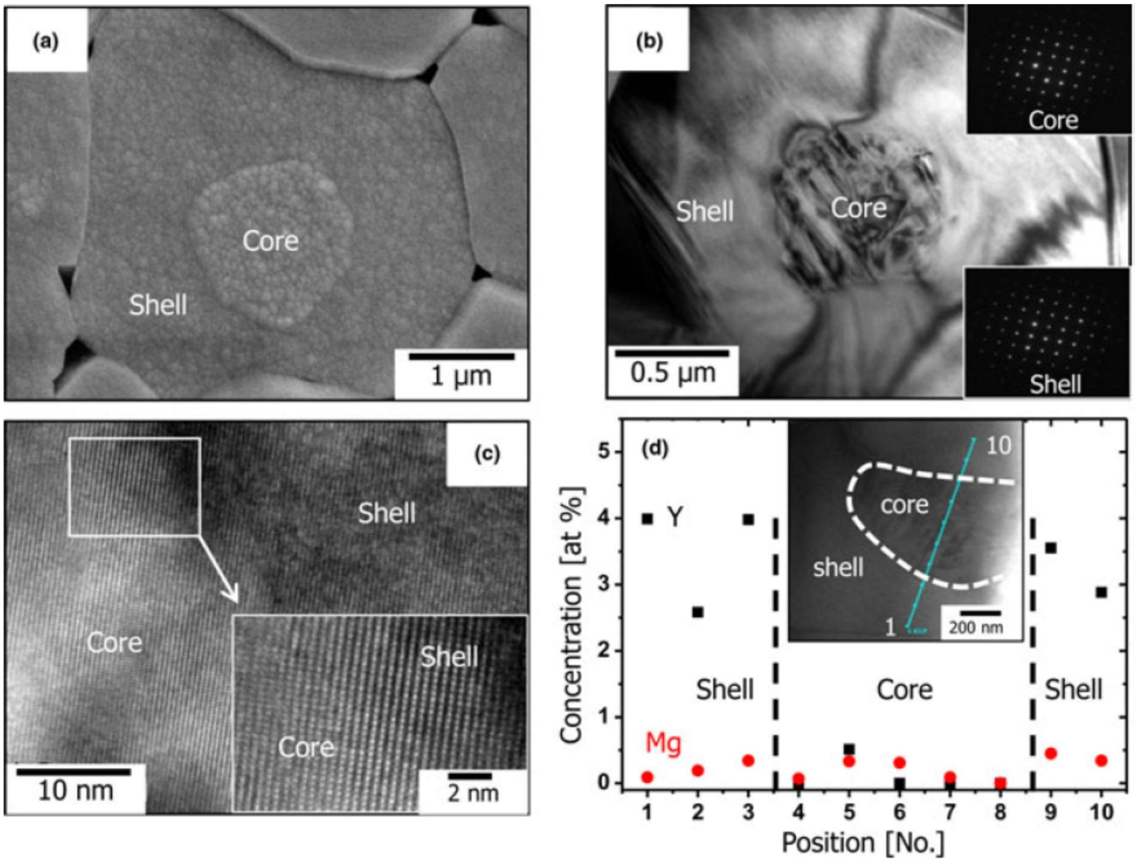

Figure 14. (a) SEM and (b) TEM micrographs showing typical core-shell structures in a sample sintered at 1350 °C in wet H_2 for 2 h; (c) HRTEM image at the interface between a core and a shell; (d) STEM/EDS line profile showing the distribution of Y and Mg. Reprinted from ref. 171 with permission of Wiley. Copyright (2012) American Ceramic Society.

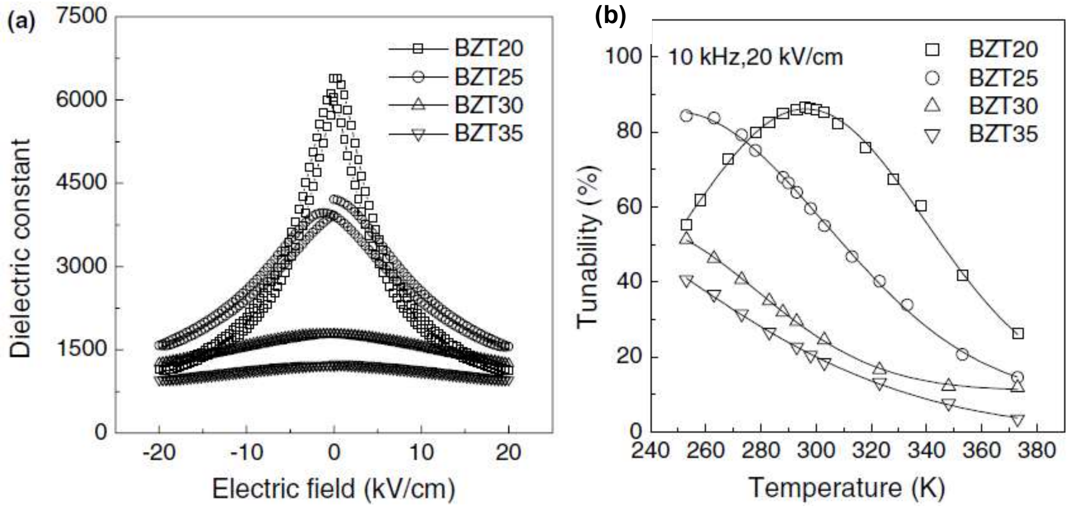

Figure 15. (a) Dielectric permittivity vs. electric field and (b) relative tunability vs. temperature for different $BaTi_{1-x}Zr_xO_3$ ceramics (x = 0.20-0.35). Reprinted from ref. 206 with permission from Elsevier. Copyright (2004) Acta Materialia Inc.

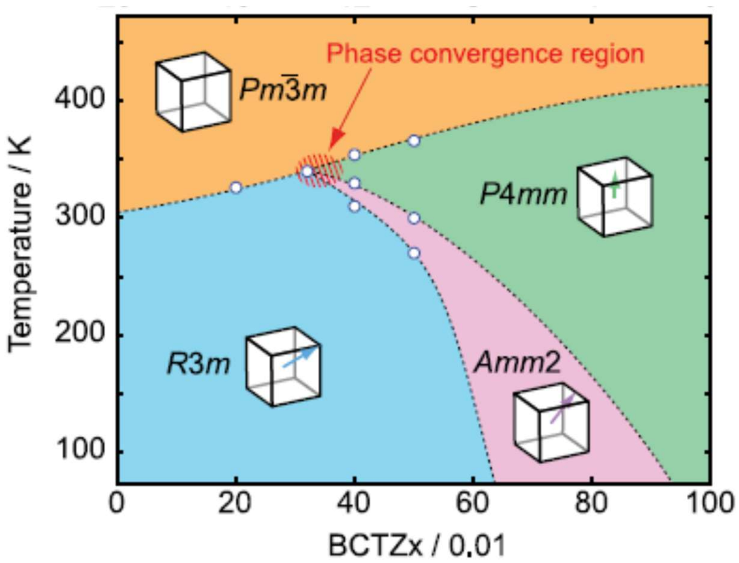

Figure 16. $x\mathrm{Ba}_{0.7}\mathrm{Ca}_{0.3}\mathrm{TiO}_3$-(1-$x$)$\mathrm{BaZr}_{0.2}\mathrm{Ti}_{0.8}\mathrm{O}_3$ phase diagram. Reprinted from ref. 212 with the permission of AIP Publishing.

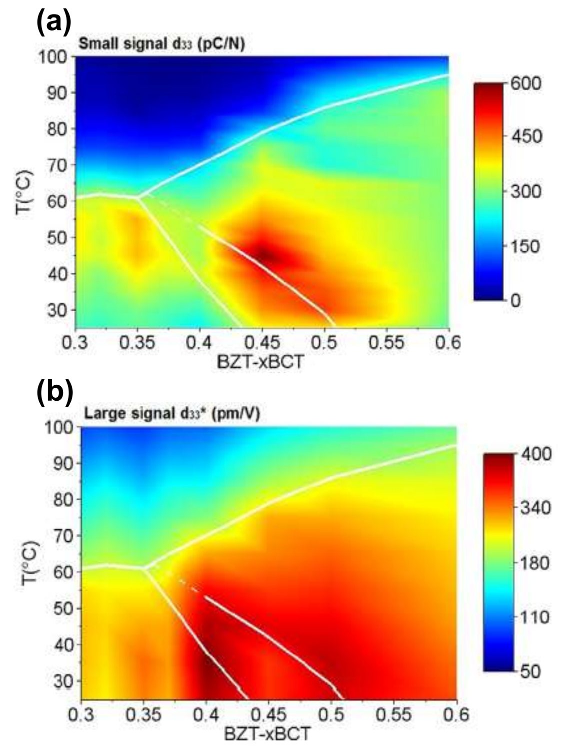

Figure 17. Contour plot of (a) small signal d_{33} and (b) large signal d_{33}^{*} as a function of temperature and composition in the $(1-x)\mathrm{Ba}(\mathrm{Zr}_{0.2}\mathrm{Ti}_{0.8})\mathrm{O}_3$-$x(\mathrm{Ba}_{0.7}\mathrm{Ca}_{0.3})\mathrm{TiO}_3$ system. Reprinted from ref. 213 with permission from Elsevier. Copyright Acta Materialia Inc. (2014).

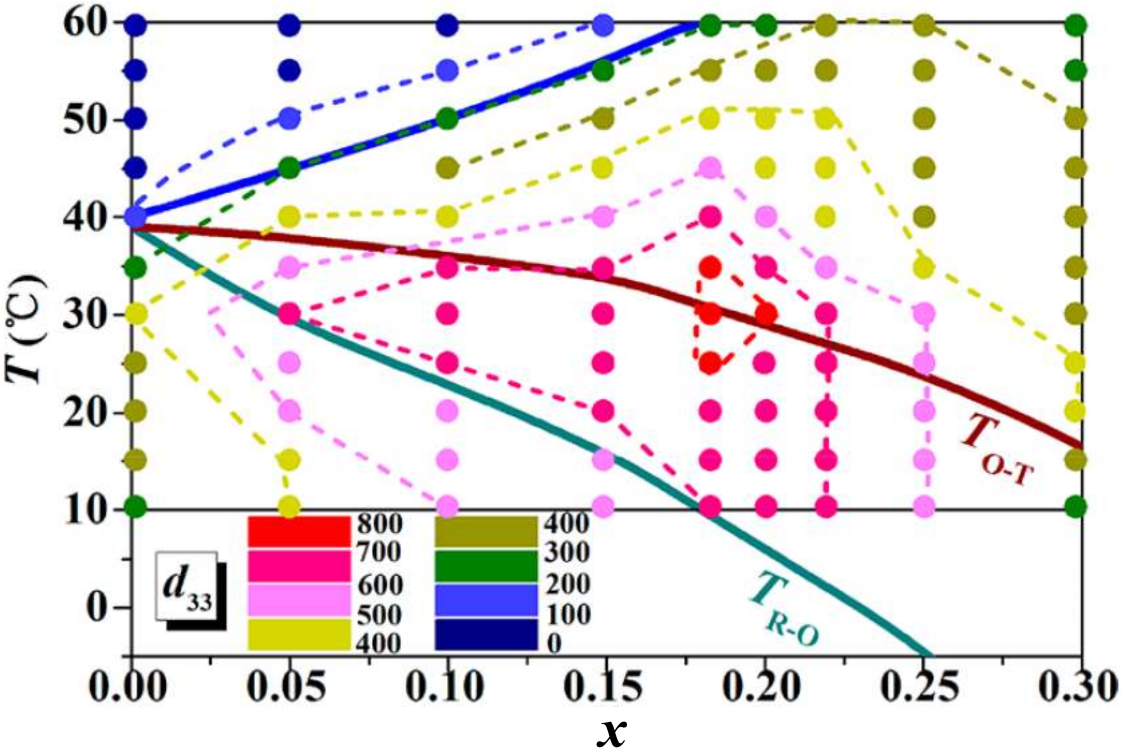

Figure 18. Map of piezoelectric coefficient d_{33} as a function of temperature and composition in the system $(1-x)Ba(Ti_{0.89}Sn_{0.11})O_3-x(Ba_{0.70}Ca_{0.30})TiO_3$. Reprinted with permission from ref. 232. Copyright (2018) American Chemical Society.

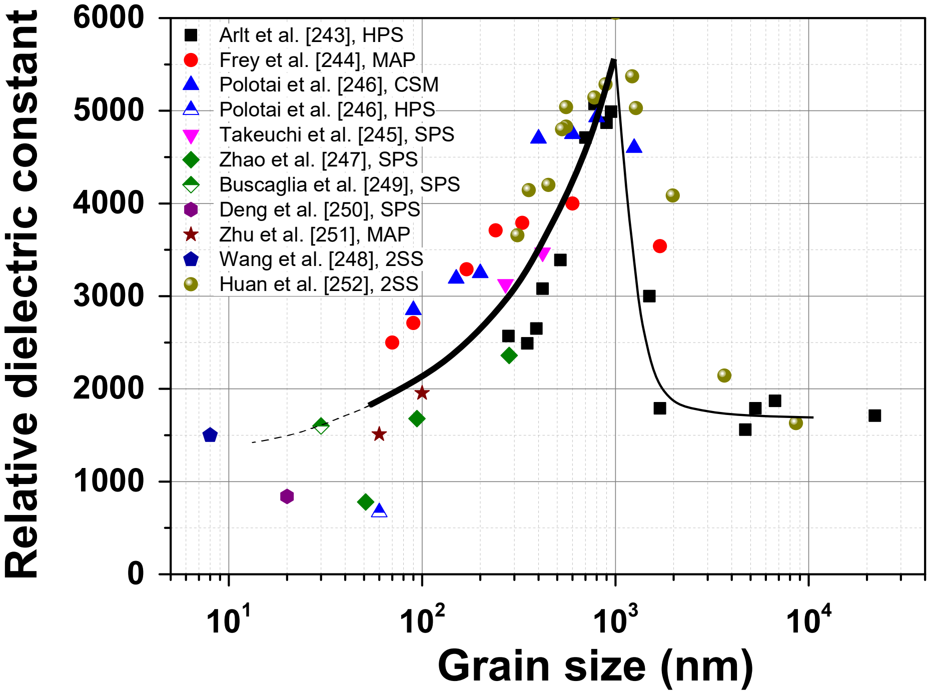

Figure 19. Room temperature dielectric constant of $BaTiO_3$ ceramics as a function of grain size. Data collected from different authors. HPS: hot pressing sintering, MAP: multi-anvil press, CSM: combined sintering method, SPS: spark plasma sintering, 2SS: two-step sintering.

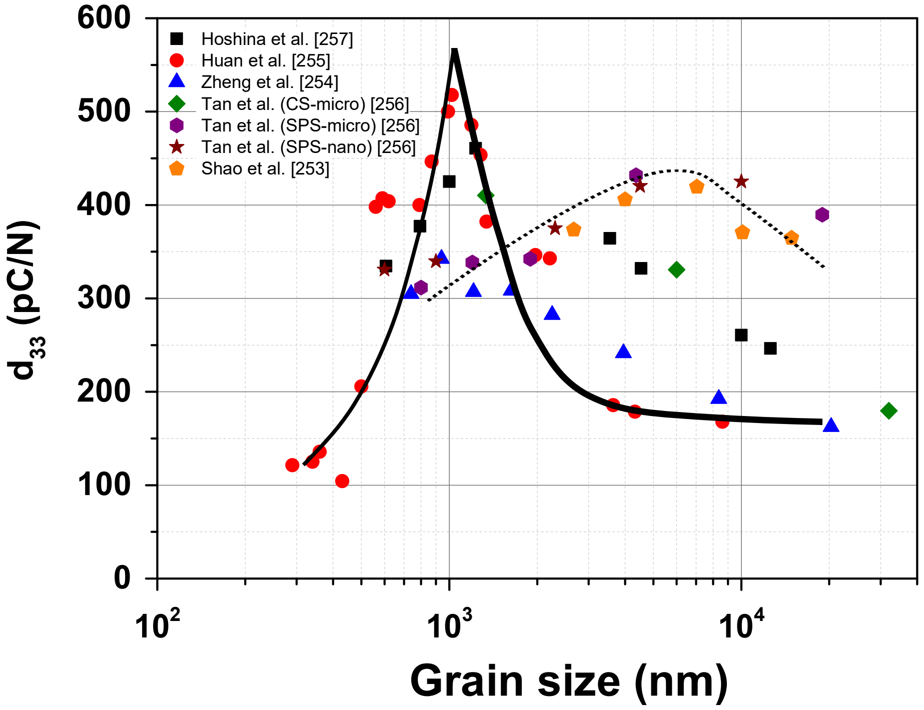

Figure 20. Room temperature piezoelectric coefficient d_{33} as a function of grain size. Data collected from different authors.

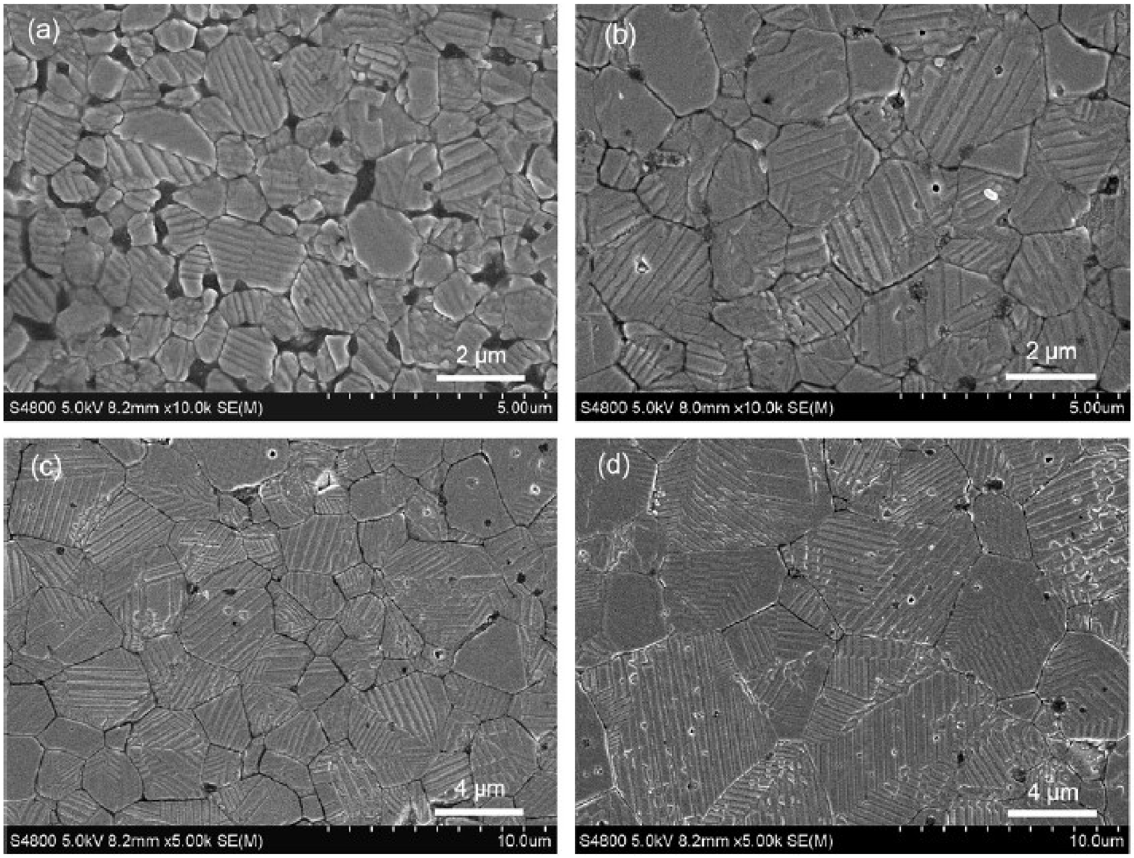

Figure 21. SEM images of domain patterns observed in the various poled BaTiO3 ceramics with different average grain size. (a) 0.74 µm. (b) 1.63 µm. (c) 3.95 µm. (d) 8.37 µm. A progressive evolution from simple stripe patterns to more complex domain arrangements is observed with increasing grain size. Reprinted from ref. 254 with permission from Elsevier. Copyright Acta Materialia Inc. (2012).